Technische Universität München

Fakultät für Physik

Single-Photon Distillation and Nonlocal Quantum-Logic Gate

Severin Daiß

Vollständiger Abdruck der von der Fakultät für Physik der Technischen Universität München zur Erlangung des akademischen Grades eines

Doktors der Naturwissenschaften (Dr. rer. nat.)

genehmigten Dissertation.

Vorsitzende :   Prof. Dr. Nora Brambilla

Prüfer der Dissertation :   1. Hon.-Prof. Dr. Gerhard Rempe
                            2. Prof. Dr. Stefan Filipp

Die Dissertation wurde am 07.09.2021 bei der Technischen Universität München eingereicht und durch die Fakultät für Physik am 21.11.2021 angenommen.

Abstract

This dissertation reports on the experimental realization and analysis of two quantum information processing protocols. In particular, it discusses the demonstration of a nonlocal quantum gate between two separate qubit modules that are connected by a 60-meter-long optical fiber. The modules are each composed of a high-finesse optical cavity with a strongly coupling rubidium atom trapped at its center. The qubits are encoded on the two distant atoms and the nonlocal quantum gate between them is performed in two steps. First, a photon is successively reflected from the two modules. Then there is a suitable measurement of the photon, and, conditioned on the result, a feedback is applied to the first qubit. The photon detection also serves as a herald of a successful gate operation. With this protocol, an overlap of $(85.1 \pm 0.8)\,\%$ with the truth table of an ideal quantum controlled-NOT gate has been achieved. Furthermore, the nonlocal gate has been used to create all four maximally-entangled Bell states from separable input states with an average fidelity of $(76.6 \pm 1.0)\,\%$.

In another series of experiments, one of the modules is used to distill single photons out of incoming weak coherent pulses that are reflected from the atom-cavity system. A subsequent measurement of the atom establishes a projective measurement of the photon-number parity. For input pulses with a low average photon number, a projection on the odd-parity Fock states has allowed to create light that has an overlap of $(66 \pm 1)\,\%$ with an ideal single-photon Fock state. The suppression of higher Fock states is confirmed by the light's second-order correlation function with $g^{(2)}(0) = 0.045 \pm 0.006$.

List of Publications

- **Cavity Carving of Atomic Bell States.**
  S. Welte, B. Hacker, S. Daiss, S. Ritter, and G. Rempe.
  Phys. Rev. Lett. **118**, 210503 (2017).

- **Photon-Mediated Quantum Gate between Two Neutral Atoms in an Optical Cavity.**
  S. Welte, B. Hacker, S. Daiss, S. Ritter, and G. Rempe.
  Phys. Rev. X **8**, 011018 (2018).

- **Deterministic creation of entangled atom-light Schödinger-cat states.**
  B. Hacker, S. Welte, S. Daiss, A. Shaukat, S. Ritter, L. Li, and G. Rempe.
  Nat. Photon. **13**, 110–115 (2019).

- **Single-Photon Distillation via a Photonic Parity Measurement Using Cavity QED.**
  S. Daiss, S. Welte, B. Hacker, L. Li, and G. Rempe.
  Phys. Rev. Lett. **122**, 133603 (2019).

- **A quantum-logic gate between distant quantum-network modules.**
  S. Daiss, S. Langenfeld, S. Welte, E. Distante, P. Thomas, L. Hartung, O. Morin, and G. Rempe.
  Science **371**, 614–617 (2021).

- **Quantum Teleportation between Remote Qubit Memories with Only a Single Photon as a Resource.**
  S. Langenfeld, S. Welte, L. Hartung, S. Daiss, P. Thomas, O. Morin, E. Distante, and G. Rempe.
  Phys. Rev. Lett. **126**, 130502 (2021).

- **A nondestructive Bell-state measurement on two distant atomic qubits.**
  S. Welte, P. Thomas, L. Hartung, S. Daiss, S. Langenfeld, O. Morin, G. Rempe, and E. Distante.
  Nat. Photon. **15**, 504–509 (2021).

- **Quantensysteme lernen gemeinsames Rechnen.**
  S. Daiss und G. Rempe.
  Phys. Unserer Zeit **52**, 113–113 (2021).

- **Detecting an Itinerant Optical Photon Twice without Destroying It.**
  E. Distante, S. Daiss, S. Langenfeld, L. Hartung, P. Thomas, O. Morin, G. Rempe, and S. Welte.
  Phys. Rev. Lett. **126**, 253603 (2021).

Contents

1. Introduction

The advent of quantum mechanics has arguably been the major scientific advancement of the last century. Not only it has deepened our understanding about many phenomena in nature, but it has also enabled many important technologies that became an integral part of today's society. This success story started in 1900, when Max Planck formulated his description of black-body radiation [1]. He assumed that the energy E at a frequency ν was emitted only in discrete quantities $E = h \times \nu$, with a constant h that is today named Planck's constant in his honor. Five years after Planck's paper, Einstein introduced in his discussion of the photoelectrical effect the concept that radiation consists of discrete quanta of energy localized in space [2] and the idea of photons was born [3]. The concept of quantization was subsequently used to explain other phenomena, like the spectral lines of the hydrogen atom [4]. Major steps in what was soon named *quantum mechanics* [5] evolved first based on paradigm-shifting insights, e.g. from de Broglie [6] or Pauli [7]. In the following, it was put on a mathematically sound footing by influential physicists like Heisenberg [8], Dirac [9], and Schrödinger [10]. An important means to understand and discuss the implications of this revolutionary new theory were various thought experiments, as the double-slit for matter waves discussed by Niels Bohr [11] or Schrödinger's cat [12], to name just two. Many of these gedanken experiments used simple systems consitisting of single matter or light quanta. For a long time, it was believed that these experiments would remain purely abstract. In 1952, Schrödinger wrote *"we never experiment with just one electron or atom or (small) molecule. In thought-experiments we sometimes assume that we do; this invariably entails ridiculous consequences"* [13]. However, the quantum theory also enabled huge technological advances that finally allowed to transfer the first gedanken experiments to the laboratory.

Foremost in these advances was the first demonstration of the laser by Theodore Maiman in 1960 [14], a tool which became the single most useful one in today's quantum optics experiments. With neutral atoms, the laser allowed for the first cooling [15] and deceleration of atomic beams [16]. This lead to the stopping of an atomic beam [17,18], to the first cloud of atoms confined in a magneto-optical trap (MOT) [19–21], and ultimately even to the first Bose-Einstein condensate in that atoms jointly occupy the lowest quantum state [22–24]. But also pure optical trapping in laser light was achieved in optical tweezers [25] or lattices [26]. These advances set the groundwork for first experiments using single neutral atoms [27]. In the meantime, charged particles could already be trapped without the help of a laser. In 1959, a single electron was stored using the static electrical field of a Penning trap [28] and in 1980, a single ion was localized using switching electrical fields in a quadrupole Paul trap [29]. All these developments therefore enabled an experimental use of single particles. It thus became possible to observe in the laboratory the *"ridiculous consequences"* Schrödinger mentioned [13] and to translate famous thought experiments to real-world studies [30–32]. Even more, we are now in a position to harness these quantum

effects for applications. In the same way as quantum theory empowered a first quantum revolution with numerous technologies, from the transistor and the laser to medical imaging and atomic clocks [33], this unprecedented control of single quanta is now bringing a second quantum revolution toward quantum systems that are controlled at the individual particle level [34, 35].

Some of the most striking technologies that are researched in this context come from the fields of quantum networks and quantum computation. Quantum networks allow sharing and extending the capabilities of individual (quantum) modules by interconnecting them with quantum channels [36]. One of the most remarkable features in the transmission of quantum information is that it can allow to identify the presence of eavesdroppers during the distribution of a secret key [37] by exploiting the no-cloning theorem of quantum mechanics [38]. With this, quantum communication promises a security technology that is based entirely on fundamental physical principles and that is therefore not jeopardized by future algorithmic improvements [39]. Networks of quantum systems could furthermore be used in sensing applications with an array of atomic clocks that could allow for unprecedented stability [40] or for beam and molecule tracking [41], to name just two more examples. Aside from these applications, quantum networks also aided experiments to test the very fundamentals of quantum mechanics, for instance concerning the notion of local realism and the existence of hidden variables brought forward by Einstein, Podolski and Rosen (EPR) [42]. Bell experiments allow to test this assumption [43–45] and the additional possibility to transport quantum states over longer distances achieved to close the locality loop-hole in these tests [46–48]. This helped to prove that the local realism suggested by EPR does not apply to quantum mechanics.

For most applications envisioned today, quantum information is transmitted between network modules using photonic states, by virtue of their speed and negligible coupling to other electromagnetic radiation. Qubits can be encoded in traveling single photons that couple to and interact with different stationary qubit modules [49, 50], and they have been used to implement various key protocols, as, for example, in the teleportation of quantum states [51–53]. For the transmission, photons can be conveniently guided in optical silica fibers. However, wavelength-dependent attenuation leads to a loss exponential in distance that limits the range of quantum communication applications based on such a direct transport of single photons. In contrast to the transmission of classical information, the no-cloning theorem prevents an amplification of the transmitted signal to counteract this effect. One approach to still send quantum information over long distances is by a free-space transmission via mediating satellites. This way of propagating light results in a loss quadratic in distance, avoiding the inferior exponential scaling of optical fibers. In this way, a quantum key distribution was performed over a distance of 7600 km between China and Austria using light at single-photon level in 2018 [54]. However, small satellite coverage, short interaction times, the dependence on weather conditions, and a required night-time operation [55] still limit the flexibility of such connections. A different approach to establish fiber-based high-fidelity entanglement between remote sites is given by quantum repeaters that were proposed by Briegel, Dür, Cirac, and Zoller in 1998 [56]. The idea is to use nested, intermediate nodes and to connect them with single photons [57]. By means of entanglement swapping [58], the entanglement of neighboring nodes can be transferred to more distant nodes. Additionally, entanglement purification can be employed to increase

the fidelity in this process [59]. The realization of this scheme is one of the great outstanding research goals in quantum communication [60].

Network applications concerned with the processing of quantum information typically use stationary qubits that enable an efficient storage and local manipulations in the different modules. The dichotomy between the flying, photonic and the stationary types of qubits requires an efficient interface to interconvert between them in order to allow constructing networks of qubit modules [60]. To date, elementary quantum networks have used various different interfaces to demonstrate photonic state transfer and/or entanglement between separated modules, with examples ranging from neutral atoms [61], vacancy centers in diamond [62], ions [63], quantum dots [64], atomic ensembles [65], to even two different platforms [66]. These experiments are the first steps toward larger networks that might one day result in a global quantum internet [36,67]. A particularly well-suited network interface is provided by single atoms strongly coupled to a resonator. This type of system has first been established in the 1980s in the microwave domain [31,68,69]. Mirrors with very high reflectivities [70] have finally allowed transfering these interconnects to the optical regime and several important milestones toward quantum networks have first been reached with them [71] (see also Chapter 3.1).

While the importance of the single photon transcends the field of quantum networks, the given examples and visions already highlight the significance of single photons as a resource. However, single photons are non-classical states of light and as such are hard to produce. Hitherto demonstrated sources typically rely either on the emission of single photons or the use of non-linear effects. Both approaches struggle with the removal of unwanted contributions in the final light, either stemming from the vacuum or the two-photon contribution. In [72], we report on a different technique that distills single photons from a reservoir state and this work is presented in this thesis in Chapter 4.

The key technology in what was labeled the second quantum revolution is maybe quantum computation. It uses the genuine quantum features of the individual quantum constituents for calculations. Since nature is not classical, information processing systems based on quantum mechanisms are inherently more effective in the simulation of quantum systems [73,74]. But the envisioned applications for quantum computation tasks far exceed this. In a general approach, the individual particles are used to encode a quantum bit of information (qubit) in an effective two-level system [75]. The qubit can hereby also assume coherent superpositions of the two levels, enabling a quantum computer that can not only simulate other quantum machines [76,77], but that can additionally allow to solve certain important computational problems that are intractable with classical machines. Two of the most prominent examples of this are the prime factorization algorithm by Peter Shor [78] and the search algorithm in unstructured databases by Lov Grover [79]. These prospects and possibilities sparked a huge interest in the field of quantum computation and systems based on a multitude of different types of physical hardware are being actively explored, for example, using ions [80], neutral atoms [81], nuclear magnetic resonance solutions [82], superconducting qubits [83], or photons [84]. Even international corporations like Google or IBM became key players in the exploration of this field [85,86].

In spite of all this effort, the largest of the current systems features only a few dozens of qubits: As opposed to classical bits, the encoding of qubits is typically very fragile

and therefore the requirements to build a universal quantum computer are demanding and very different from the ones for classical machines. The qubits require techniques for faithful initialization and measurement, long coherence times, and a universal set of gates, all within a scalable architecture, as outlined by David DiVincenzo [87]. However, for increasing system sizes, it becomes harder to maintain a good isolation of the qubits from the environment while at the same time retaining the ability to have controlled operations and interactions over longer distances [88, 89]. Today, the upscaling is still a major challenge in the construction of quantum computers. Not only could more qubits increase the computational space, but the availability of many of them is a necessity to implement quantum error correction (QEC) protocols, arguably one of the main steps to bring quantum computation to the next level. For these error correction codes, one logical qubit would be implemented by many physical qubits, where the exact number depends on the applied QEC code [90]. A proposed solution to the scaling problem comes from employing quantum networks as discussed above: Smaller and well isolated qubit modules could be connected via optical fibers to form a larger, combined machine [91, 92]. A key aspect is that such a network for quantum information processing tasks could encode information not only in each individual node or module but also between them. The loss intrinsic in fiber networks could be adequately met by heralded protocols that use measurements to confirm a successful transmission through the network channel [71]. Albeit first steps in this direction have been taken with entangling distant modules optically in elementary quantum networks, for a quantum computer it is crucial to be able to perform quantum gates between qubits residing in separated network modules [93]. This has first been achieved in our work [94], which is presented in Chapter 5 of this thesis.

This thesis is outlined as follows: In Chapter 2, I explain the basic theory and introduce the most important concepts of the modules used in this work. Chapter 3 characterizes the experimental realization of the two modules and describes the tools we have available to control the quantum state of the qubits. The following two chapters present the main results of this thesis. First, in Chapter 4, a photonic parity measurement and its application to distill single photons is shown. Then, in Chapter 5, the demonstration of a nonlocal quantum-logic gate between two modules separated by a 60-m-long optical fiber is presented. Lastly, Chapter 6 discusses possible next steps based on the introduced protocols that might prove fruitful for future experiments.

2. Theoretical Foundation

This chapter lays the basis for the description of concepts, interactions, and labeling used in the present work. First, I introduce the theory of atom-cavity systems that form the heart of the experiments detailed in this thesis. Then the basics of quantum information are discussed and the atom-photon gate, which is the underlying interaction mechanism for the results given in this work, is introduced.

2.1. Atom-Cavity Systems

As it was outlined in the introduction in Chapter 1, single atoms that couple strongly to an optical cavity are a prime example of a system interfacing photons and stationary qubits in a future quantum network. Atom-resonator systems are the basic modules for the work performed in this thesis and are therefore introduced in more detail in the following sections.

2.1.1. Cavity Quantum Electrodynamics

In free space, the coupling between single atoms and single photons is very weak due to the small cross-section of maximally $3\lambda^2/(2\pi)$ for resonant light of wavelength λ [95]. This interaction can be vastly increased by employing an optical resonator around the atom which enhances the resonant light field. The radiative properties of an effective two-level system or spin – given by the atom in our case – in such a cavity are described by the theory of cavity quantum electrodynamics (cQED). For a strong enough coupling between the spin and the cavity mode, the interaction with the environment outside the resonator can be neglected. The Hamiltonian of the combined system consists then of a term for the bare atomic spin $\hat{H}_\mathrm{a}$, a term for the energy in the resonator field $\hat{H}_\mathrm{c}$ and an interaction term $\hat{H}_\mathrm{int}$. Assuming that the cavity resonance frequency ω_c and the spin transition frequency ω_a between the atomic ground ($|g\rangle$) and excited state ($|e\rangle$) are close, the rotating wave approximation can be applied to neglect interaction terms oscillating at optical frequencies $\omega_c + \omega_a$. This results in the Jaynes-Cummings Hamiltonian [96] that is given by

$$\hat{H}_\mathrm{JC} = \underbrace{\hbar\omega_a \hat{\sigma}^+ \hat{\sigma}^-}_{\hat{H}_\mathrm{a}} + \underbrace{\hbar\omega_c \hat{a}^\dagger \hat{a}}_{\hat{H}_\mathrm{c}} + \underbrace{\hbar g(\hat{a}\hat{\sigma}^+ + \hat{a}^\dagger\hat{\sigma}^-)}_{\hat{H}_\mathrm{int}}. \tag{2.1}$$

In this equation, $\hat{\sigma}^+ = |e\rangle \langle g|$ and $\hat{\sigma}^- = |g\rangle \langle e|$ are the atomic raising and lowering operators and the photonic creation and annihilation operators $\hat{a}^\dagger$ and $\hat{a}$ have been used. The

interaction term in Eq. 2.1 describes the coherent coupling between the resonator and the atom with the coupling strength [97]

$$g = \sqrt{\frac{\omega_c}{2\hbar\epsilon_0 V}}\mu_{ge}\psi_c\left(\vec{r}\right). \tag{2.2}$$

Here ϵ_0 is the vacuum permittivity and $\psi_c\left(\vec{r}\right)$ gives the normalized intensity distribution of the standing wave in the resonator mode. The coupling strength for a given cavity frequency depends on both the dipole matrix element of the atomic transition $\mu_{eg} = -e\left\langle g\right| x\left|e\right\rangle$ and on the mode volume of the cavity V, which is defined by the distance between the resonator mirrors and by the mode waist of the light in the cavity. For a given atomic species and transition, both the matrix element and the cavity frequency are fixed. To increase the coherent coupling g in this case, a cavity with a smaller mode volume has to be used. A small mode volumes and therefore high coherent coupling rates can be realized with fiber-cavity systems [98–100].

The eigenenergies of the Hamiltonian in Eq. 2.1 can be found by considering the closed subspace spanned by the states $|g, n\rangle$ and $|e, n-1\rangle$, where the first entry of the ket state indicates the state of the atomic spin and the second entry corresponds to the number of light quanta in the cavity. These states therefore describe a system having n excitations. The corresponding eigenenergies are

$$E_\pm = \hbar\omega_c\left(n - \frac{1}{2}\right) + \frac{\hbar\omega_e}{2} \pm \sqrt{\frac{1}{4}\Delta^2 + ng^2}, \tag{2.3}$$

with the detuning $\Delta = \omega_c - \omega_a$. If an uncoupled atomic spin and resonator have the same transition frequency, their energy levels of the first excited state are degenerate. If they are coupled, however, Eq. 2.3 yields for $\Delta = 0$ and $n = 1$ the energy levels $E_- = \hbar\omega_c - g$ and $E_+ = \hbar\omega_c + g$ that are split by $2g$. These hybridized excitations are called normal modes and therefore the energy split between E_+ and E_- is called the normal mode splitting or, for a single excitation, the vacuum Rabi splitting. It has first been observed in spectroscopic transmission measurements in 1992 [101] and is the basis for the state dependent interaction of a photon and the atom-cavity system in this work.

2.1.2. Input-Output Formalism for Coupled Atom-Cavity Systems

So far, it has been assumed that the coherent interaction of the atom and the light in the cavity mode is strong enough to neglect couplings to the environment. In real world examples, however, this is difficult to achieve and different dissipative channels that lead to an interaction with the environment have to be considered. Indeed, some coupling to modes outside the system is required: At least one of the resonator mirrors needs a sufficiently high transmission to allow for the necessary input and retrieval of light from and to the system. In each cavity relevant for this thesis, only one of the two mirrors is used for this in- and outcoupling of the light. Its transmission defines a dissipation rate κ_{out} for the intra-cavity field. As the coatings of the mirrors are not perfect, there are additional dissipation rates κ_{t} for the residual transmission out of the second mirror and κ_{m} for light scattering from imperfections in the mirror surfaces and coatings. In total, the
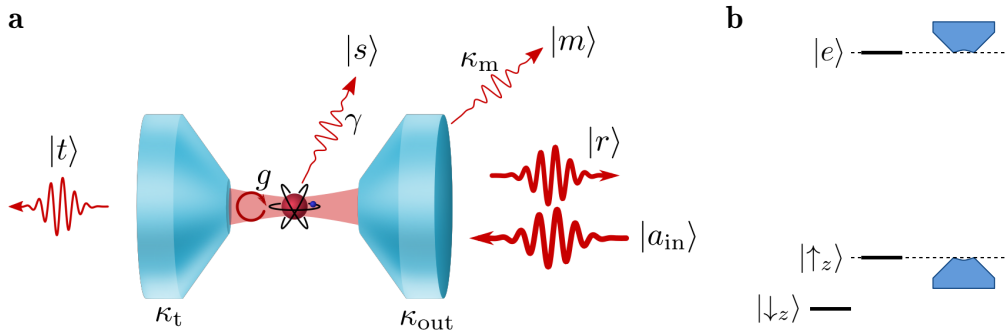
Figure 2.1.: Output modes of the atom-cavity system. a: The picture shows the various couplings to the environment κ_{out}, κ_m, κ_t, and γ and the resulting output modes for an input pulse $|a_{\mathrm{in}}\rangle$. **b**: Level scheme with the three relevant energy levels of the atom. The cavity is resonant with a transition to an excited state from one of the ground states and therefore couples to the corresponding transition.

cavity field decays with a rate of $\kappa = \kappa_{\mathrm{out}} + \kappa_{\mathrm{t}} + \kappa_{\mathrm{m}}$ giving the half width of the cavity line width. Similarly, atomic excitations decay by spontaneous emission with a rate of γ, giving the half width of the natural line width of the excited state.

The ratio between coherent and dissipative processes in the cavity is often specified in a single parameter as the cooperativity

$$C = \frac{g^2}{2\kappa\gamma}. \tag{2.4}$$

The atom is said to be strongly coupled to the cavity if $g > \kappa$ and $g > \gamma$. In this case, the dynamics of the system are governed predominantly by coherent processes and they can be aptly characterized by the bare Hamiltonian in Eq. 2.1. For a more accurate description of the atom-cavity setup, however, it has to be treated as an open quantum system. One method to describe the dynamics of it under a weak Markovian coupling to the environment is the use of a Lindblad master equation [102]. In such an approach, the environmental modes coupled to the system are traced out, resulting in effective decay channels for the system. However, for the work in this thesis, it is important to also consider the output response to the environment for incident pulses. This can be done using the input-output formalism for cavity-QED systems [103, 104].

The modes that have to be taken into account are indicated as ket states in Fig. 2.1**a**. The equation of motion for the cavity field $\hat{a}$ with a coupling spin in the Heisenberg picture is obtained under the rotating wave approximation and the Markov assumption to be [105]

$$\frac{\mathrm{d}\hat{a}(t)}{\mathrm{d}t} = \frac{i}{\hbar}\left[\hat{H}_{\mathrm{JC}}, \hat{a}(t)\right] - \kappa\hat{a}(t) - \sqrt{2\kappa_{\mathrm{out}}}\hat{a}_{\mathrm{in}}(t). \tag{2.5}$$

It describes the response of the cavity mode to an incoming field $\hat{a}_{\mathrm{in}}(t)$. If there is no coupled spin, the interaction term in the Jaynes-Cummings Hamiltonian $\hat{H}_{\mathrm{JC}}$ has to be omitted. In the experiments, we do not obtain information on the cavity field directly,

instead we measure the amplitude in the reflected output field $\hat{r}(t)$ for different input fields $\hat{a}_{in}(t)$. The relation between the in- and the output amplitude of the system is

$$\hat{r}(t) = \hat{a}_{in}(t) + \sqrt{2\kappa_{out}}\hat{a}(t), \tag{2.6}$$

therefore the output field is given by the reflected input with an additional contribution from the cavity field. As there is no incoming field in other modes, the output relations of the other channels to the environment are just given by the light leakage from the cavity mode $\hat{t}(t) = \sqrt{2\kappa_t}\hat{a}(t)$, $\hat{m}(t) = \sqrt{2\kappa_m}\hat{a}(t)$ and $\hat{s}(t) = \sqrt{2\gamma}\hat{a}(t)$. We assume two atomic ground states: $|\uparrow_z\rangle$ that couples to the cavity and $|\downarrow_z\rangle$ that has no transition resonant with the resonator mode, as shown in Fig. 2.1b. To unify the notation, $g_\uparrow = g$ and $g_\downarrow = 0$ is used. For a negligibly small excitation of the atom and slow changes of the incoming field, a steady-state solution can be derived [106, 107], yielding the following, atomic-state-dependent amplitudes for the reflection r, the transmission t, the scattering from the mirrors m and the atomic scattering s for an incoming light field of frequency ω:

$$r_{\uparrow/\downarrow}(\omega) = 1 - \frac{2\kappa_{out}(i\Delta_a + \gamma)}{g_{\uparrow/\downarrow}^2 + (i\Delta_c + \kappa)(i\Delta_a + \gamma)} \tag{2.7}$$

$$t_{\uparrow/\downarrow}(\omega) = \frac{2\sqrt{\kappa_{out}\kappa_t}(i\Delta_a + \gamma)}{g_{\uparrow/\downarrow}^2 + (i\Delta_c + \kappa)(i\Delta_a + \gamma)}, \tag{2.8}$$

$$m_{\uparrow/\downarrow}(\omega) = \frac{2\sqrt{\kappa_{out}\kappa_m}(i\Delta_a + \gamma)}{g_{\uparrow/\downarrow}^2 + (i\Delta_c + \kappa)(i\Delta_a + \gamma)}, \tag{2.9}$$

$$s_{\uparrow/\downarrow}(\omega) = \frac{2\sqrt{\kappa_{out}\gamma}g_{\uparrow/\downarrow}}{g_{\uparrow/\downarrow}^2 + (i\Delta_c + \kappa)(i\Delta_a + \gamma)}, \tag{2.10}$$

with $\Delta_{c(a)} = \omega - \omega_{c(a)}$. The reflected and transmitted modes have a well-defined phase relation to the incoming light, whereas the modes related to the mirror and atomic scattering correspond to incoherent processes with an arbitrary phase.

From the amplitudes the overall reflection $R(\omega)$ of the cavity can be derived as $R(\omega) = |r(\omega)|^2$. For an ideal mode matching[1], the spectrum for a noncoupling atom is completely defined by the reflection amplitude $r_\downarrow$ in Eq. 2.7. If there is an atom coupling to the cavity, however, its thermal motion in the trapping potential results in a position-dependent transition frequency to the excited state. In this situation, the expectation value $\langle r_\uparrow \rangle$ averaged over the distribution of Δ_a has to be used to describe the observed spectrum [108]. Fig. 2.2 shows a measured reflection spectrum of one of the two atom-cavity systems used in this thesis (labeled QGate) for both a coupling and a noncoupling atom. The solid lines give the expected spectra for the input-output amplitudes with fitted mode matching and residual thermal motion of the atom. The normal-mode splitting for the atom in $|\uparrow_z\rangle$ is clearly visible: On a resonance, the light enters the system and is dissipated into the different channels described above, resulting in a lower reflection compared to non-resonant light that is reflected with the full amplitude, as it does not enter into cavity.

---

[1]The influence of imperfections in the mode matching is described in the next section.
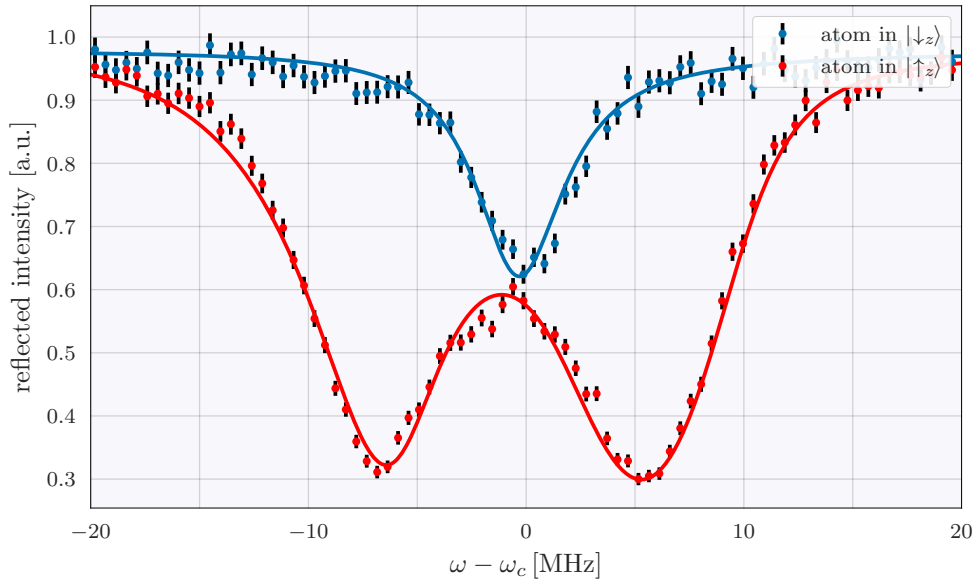
Figure 2.2.: Reflection spectrum of an atom-cavity system. The figure shows the normalized reflection spectra for the QGate cQED system introduced in detail in Chapter 3 for light of frequency ω reflected from the resonator. The atomic resonance is tuned to achieve symmetric normal modes for a given resonator frequency ω_c. Measured values are given for both a coupling atom in $|\uparrow_z\rangle$ as red data points and for an effectively empty resonator (atom in $|\downarrow_z\rangle$) in blue. The solid lines are obtained by the input-output model for the QGate system and by taking additionally into account the mode matching of two different fibers and the thermal motion of the atom.

2.1.3. Transversal Mode Matching to the Resonators

An important parameter in our experimental realizations of atom-cavity systems as light-matter interfaces is the transversal matching between the modes of the resonators and the adjoining input and pick-up fibers. For an imperfect matching, only part of an incident light pulse enters the cavity mode before leaving again through the in- and outcoupling mirror. The other part of the pulse is in an orthogonal mode and is therefore directly reflected at the first mirror. The collection of the total reflection by another non-perfectly matched fiber then picks up an interference between the two different light modes. This affects the measured spectrum and thereby also the fidelities of cQED protocols.

In [108], this situation is discussed with the same fiber being both source and pick-up. Here the more general situation with two different fibers and a nonpolarizing free-space beam splitter as a circulator is considered. A sketch of this configuration is shown in Fig. 2.3. This setup matches the arrangement at one of the two atom-cavity systems (QGate) used in this thesis. In the QGate setup, a Semrock laserline filter with a reflectivity of 1.5% at the used wavelength serves as a circulator.

The importance of good mode matchings becomes apparent when considering the effect of decreased mode matchings on the QGate cavity spectra as shown in Fig. 2.4. For these measurements, the mode of either only the input fiber (**a**) or of both the input
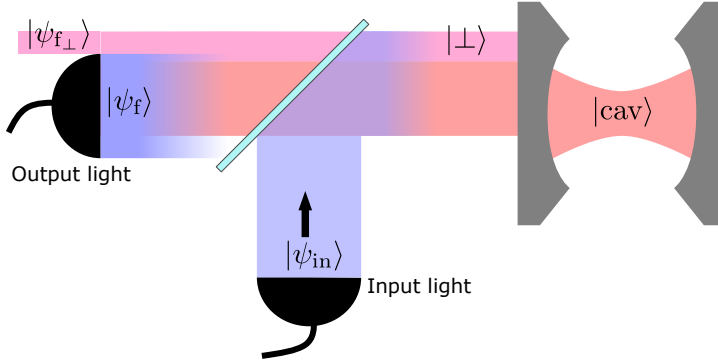
Figure 2.3.: The different light modes relevant for the mode-matching consideration. The picture shows the modes that play a role in the mode-matching consideration. The cavity is depicted in gray and the input and pick-up fibers are shown in black. The nonpolarizing beam splitter used as a circulator is shown in teal without the transmitted light from the input fiber. The differently labeled light modes are described in detail in the main text.

and the pick-up fiber (**b**) were artificially changed to reduce the matching to the cavity mode by an approximate 30 %. Compared to the optimized case shown in Fig. 2.2, the difference between the on-resonance reflectivities of the two atomic states becomes larger, which affects, for example, the fidelity of the atom-photon gate discussed in Chapter 2.2.3. Furthermore, an overall asymmetry in the spectrum can be observed, increasing the impact of frequency fluctuations in a probing laser. Both of these effects result from an increased pick-up of light that has not previously interacted with the atom-cavity system and that interferes with the wanted light mode, as described below. To achieve high fidelities with the protocols presented in this work, it is important to have very high mode matchings to limit the effect of light not interacting with the resonator mode.

The observed spectra for a coupling atom or an empty resonator depend on the two mode matchings between the cavity and either one fiber. The input light $|\psi_{\mathrm{in}}\rangle = \chi_1 |\mathrm{cav}\rangle + \sqrt{1-\chi_1^2}|\perp\rangle$ with frequency ω coming from the first fiber can be split in a part $|\mathrm{cav}\rangle$ that matches the mode of the resonator and an orthogonal mode $|\perp\rangle$. The state $|\mathrm{cav}\rangle$ reflects from the resonator with an amplitude of $r(\omega)$ given by the input-output amplitudes, whereas the orthogonal mode reflects directly with full amplitude. The reflected light state at a certain point of the resulting interference pattern is characterized by these two fields with a relative phase ϕ between them:

$$|\psi_{\mathrm{refl}}(\omega)\rangle = \left(\chi_1 r(\omega) |\mathrm{cav}\rangle + \sqrt{1-\chi_1^2}\, e^{i\phi} |\perp\rangle \right) / \mathcal{N} \tag{2.11}$$

with some normalization $\mathcal{N}$. At the second fiber, the reflected light and therefore the light fields in both the $|\mathrm{cav}\rangle$ and the $|\perp\rangle$ mode are picked up by a fiber with mode $|\psi_{\mathrm{f}}\rangle$. The relevant, normalized mode-matching coefficient for this fiber is then

$$\chi_2 = \frac{\langle\psi_{\mathrm{f}}|\,\mathrm{cav}\rangle}{\sqrt{\langle\psi_{\mathrm{f}}|\,\mathrm{cav}\rangle^2 + \langle\psi_{\mathrm{f}}|\,\perp\rangle^2}}. \tag{2.12}$$
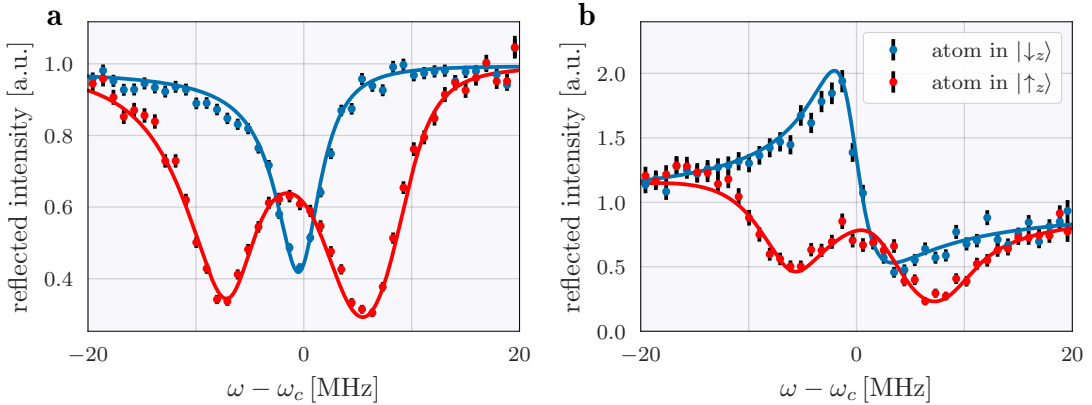
Figure 2.4.: Reflection spectrum of cavities with imperfect mode matchings. The figures each show the reflection spectra of the cavity setup from Fig. 2.2 for an artificially lowered mode matching and otherwise similar parameters. On the left, the mode matching for the input fiber was lowered by an approximate 30 %. For the picture on the right, additionally the pick-up of cavity light with the second fiber is lowered by 30 % compared to the optimal case. Interference effects between matched and unmatched light result in a final spectrum with on-resonance reflectivities that depend more strongly on the atomic state and an asymmetric spectrum compared to the more ideal case in Fig. 2.2. As discussed in the main text, these deficiencies can reduce, e.g., the fidelity of an atom-photon gate based on the reflection of a photon. The solid lines result from a fit for the QGate cavity with the model described in the present section and $\eta_1 = 0.66$ (measured as the percentage of cavity light that can couple to the input fiber). The other values for the mode matching are obtained from the fit as $\{\eta_2, \phi^*\} = \{0.98, 0.31\}$ in **a** and $\{\eta_2, \phi^*\} = \{0.91, -2.19\}$ in **b**.

In general, it can be different from the coefficient for the absolute mode matching to the cavity, $\langle \psi_f | \text{cav} \rangle$, since modes different from $|\text{cav}\rangle$ and $|\perp\rangle$ can also couple to the fiber. The reflected light that enters the pick-up fiber with the second mode-matching coefficient taken into account is then proportional to $R(\omega) \sim \left| \chi_1 \chi_2 r(\omega) - \sqrt{1-\chi_1^2}\sqrt{1-\chi_2^2}\, e^{i\phi} \right|^2$. In practice, it is useful to define the intensity mode matchings of the fibers as $\eta_1 = |\chi_1|^2$ and $\eta_2 = |\chi_2|^2$ and to absorb any additional phase from the coefficients into the relative phase ϕ^*.

Enforcing the normalization condition $R(\omega) \to 1$ for $\omega - \omega_c \to \infty$, the reflected light in the fiber is

$$R(\omega) = \frac{\left| \sqrt{\eta_1 \eta_2}\, r(\omega) - \sqrt{1-\eta_1}\sqrt{1-\eta_2}\, e^{i\phi^*} \right|^2}{\eta_1 \eta_2 + (1-\eta_1)(1-\eta_2) + 2\sqrt{\eta_1 \eta_2}\sqrt{1-\eta_1}\sqrt{1-\eta_2}\cos(\phi^*)}. \tag{2.13}$$

If the relative fraction of the light in a certain mode is relevant (for example, if the overall reflection and pick-up probability plays a role), a different normalization condition could be enforced or appropriate losses could be added. Overall, the presented calculation can describe the impact of imperfect mode matchings and is used to fit the spectra shown in Fig. 2.4 **a** and **b**. The model for the mode matching is used in simulations done for the presented work.

2.2. Quantum Information Processing with cQED Systems

The previous section laid out the main theory of cQED systems needed for this thesis, in which such atom-cavity systems are used for the distillation of single photons and to implement a nonlocal quantum gate. Such a gate is a fundamental processing operation for quantum information systems. This section first gives the basic notions of quantum information science before it describes an atom-photon gate based on the light's reflection from an atom-cavity system – a key building block for the work desribed in the later chapters. The complete field of quantum information processing with cQED system is far richer and a full description of it is beyond the scope of this chapter. A more general overview is given, for example, in [71].

2.2.1. Quantum Information

Classical bits that can assume either the states 0 or 1 are the basic information units in classical computation and are used for all processing tasks such as calculations, storage and communication. They are the fundamental constituents of global technologies like the internet and they lie at the heart of the concept of *digitalization* widely used in both politics and industry.

For many decades the progress made in computing was driven solely by the miniaturization of the physical size of the bits and their processing units. However, in the 1980s a new paradigm of computing came up [73, 76] based on the concept of quantum information. The research identified diverse problems that are hard to solve on classical machines but for which efficient algorithms were found using this new form of computing. The quantum analog to the classical bit is given by the quantum bit (qubit) that was introduced by Ben Schumacher [75]. Similar to the classical version, it can assume the states $|0\rangle$ and $|1\rangle$, but additionally it allows for any superposition of them with a defined phase relation. They can be described by a pure state

$$|\psi\rangle = \beta |0\rangle + \upsilon |1\rangle, \tag{2.14}$$

with $\beta, \upsilon \in \mathbb{C}$ following the normalization condition $|\beta|^2 + |\upsilon|^2 = 1$. The state $|\psi\rangle$ can also be interpreted as a vector in a two-dimensional, complex Hilbert space spanned by the orthonormal vectors $|0\rangle$ and $|1\rangle$. Remarkably, a measurement can generally not determine the exact state of a qubit and yields only the orthogonal states $|0\rangle$ and $|1\rangle$ with a probability of $|\beta|^2$ for the former and $|\upsilon|^2$ for the latter. Such a measurement can be performed along any two orthonormal vectors in this qubit space, but the result of each individual detection is generally probabilistic with probabilites that depend on the chosen detection basis. Each measurement projects the qubit onto the detected state and the information about its former state is lost. However, many detections of a similarly prepared qubit in various bases allow to reconstruct the underlying state that is unobservable in a single measurement.

A useful way to visualize the state of a single qubit is given by the Bloch-sphere representation. Due to the normalization condition, any pure qubit state lies on a sphere spanned between the states $|0\rangle$ and $|1\rangle$ on the poles. Examples of this representation are given in Fig. 2.5**a**.
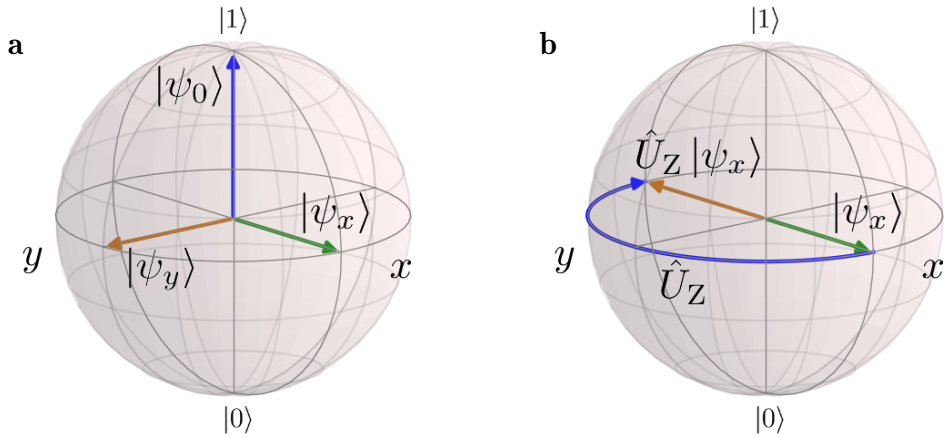
Figure 2.5.: Visualization of states and a Z-gate on the Bloch sphere. a: States representation on the Bloch sphere for the states $|\psi_0\rangle = |1\rangle$, $|\psi_x\rangle = (|0\rangle + |1\rangle)/\sqrt{2}$ and $|\psi_y\rangle = (|0\rangle + i\,|1\rangle)/\sqrt{2}$. **b:** Bloch-sphere visualization of a Z-gate acting on the state $|\psi_x\rangle$.

The description of qubits in such pure states $|\psi\rangle$ is useful to discuss underlying principles and ideal interactions in the protocols in this work. However, any real world experiment with data accumulated over many trials is more aptly characterized by the density matrix ρ.

For a system that is in different states $|\psi_i\rangle$ with probabilities p_i, it is defined as [95]

$$\rho = \sum_i p_i |\psi_i\rangle \langle\psi_i| . \tag{2.15}$$

If exactly one of the p_i is nonzero, the density matrix describes a pure state, otherwise the state described is called a mixed state. The density matrix is typically represented by a matrix: The diagonal entries of it give the detection probabilities (or populations) in the basis states of the representation and the off-diagonal terms indicate the coherences between the different terms. If a state becomes mixed, these coherences decay and the density matrix describes a statistical ensemble of different pure states. Mixed states in the laboratory can arise, for example, from different experimental runs that yield slightly different results due to fluctuating experimental parameters. Furthermore, decoherence between different states adds a time dependent source of admixing. Lastly, there can be loss of information about the state due to the interaction with unobserved degrees of freedom. In this case, the final observables of an experiment characterize only part of a larger state and can therefore only be used to reconstruct a reduced density matrix. As this does not contain all coherent interactions of the full system, there can be apparent random measurement results that need to be described by a mixed state [109]. The computer simulations used later in this thesis have been performed employing the density matrix formalism. For brevity, however, the discussion of the underlying quantum mechanism in this work is given using a description of pure states, which is also used for the remainder of this section.

The potential of quantum computing systems becomes apparent when scaling up from one to more qubits. A system of the qubit in Eq. 2.14 and another qubit in the state

$\beta' \left| 0 \right\rangle + \upsilon' \left| 1 \right\rangle$ spans a four-dimensional Hilbert space with states defined by four complex coefficients

$$\left| \psi' \right\rangle = \beta\beta' \left| 00 \right\rangle + \beta\upsilon' \left| 01 \right\rangle + \upsilon\beta' \left| 10 \right\rangle + \upsilon\upsilon' \left| 11 \right\rangle . \tag{2.16}$$

Here the first (second) number in each ket vector corresponds to the state of the first (second) qubit. Generally, for n qubits there are 2^n coefficients needed to describe the state. This exponential growth of the space dimensionality is both the reason why quantum systems are hard to simulate classically [73] and the basis of the capabilities of the quantum information processors.

To perform actual quantum computing, it is necessary to be able to manipulate and process the information stored in the qubits. Two approaches have been brought forward toward this. The concept of a one-way quantum computer is based on large entangled resource states and single qubit measurements [110]. Equivalently, a quantum circuit model of computing can be used. It is in analogy to classical computers, and the basic operations for a computation are called quantum gates. This second approach is the one that is actively pursued by, for example, Google and IBM and is also the computing model with that this thesis is concerned. The quantum gates can be represented by a unitary[2] matrix $\hat{U}$ and its effect on the state vector $\left| \psi \right\rangle$ is given by $\hat{U} \left| \psi \right\rangle$. Single qubit gates can be represented by rotations around different axes of the Bloch sphere. One example is the Z-gate (or phase gate) for one qubit described by

$$\hat{U}_{\text{Z}} = \begin{pmatrix} 1 & 0 \\ 0 & -1 \end{pmatrix} . \tag{2.17}$$

The effect of this gate on a state $(\left| 0 \right\rangle + \left| 1 \right\rangle)/\sqrt{2}$ is shown in Fig. 2.5**b**. There are furthermore two two-qubits gates that are particularly important for this thesis. The first one is a controlled-Z gate. It adds a π phase shift on one state of one qubit (the target) for a certain state of the other qubit (the control). The corresponding matrix representation is

$$\hat{U}_{\text{cz}} = \begin{pmatrix} 1 & 0 & 0 & 0 \\ 0 & 1 & 0 & 0 \\ 0 & 0 & 1 & 0 \\ 0 & 0 & 0 & -1 \end{pmatrix} . \tag{2.18}$$

The second relevant two-qubit gate is the controlled-NOT (CNOT) gate. It changes the state of the target qubit, if the control qubit is in a certain state. The corresponding matrix representation is

$$\hat{U}_{\text{CNOT}} = \begin{pmatrix} 1 & 0 & 0 & 0 \\ 0 & 1 & 0 & 0 \\ 0 & 0 & 0 & 1 \\ 0 & 0 & 1 & 0 \end{pmatrix} \tag{2.19}$$

In general circuit-based quantum computation, it is important to have a set of gates that is universal. This means that any unitary operation in the computing Hilbert space can be approximated to arbitrary accuracy by quantum circuits that involve only gates from this universal set [109]. This is possible with a combination of single qubit gates and a CNOT or a controlled-Z gate, which highlights the importance of the given two-qubit gates.

---

[2]The unitarity condition $\hat{U}^\dagger \hat{U} = I$ with identity matrix I ensures that a normalized input results again in a normalized output.

2.2.2. Qubit Labeling in this Work

In this thesis, two different physical representations of qubits are used. Both of them have an established labeling of specific states and gates, which is introduced here.

The first sort of qubit is encoded on an atom and defined by the two spin states that are labeled

$$|\uparrow_z\rangle = \begin{pmatrix} 1 \\ 0 \end{pmatrix}, \quad |\downarrow_z\rangle = \begin{pmatrix} 0 \\ 1 \end{pmatrix}. \tag{2.20}$$

Two important orthogonal superposition states of them that lie on the x-axis of the Bloch sphere are

$$|\uparrow_x\rangle = \frac{1}{\sqrt{2}}\left(|\uparrow_z\rangle + |\downarrow_z\rangle\right), \quad |\downarrow_x\rangle = \frac{1}{\sqrt{2}}\left(|\uparrow_z\rangle - |\downarrow_z\rangle\right). \tag{2.21}$$

The most common single-qubit gates for atomic qubits are rotations around specific axes and for certain angles, either as a π or as a $\pi/2$ pulses. The matrix representations of the corresponding transformations are given in Appendix A.

The second sort of qubit used in this work is encoded in the polarization of a photon. As a basis, the right- and left-circular polarizations are used

$$|R\rangle = \begin{pmatrix} 1 \\ 0 \end{pmatrix}, \quad |L\rangle = \begin{pmatrix} 0 \\ 1 \end{pmatrix}. \tag{2.22}$$

Furthermore, diagonal and antidiagonal polarizations are used extensively in this work. They are defined as

$$
\begin{aligned}
|D\rangle &= \frac{1}{\sqrt{2}i}\left(i\,|R\rangle - |L\rangle\right), \\
|A\rangle &= \frac{1}{\sqrt{2}}\left(i\,|R\rangle + |L\rangle\right).
\end{aligned}
\tag{2.23}
$$

For polarization qubits, the most common single-qubit manipulations relevant to this work are given by quarter-wave plates. Again, the matrix representation of the corresponding transformation is given in Appendix A. The polarization equivalent for the Bloch-sphere representation is called Poincaré sphere.

While this work tackles quantum information processing (QIP) tasks using neutral atoms and photons, many other systems are being actively explored. An overview over different quantum information systems can be found in [88] and [89].

2.2.3. Cavity-Induced Atom-Photon Gate

A major quantum information processing task for an atom-cavity system in the context of both a quantum network and this thesis, is to perform a gate between a flying optical photon and the stationary qubit encoded on the atom. The physics of this process is discussed in this section, using the input-output formalism introduced in Chapter 2.1.2. The reflection amplitude of the atom-cavity system described in Eq. 2.7 can have a different

sign for a coupling atom compared to an empty resonator. For a single resonant photon that impinges on the cavity, the reflections amplitudes for these two cases are

$$r_\downarrow(\omega = \omega_c = \omega_a) = \frac{(\kappa - 2\kappa_{\mathrm{out}})\,\gamma}{\kappa\gamma} \tag{2.24}$$

and

$$r_\uparrow(\omega = \omega_c = \omega_a) = \frac{g^2 + (\kappa - 2\kappa_{\mathrm{out}})\,\gamma}{g^2 + \kappa\gamma}. \tag{2.25}$$

The sign between them is different if the following two conditions are fulfilled [111]:

1. $\kappa_{\mathrm{out}} > \kappa/2$, which is equivalent to the statement that an asymmetric cavity is required (for negligible mirror losses).

2. $g^2 > (2\kappa_{\mathrm{out}} - \kappa)\,\gamma$, which is equivalent to saying that the coherent atom-light coupling needs to be sufficiently strong compared to loss rates out of the system.

The latter requirement can also be understood in terms of the normal-mode splitting discussed in Chapter 2.1.1: For a coupling atom, it changes the energy spectrum compared to an empty resonator. In this situation, a photon at frequency ω_c is not resonant with the coupled system and cannot enter the cavity. It is therefore directly reflected with the same phase as the incident photon[3]. If there is no atom coupling to the cavity, the photon enters the resonator before being reflected, acquiring a π phase shift in this process.

In the atom-cavity systems of this work, only right-circular polarization $|R\rangle$ in the cavity couples to an atomic transition (see Chapter 3.2 for details) and therefore only this polarization can be blocked from entering the resonator depending on the atomic state. Left-circularly-polarized light $|L\rangle$ does not couple and therefore always enters the resonator before being reflected. In this process, it always acquires a π phase shift on resonance independent of the atomic state. For a coupling atom, there is a difference in the phase of reflected $|R\rangle$ and $|L\rangle$ polarizations. Fig. 2.6 shows the phase shift calculated from the input-output theory of one of the cavities used in this work (QGate). It gives the phase shifts of reflected light stemming from both a coupling situation (atom in $|\uparrow_z\rangle$ and light in $|R\rangle$) and a noncoupling situation (atom in $|\downarrow_z\rangle$ or light in $|L\rangle$) and also displays the phase difference between the two situations for various detunings of the incoming light from the common atomic and cavity resonance. The phase shift of π on resonance was first used to realize a nondestructive detection of an optical photon [112], and later to implement an atom-photon gate [113].

To illustrate the effect of this gate, the approximation $r_\uparrow = -r_\downarrow$ for light on resonance with the atom and the cavity is used. In general, the equality is only true for the specific

$$g^2 = \kappa\gamma(2\kappa_{\mathrm{out}} - \kappa)/(\kappa - \kappa_{\mathrm{out}}) \tag{2.26}$$

that results in the reflection amplitudes $r_\uparrow = (2\kappa_{\mathrm{out}} - \kappa)/\kappa = -r_\downarrow$. However, it approximates well cQED setups with $\kappa_{\mathrm{out}} \gg \kappa_{\mathrm{t}}, \kappa_{\mathrm{m}}$ and $g^2 \gg \kappa\gamma$, two of which are introduced in the next

---

[3]Note that this is a convention used in this work that can be different in other texts. The observations in the lab are just related to the relative phase between directly reflected light and light entering the resonator, whereas different conventions can be chosen for the absolute phase.
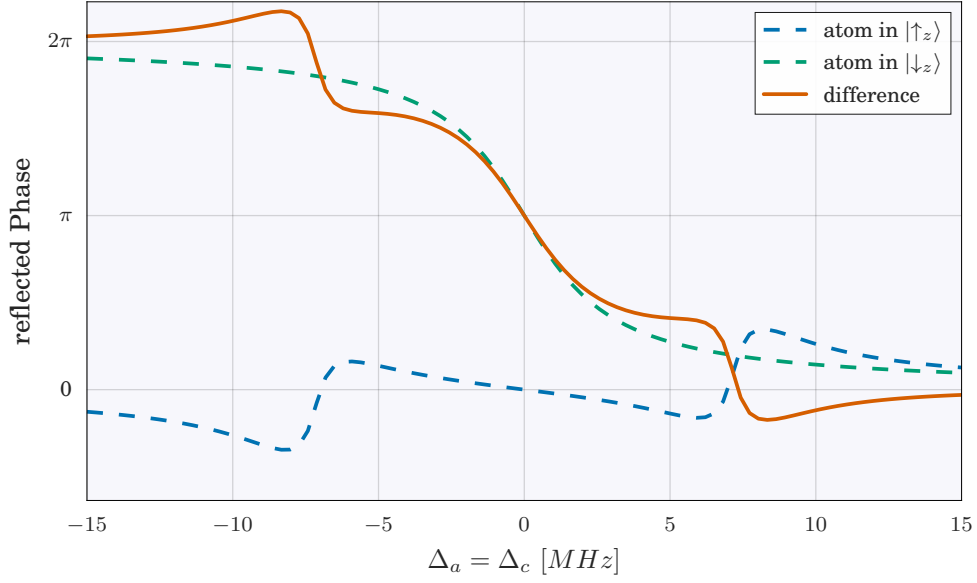
Figure 2.6.: Phase of the reflected light. The figure shows the phase of the reflected light from a cQED system with $\{g, \kappa, \kappa_{\text{out}}, \gamma\} = 2\pi\{7.6, 2.5, 2.3, 3\}$ for both a coupling atom in $|\uparrow_z\rangle$ and for an effectively empty resonator (atom in $|\downarrow_z\rangle$)) in dashed lines. The solid line gives the phase difference between the two cases that is relevant for the atom-photon gate.

chapter. This approximation is also used later to detail the further protocols implemented in this work, always in conjunction with considering the reflected light to be normalized again. If no frequency information is given in the reflection amplitudes, $\omega = \omega_a = \omega_c$ is assumed.

Using this with the atomic state $|\uparrow_z\rangle$ coupling to $|R\rangle$, the interaction of the atom in the cavity and a photon carrying a polarization qubit results in a quantum gate with the transformation

$$
\begin{aligned}
|\downarrow_z\, L\rangle &\longrightarrow -|\downarrow_z\, L\rangle \\
|\downarrow_z\, R\rangle &\longrightarrow -|\downarrow_z\, R\rangle \\
|\uparrow_z\, L\rangle &\longrightarrow -|\uparrow_z\, L\rangle \\
|\uparrow_z\, R\rangle &\longrightarrow +|\uparrow_z\, R\rangle .
\end{aligned}
\tag{2.27}
$$

As explained in the preceding section, this realizes a controlled-Z gate in the given basis [113]. This atom-photon gate is used as the integral part in the realization of the nonlocal quantum gate presented in this work in Chapter 5 [94].

Employing Eq. 2.27, the effect of the reflection of a photon in $|A\rangle$ or $|D\rangle$ is

$$
|\uparrow_z\rangle\,|A\rangle \to \frac{1}{\sqrt{2}}\,|\uparrow_z\rangle\,(i\,|R\rangle - |L\rangle) = i\,|\uparrow_z\rangle\,|D\rangle\,, \quad |\downarrow_z\rangle\,|A\rangle \to -\,|\downarrow_z\rangle\,|A\rangle
\tag{2.28}
$$

and

$$
|\uparrow_z\rangle\,|D\rangle \to \frac{1}{\sqrt{2}}\,|\uparrow_z\rangle\,(|R\rangle - i\,|L\rangle) = -i\,|\uparrow_z\rangle\,|A\rangle\,, \quad |\downarrow_z\rangle\,|D\rangle \to -\,|\downarrow_z\rangle\,|D\rangle\,.
\tag{2.29}
$$

For a coupling atom, the incoming linear polarization is changed to an orthogonal polarization in both cases, whereas the input polarization is retained for an empty cavity (or a noncoupling atom). In this way, the interaction can be used to construct a quantum CNOT gate between the atomic and the photonic qubit.

This simplified discussion of the gate assumes the same absolute value of the reflectivities $|r_\uparrow|$ and $|r_\downarrow|$. In general, slight differences in the amplitudes have to be considered. This can be done either by introducing them explicitly in a model or by calculating the fidelity overlap of the real state with the ideal state to be [114]

$$F = \frac{(|r_\uparrow| + |r_\downarrow|)^2}{2|r_\uparrow|^2 + 2|r_\downarrow|^2} = \frac{1}{2} + \frac{|r_\uparrow||r_\downarrow|}{|r_\uparrow|^2 + |r_\downarrow|^2}. \qquad (2.30)$$

3. The Quantum-Network Modules

This work uses two independent atom-cavity setups as quantum-network modules. They reside in two different laboratories at the Max-Planck-Institut of Quantum Optics and have distance to each other of 21 m. The two labs and therefore the two network modules are called "QGate" and "Pistol". After a brief historical overview of these setups, this chapter discusses the basic workings and the available toolbox for them. Unless specified differently, the discussed values refer to the QGate setup, on which I was working and which was used for the experiments on the single-photon distillation. More details on the Pistol experiment can be found, for example, in the theses of Matthias Körber [115] or Stefan Langenfeld [116].

3.1. Brief History of the Setups

Both of the setups used in the experimental work performed for this thesis have a history of several generations of doctoral researchers with a plethora of publications. In this time, the systems have been constantly improved and new tools have been implemented. Obviously, without all of this, the work presented here would not have been possible. Therefore, I want to give a non-exhaustive overview over some experiments that have been done in each setup, to exemplify both the capabilities of the setups and the foundations that had been laid prior to this work.

The construction of the QGate experiment started in 1999. Initially, it had a slightly different cavity than the one which is used now [117, 118]. In this system, the techniques for positioning, trapping and cooling were established [117]. The addition of further laser beams allowed experiments with more control of the trapped atoms, for example to implement photon-photon entanglement [119]. In 2009, the resonator of the QGate system was exchanged for the current model [118]. With this new system, the qubit state of an incoming photon was stored on the single atom in the cavity [118]. Another major improvement was the introduction of the Raman laser setup [120] that allowed fast coherent rotations in the atomic qubit space.

In 2005, the construction of the twin setup Pistol began that lead to the first combined quantum network experiments between the two laboratories. In these, the universal network modules formed by the atom-cavity systems were used for a direct state transfer between the systems, for the creation of remote entanglement and for probabilistic quantum teleportation between the setups [121, 122].

After these combined protocols, the modules were improved independently. In the Pistol setup, basic techniques for working with more than a single atom in the cavities were

pioneered and the fluorescence properties of an atom pair were studied [108]. Afterwards, the noise-related decoherence in the setup was improved to achieve a long-lived quantum memory in the atom-cavity system [115]. This and the experience with two atoms was then combined to a random-access quantum memory [116]. In the QGate setup, in the meantime, the reflection phase-shift mechanism was established with a nondestructive detection of an optical photon [123]. This lead to a quantum gate between a flying qubit encoded on a photon and the stationary atomic qubit [123] and to a heralded storage of a polarization qubit in the system [124]. The two research foci since then were on photonic states, with a photon-photon gate and the creation and analysis of optical cat states [125], and on quantum information processing with two atoms in the cavity, resulting in various techniques to entangle them and in an atom-atom gate mediated by single photon [126].

Altogether, there is already a rich experience in the two setups for different protocols of hybrid light-matter interaction, photonic and atomic state control and analysis, and even for the connection between the two systems. Many components of such a connection were adapted and changed for a better synchronization and stability between the setups, as is explained in Chapter 5. Furthermore, it has already been demonstrated that the systems enable QIP tasks with more than one qubit, an important perspective when considering the scalability of the nonlocal quantum gate introduced in that chapter.

3.2. Atomic Species for the Qubits

In both quantum network modules, single atoms are coupled to the resonator modes. The atom of choice in our setups is ^{87}Rb. As an alkali metal, it has one valence electron resulting in a comparatively simple level structure [127]. The energy levels relevant in this work lie in the near-infrared spectrum of the light which is well accessible with standard diode lasers. Both experimental setups contain a ^{87}Rb dispenser that is electrically heated to create the rubidium vapor inside the vacuum chamber.

^{87}Rb has a nuclear spin $\mathbf{I}$ with an absolute value of $I = 3/2$ [127]. It couples to the total angular momentum of the electron $\mathbf{J} = \mathbf{S} \times \mathbf{L}$ that consists of its spin $\mathbf{S}$ with $S = 1/2$ and the orbital angular momentum $\mathbf{L}$. This coupling of $\mathbf{F} = \mathbf{I} \times \mathbf{J}$ gives rise to the hyperfine energy levels with the quantum number F taking on the values $|J - I| \leq F \leq J + I$. For the $5^2S_{1/2}$ ground state, there are two hyperfine states with quantum numbers $F = 1$ and $F = 2$. They are split by a microwave transition with an energy of $h \times 6.835\,\text{GHz}$. For states in the P shell, the electron's angular momentum $\mathbf{L}$ is non-zero and its interaction with the valence electron's spin results in a fine-structure doublet with the quantum numbers $J = 1/2$ and $J = 3/2$. The transition $5^2S_{1/2} \leftrightarrow 5^2P_{1/2}$ is called the D$_1$ line and the transition $5^2S_{1/2} \leftrightarrow 5^2P_{3/2}$ is called the D$_2$ line. In our setups, we are mostly working with transitions to the $5^2P_{3/2}$ manifold. Its total electronic angular momentum couples to the nuclear spin resulting in a hyperfine splitting to levels with quantum numbers $F = \{0, 1, 2, 3\}$. The energy differences between the various hyperfine levels for the ground states and for $5^2P_{3/2}$ are given in Fig. 3.1 according to [127]. The most relevant energy levels for this thesis are two ground-state levels, namely $\left|5^2S_{1/2}, F = 2, m_F = 2\right\rangle =: \left|\uparrow_z\right\rangle$ and $\left|5^2S_{1/2}, F = 1, m_F = 1\right\rangle =: \left|\downarrow_z\right\rangle$ that form the qubit space and one excited level $\left|5^2P_{3/2}, F' = 3, m_F' = 3\right\rangle =: \left|e\right\rangle$, all of which are highlighted in Fig. 3.1.
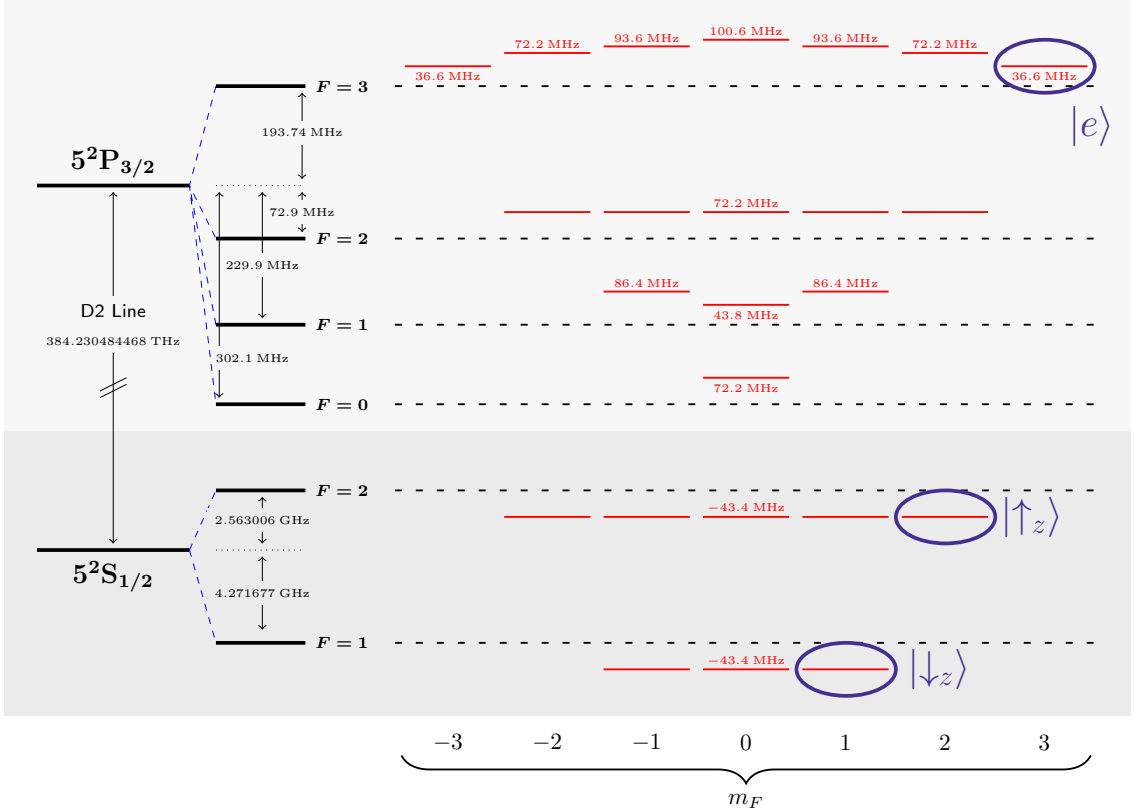
Figure 3.1.: Energy levels of ^{87}Rb. This figure shows the hyperfine energy levels of ^{87}Rb and gives the energy splittings between them. Additionally, the red states and frequencies for the different m_F sublevels indicate the calculated energy shifts that are caused by the AC Stark shift of the 1064 nm standing-wave dipole trap at a power of 1.37 W. The relevant states for the QIP protocols in this work are labeled and highlighted in purple.

In the experiments, the atoms are trapped in an optical lattice (see Chapter 3.4). The standing-wave trap along one of the axes is red-detuned with a wavelength of 1064 nm and a beam waist of 16 µm. In contrast to the other, blue-detuned traps, the atoms reside in an intensity maximum of this dipole trap. This results in a comparatively strong AC Stark effect that shifts the different energy levels [128]. This is used to create a difference in the transition frequencies between the atomic state $|\uparrow_z\rangle$ and excited states coupled to it by light being either $|R\rangle$ or $|L\rangle$ polarized. The power in the 1064 nm trap is chosen such that the transition $|\uparrow_z\rangle \leftrightarrow |e\rangle$ for light in $|R\rangle$ is shifted by a total of 80 MHz. The corresponding light shifts on all different m_F states are shown in Fig. 3.1. Ideally, those shifts are achieved for a power of 1.37 W in the trap, but, because of alignment drifts, the power to achieve them fluctuates on a timescale of months between 1.4 W and 1.7 W. As the resonance frequency of the cavity is tuned to the $|\uparrow_z\rangle \leftrightarrow |e\rangle$ transition, left-circularly polarized light in the cavity does not couple resonantly to an atomic transition.

Lastly, there is a small magnetic guiding field along the cavity axis with a magnitude of

Table 3.1.: Cavity characteristics and cQED parameters of both setups used in this work. This table lists the different specifications of the cavities and their coupling to the atom for both the QGate and the Pistol setup. The numbers correspond to the the correct locking points of the resonators that is used throughout this thesis. The atom-cavity coupling is given for the point of maximum intensity in the cavity mode.

	QGate cavity	Pistol cavity
Mirror transmissions T_1,T_2	$(92 \pm 3)\,\text{ppm}$,$(3 \pm 1)\,\text{ppm}$	$101\,\text{ppm}$,$4\,\text{ppm}$
Finesse $\mathcal{F}$	61000 ± 2000	55059
Round trip loss	$(102 \pm 3)\,\text{ppm}$	$114\,\text{ppm}$
Cavity length	$(485 \pm 1)\,\mu\text{m}$	$497.7\,\mu\text{m}$
Free spectral range	$309\,\text{GHz}$	$301.173\,\text{GHz}$
Mode waist of fundamental mode	$29\,\mu\text{m}$	$29.6\,\mu\text{m}$
Atom-cavity coupling g	$2\pi \times 7.6\text{MHz}$ ($2\pi \times 7.8\text{MHz}^2$)	$2\pi \times 7.6\text{MHz}$
Decay rate κ	$2\pi \times 2.5\,\text{MHz}$	$2\pi \times 2.8\,\text{MHz}$
Decay into outcoupling mode κ_{out}	$2\pi \times 2.3\,\text{MHz}$	$2\pi \times 2.4\,\text{MHz}$
Atomic decay rate γ	$2\pi \times 3\,\text{MHz}$	$2\pi \times 3\,\text{MHz}$
Cooperativity C	3.85 (4.06[1])	3.44

$B = 0.35\,\text{G}$, which shifts the different m_F levels by an amount of $g_F m_F B \times 1.4\,\text{MHz/G}$ [1]. Here g_F is the hyperfine Landé g factor. As these shifts are comparatively small for our magnetic field, they are not shown in Fig. 3.1. For $|\uparrow_z\rangle$, we have $g_F = 1/2$ and for $|e\rangle$, $g_F = 2/3$. Thus, the frequency f of the transition $|\uparrow_z\rangle \leftrightarrow |e\rangle$ is shifted by the magnetic field by a value of $\Delta f = 490\,\text{kHz}$. In total, the transition frequency of $|\uparrow_z\rangle \leftrightarrow |e\rangle$ and the corresponding wavelength are

$$\omega_a = \omega_c = 2\pi \times 384.228\,195\,692\,\text{THz} \quad \text{and} \quad \lambda = 780.245\,857\,439\,\text{nm}. \qquad (3.1)$$

3.3. The Resonators

The heart of each experimental setup is a high-finesse optical Fabry-Pérot cavity. The resonators enable the strong coupling between the single photons and the individual rubidium atoms that is the foundation for the experiments presented here. In order to achieve such a coupling, a high-reflection coating is deposited on the fused-silica mirrors to increase the field build-up for a single resonant light quanta in the cavity. The high reflectivities also result in low transmissivities T_1 and T_2, where the index 1 is used for the in- and outcoupling mirror of the cavity. The asymmetry between T_1 and T_2 is the reason that light from within the cavity is outcoupled predominantly in one direction – an important criterion for experiments that require, for instance, to send the light resulting from the interaction with the atom-cavity system to another network module.

---

[1]As long as the magnetic field is only a small perturbation compared to the hyperfine splitting

The most important specifications of the resonators in the QGate and Pistol setups for light at a wavelength of $\lambda = 780\,\text{nm}$ are listed in Table 3.1. More details can be found, e.g., in the PhD theses of Holger Specht [118] (QGate) and of Andreas Neuzner [108] (Pistol). The atom-cavity coupling g is derived from spectroscopic cavity measurements in transmission.

To control the resonance frequency of the cavity, the mirrors are mounted in a piezoelectric tube [117]. By adjusting the voltage, the length is set such that resonator is tuned to the frequency of the ^{87}Rb D_2 line. While the length of the cavities might only be known up to $1\,\mu\text{m}$, this uncertainty is not related to actual fluctuations of the distance between the mirrors, but to the unknown penetration depth of the cavity light-field into the multi-layer mirror coatings [125]. The length of the cavity is stabilized using the Pound-Drever-Hall locking technique [129]. For this, the intra-cavity trap laser with a frequency of $771\,\text{nm}$ (locked to a frequency comb) is modulated and its transmission is detected after the cavity. The electronic processing of the mixing and amplification of the related photodiode signal is detailed in [125]. For light after the resonator, we measure frequency fluctuations with an $1/e$ intensity half-width of $\Delta f \approx (200 \pm 50)\,\text{kHz}$. The fluctuations result from a combination of the line width of the locked laser and the length fluctuations of the resonator, and they give an upper bound for the latter: If Δf would correspond entirely to a change in the length L of the cavity, this limit was $\Delta L = L \Delta f / f = 0.25\,\text{pm}$ and thus much smaller than the size of an atom ($\approx 100\,\text{pm}$), which illustrates the precision at which the lock works.

In the QGate setup, the cavity frequency has residual drifts on the timescales of $10\,\text{min}$ resulting from the heating of the glass substrate by the $1064\,\text{nm}$ laser beam. This is compensated actively during the experimental sequence, by sending repeated pulses detuned by κ above and below the target frequency and by comparing their transmitted intensities [125].

Both resonators have a small birefringence that likely stems from strain in the mirror substrates. This results in a polarization rotation around the eigenaxes of the resonator. For QGate, the frequency difference of the modes belonging to the eigenaxes is $410\,\text{kHz}$ and the birefringence causes a rotation with an angle of $0.18\,\text{rad}$ on the Poincaré sphere around the linear polarization $50°$ from horizontally polarized light [118]. For Pistol, the measured frequency difference of the modes belonging to the eigenaxes is $415\,\text{kHz}$ and the birefringence causes a rotation with an angle of $0.178\,\text{rad}$ on the Poincaré sphere around the $|A\rangle$ polarization[3].

3.4. Experimental Toolbox

Many parts of the experimental setup in the QGate laboratory are characterized in previous PhD theses [117,118,125] and only a basic description is recounted here in order to introduce

---

[2]In the distillation experiments presented in Chapter 4, the atom-cavity coupling is the used QGate cavity was measured to be slightly larger. The corresponding value for g and C are given in brackets here and are only relevant in the distillation chapter.

[3]In the Pistol laboratory frame, the Stokes vector of the birefringence eigenpolarization is $(-0.91, -0.39, -0.04)$. In the present work, $|A\rangle$ polarization on the QGate side is matched to the eigenaxis of the Pistol resonator, resulting in the relabeling compared to the lab frame.

the available tools. Some smaller changes that were made for the work presented in this thesis are outlined in more detail.

3.4.1. Loading and Trapping

The core part of the setup is a custom-made vacuum chamber that contains the resonator and the rubidium dispenser. In the QGate lab, the dispenser is heated by a current pulse at the beginning of each attempt to trap atoms, whereas the Pistol lab uses a constant current. The produced rubidium vapor is used to load a MOT, which is located in a distance of 14 mm from the center of the cavity. To transport the atoms from the MOT into the resonator mode, a running-wave optical dipole trap at 1064 nm is utilized: It is red-detuned from the nearest optical transitions of the atom and its potential minimum is at the point of the highest intensity, i.e. at the focus of the beam. This focus is placed between the cavity and the MOT and the atoms start oscillating in the resulting potential. When they are at the turning point between the cavity mirrors, the optical traps there are switched on and the transport beam is turned off. This leads to a probabilistic loading of atoms into the cavity. On top of the vacuum chamber, an objective with a numerial aperture (NA) of 0.43 is mounted. An EMCCD camera from Andor collects light scattered from the atoms through the objective, which allows to observe the number of atoms trapped in the resonator with a resolution of 1.3 μm (see Fig. 3.2 for an example picture of the Andor camera). If too many atoms are loaded, they are optically heated until only one atom remains. If no atom is loaded, the MOT and transport sequence is repeated. The average number of atoms in the cavity can be increased with the time the dispenser is pulsed (just in the QGate setup) or with the loading time of the MOT.

In the resonator, the atoms are held in place in an optical lattice formed by retro-reflected trapping beams along three different, orthogonal axes (two for the Pistol setup): The intra-cavity trap at 771 nm that is also used to lock the frequency of the resonator, the 1064 nm dipole trap that causes the large AC Stark shifts of the atoms described above, and - for the QGate setup - a vertical standing-wave trap at 771 nm. This trapping geometry is sketched in Fig. 3.2. For Pistol, the trapping along the vertical axis stems solely from the radial confinement of the 1064 nm standing-wave trap. The interference pattern along this trapping axis can be moved in both setups by means of the phase shift caused by a rotatable glass plate to fine adjust the position of the atoms. The approximate parameters of the QGate optical dipole traps are given in Table 3.2. In the blue detuned traps at 771 nm, the atoms sit in the nodes of the standing wave. The wavelength along the resonator axis is chosen such, that the light is resonant with the cavity (15 free spectral ranges away from the frequency of the transition $|\uparrow_z\rangle \leftrightarrow |e\rangle$) and that the positions of the nodes at this frequency coincide with the antinodes of the 780 nm light in the middle of the cavity. This ensures that the atoms sit at points with a maximal intensity of the 780 nm light, which is crucial to achieve the highest possible coupling (see Eq. 2.2). Light at this coupling wavelength is derived from a laser that is locked to the same frequency comb as the 771 nm laser.

The slow sequence comprised of the initial loading and positioning of the atoms is controlled using an ADwin system. The fast sequence that governs the experimental protocol needs
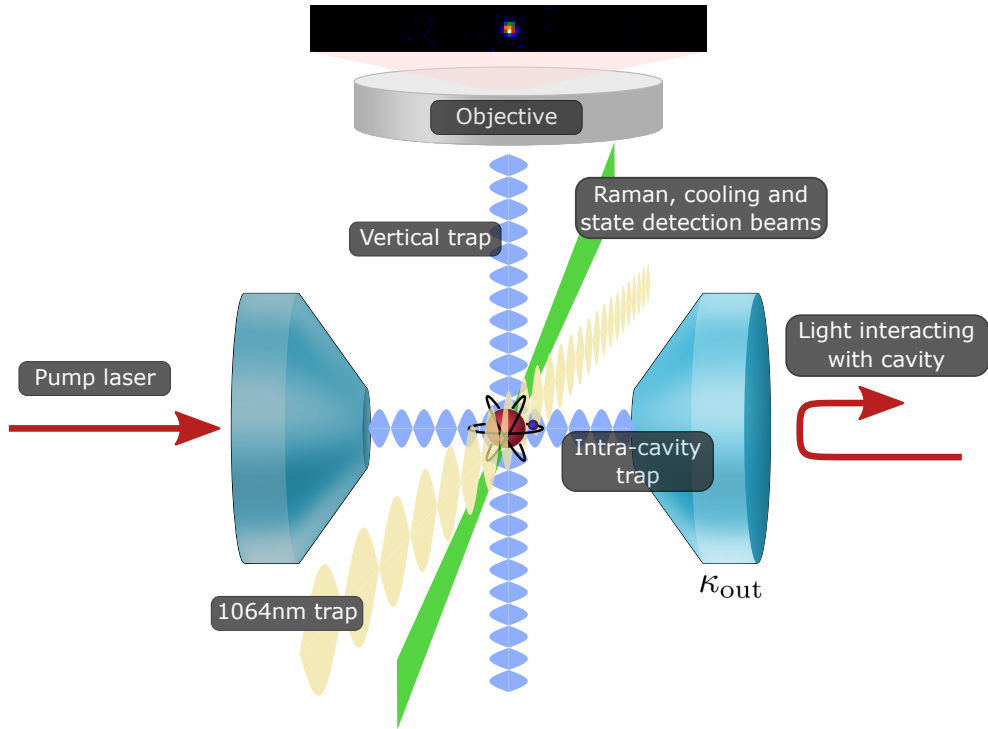
Figure 3.2.: Atom-cavity trap geometry. This figure shows the alignment of the different optical dipole traps and laser beams interacting with the atom at the center of the resonator. The position and number of the atoms in the cavity are imaged with a high NA objective from above. A typical camera picture resulting from one trapped atom is shown at the top. Pumping light is sent to the low-transmission mirror (left) and the single photons used in the protocols of this work are incident on the outcoupling mirror (right).

to be able to switch pulses on a sub- µs timescale. For this, we use field-programmable gate arrays (FPGAs) that allow to control digital outputs with a resolution of 20 ns.

During the experimental cycle controlled by the FPGAs, the trapped atoms are heated up by the interaction with resonant and near resonant light and by the scattering from the various dipole traps [128]. To maximize the trapping time of the atoms, it is crucial

Table 3.2.: Parameters of the dipole traps. This table lists the approximate parameters of the different optical dipole traps for the atoms in the QGate setup. The power of the 1064 nm trap is fine-adjusted to achieve a specific AC Stark shift (see Chapter 3.2).

Trap	Wavelength	Polarization	Power	Waist
Transfer trap	1064 nm	V	2 W	43 µm
Intra-cavity trap	771 nm	A	180 µW	29 µm
1064 nm standing-wave trap	1064 nm	π	≈ 1.4 W	16 µm
Vertical trap	771 nm	π	20 mW	8 µm

to cool them between the repeated runs of the main experimental sequence. For this purpose, the experiments use two counterpropagating cooling beams, shown in Fig. 3.2. The light is 10 MHz blue detuned from the transition frequency between $\left|5^2S_{1/2}, F = 2\right\rangle$ and $\left|5^2P_{3/2}, F' = 3\right\rangle$ without the AC Stark shifts taken into account, and it is in a lin⊥lin configuration. This results in a fast varying polarization pattern that cycles within half a wavelength and that enables a Sisyphus-cooling mechanism to dampen the atomic motion [95, 117]. Additionally, a repumping light is applied along the cooling axes, as the atom can be scattered into $\left|5^2S_{1/2}, F = 1\right\rangle$, a state in that otherwise no further cooling would occur. The cooling and repumping light beams are both derived from lasers that are locked to a frequency comb.

Typical experimental sequences run for $\approx 250 - 500\,\text{µs}$ if pumping (see Chapter 3.4.2) and the additional cavity stabilization at QGate (see Chapter 3.3) are taken into account. The experiments performed in this work have been done with repetition rates of 500 Hz and 1 kHz, respectively. The remaining time after the main experimental protocol has been taken completely to cool the atoms. With this, we achieve atom trapping times on the order of $\approx 10\,\text{s}$ in both setups.

3.4.2. Atomic State Preparation and Detection

Initially, an atom can be in any m_F ground state, either in the $F = 1$ or the $F = 2$ manifold. Prior to any experiment, the atoms are therefore pumped to the (qubit) state $\left|\uparrow_z\right\rangle$. For this, right-circularly polarized light $\left|R\right\rangle$ resonant with the $\left|\uparrow_z\right\rangle \leftrightarrow \left|e\right\rangle$ transition is sent along the cavity axis. It pumps an atom from $F = 2$ with a certain m_F level to an excited state with $F' = 3$ and $m_F' = m_F + 1$. From there the atom decays back to the $F = 2$ manifold with on average no further change of the m_F' state. Thereby, the m_F state of an atom in the $F = 2$ manifold is successively increased. Additional repumping light is incident on the atom from the side and transfers atoms in the $F = 1$ manifold back to a $F = 2$ state. When the atom has been successfully pumped to $\left|\uparrow_z\right\rangle$ with $F = 2, m_F = 2$, it couples to the resonator leading to a normal-mode splitting in the atom-cavity system. This suppresses the pumping light in the resonator and the drop of the transmitted pumping power heralds a successful pumping. At QGate, the pumping is done within $\approx 200\,\text{µs}$. This comparatively long time results from the resonance of the pumping light with both the cavity and the transition $\left|\uparrow_z\right\rangle \leftrightarrow \left|e\right\rangle$. As shown in Fig. 3.1, all other transitions from the $F = 2$ ground state to an excited $F' = 3$ state are detuned up to $\approx 50\,\text{MHz}$ from this frequency as a result of the AC Stark shifts. This slows the initial pumping to higher m_F states. For faster pumping, the power of 1064 nm trap and therefore the related AC Stark shifts can be lowered in the beginning of the pumping. This decreases the detuning of transitions with lower m_F state resulting in a faster initial pumping. However, it was found that the switch of the trapping power affects the cavity lock. As fast pumping was not required, the slower pumping was employed throughout the experiments of this thesis. Recently, in the Pistol experiment, a different approach was taken for faster pumping (within 55 µs) by using light not resonant with the cavity and by compensating the low insertion to the resonator with higher powers [116]. This could equally fasten the pumping and avoided the detrimental effect on the cavity lock.

To detect the state of the atom, light resonant with $|\uparrow_z\rangle \leftrightarrow |e\rangle$ is sent to the atom from a diagonally impinging beam (green beam in Fig. 3.2). For an atom in $|\uparrow_z\rangle$, this leads to light scattering into the cavity mode and the resulting photons leave the resonator through the outcoupling mirror. After the cavity in the QGate setup, an accousto-optical modulator (AOM) is used to allow for a fast switching of the path of the light. The first order diffraction is sent through an optical single-mode fiber to a detection setup of a beam splitter and two single-photon detectors (SPDs). Each of them is an Excelitas device with a detection efficiency of $\approx 55\,\%$ and dark-count rates of about $20\,\mathrm{Hz}$. Together with the AOM switch and the optical fiber-coupling, the overall detection efficiency of light after the QGate cavity is $29\,\%$. In the Pistol setup, the light is directed with a circulator (PMOPTICS Inc. $780\,\mathrm{nm}$ SM2) to superconducting nanowire single-photon detectors (SNSPDs) resulting in an overall detection efficiency of $50\,\%$. The dark-count rate of these detectors is dependent on the ambient light and was measured to be as low as $\approx 10\,\mathrm{Hz}$. The click signals from a photon detection in any detector are logged with a qutools quTAU time-tagging module to evaluate the time stamps of the clicks on a computer. The power in the detection beam is chosen such that the measured Poisson distribution of the photons has only a small overlap with the absence of detector clicks observed for an atom in $|\downarrow_z\rangle$ [130]. On the other hand, the scattering due to the state-detection light heats the atoms which can lead to reduced trapping times. To limit this effect on the trapping time in QGate, an active state-detection feedback has been introduced prior to the work on the nonlocal quantum gate: The registered clicks of the SPDs are counted by the FPGA and if the clicks exceed a given threshold, the state detection light is switched off, overriding possible longer detection times from the sequence.

3.4.3. Control of the Atomic Qubit States

At the end of the optical pumping, the atom is in the state $|\uparrow_z\rangle$ and therefore in the qubit space. To prepare other initial qubit states and to perform single-qubit gates, it is necessary to implement arbitrary rotations around the Bloch sphere of the qubit. For this, two copropagating Raman beams are used [120]. They have a frequency difference that equals the transition frequency between the ^{87}Rb $F = 1$ and $F = 2$ ground states of roughly $h \times 6.835\,\mathrm{GHz}$ and they therefore drive coherent two-photon transitions between the corresponding energy levels. One of the beams is π polarized, whereas the other is in a superposition of σ^+ and σ^- polarized light. Consequently, they drive two-photons transitions with $\Delta m_F = \pm 1$. To avoid the unwanted transition $|\downarrow_z\rangle = |F = 1, m_F = 1\rangle \leftrightarrow |F = 2, m_F = 0\rangle$, a small magnetic guiding field of $0.35\,\mathrm{G}$ is used to shift the different Zeeman levels. The energy difference of the transition with $\Delta m_F = -1$ is chosen such that it coincides with a minimum of the Raman spectrum[4]. The two beams have a $130\,\mathrm{GHz}$ detuning from the rubidium D_1 line and incoherent scattering can be neglected on timescales of typical state transfers.

The beams are incident diagonally on the cavity, on the same axis as one of the cooling beams (see Fig. 3.2). For the experiments performed in the single-photon distillation, the

---

[4]We use square driving pulses to switch the Raman lasers on and off via the controlling AOMs. This leads to sidebands in the frequency spectrum with defined minima in between them.
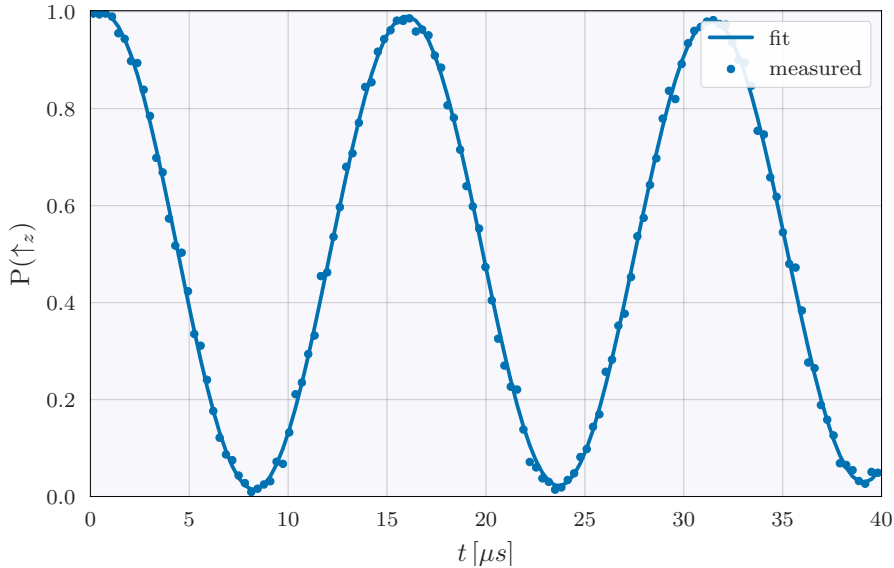
Figure 3.3.: Rabi oscillations. Measured populations in $|\uparrow_z\rangle$ over time for a continuous driving of the atom with the Raman beams. The solid line gives a fit to the data with a period of 15.4 µs and an initial amplitude of 0.989 with a decay time of 979 µs.

Raman lasers came along this axis from below. This allowed to overlap the Raman with the cooling and repumping beams directly in free-space on the optical table. However, due to space restrictions, the fiber outcoupler of the Raman beams was rather far from the atoms (approximately $\approx 1\,\text{m}$) and had to propagate via several mirrors. This limited the pointing stability of the state-control beams, affecting the effective power at the atoms and therefore the realized rotation angle. For this reason, the Raman lasers had to be readjusted daily. This not only added an overhead to the daily routine, but also made longer measurements more difficult and subjected them to larger drifts. For the nonlocal quantum gate, the Raman beams in QGate were therefore sent along the diagonal axis from the top. This required to overlap them with the cooling, repumping, and state-detection light coming from this axis on a separate breadboard and to send the combined light to the outcoupler above the resonator. As this coupler is only approximately 35 cm from the location of the atoms with no further mirrors, the pointing stability is much improved and hardly requires further adjustments. Power fluctuations are additionally stabilized by a feedback on the laser based on the measurement of the power in the Raman beams after the atom (a multi-mode fiber was chosen to pick-up the light to reduce the sensitivity on the coupling). After each experimental run, the power in both Raman beams is switched on separately and compared to the gauged value. Differences are compensated by voltage-controlled attenuator in the driving signal of the AOM for this beam.

Switching on both beams continuously, Rabi oscillations between the two qubit states can be observed (see Fig. 3.3). The combined Raman beams introduce a small AC Stark shift to the atoms of about 8 kHz. Thus, the atomic transition frequency differs when the Raman lasers are on and when they are off. To compensate this, an additional detuning

between the two lasers is switched on when they are not incident on the atoms [126]. This ensures that the phase between the two lasers and the phase between the qubit states evolves synchronized throughout the experiment. In all experiments in this work, a $\pi/2$ Rabi-pulse is performed within $4\,\mu s$.

The rotation around an axis on the Bloch sphere can be performed with any axis of rotation around the equator by switching the relative phase between the Raman beams. Furthermore, to implement rotations around the Z axis, the detuning between the two lasers can be changed by an additional Δ_R for a given amount of time. This leads to an accumulation of a relative phase of the $|\uparrow_z\rangle$ and $|\downarrow_z\rangle$ states compared to the reference system given by the Raman lasers. A combination of these two techniques allows then rotations around an arbitrary qubit axis.

4. Distilling Single Photons out of Coherent States

The content of this chapter has been published in:
Single-Photon Distillation via a Photonic Parity Measurement Using Cavity QED
S. Daiss, S. Welte, B. Hacker, L. Li, and G. Rempe,
Phys. Rev. Lett. **122**, 133603 (2019).

4.1. Motivation

Single-photon Fock states are the lowest excited photonic quantum state and therefore the most basic unit of the quantized electromagnetic field. A controlled generation of them is both of fundamental appeal and of great technological interest: Single photons have a plethora of applications ranging from quantum communication like quantum key distribution [131] or state transfer [71] to both all-optical [132–135] and distributed (see Chapter 5) quantum computing and quantum simulation [136, 137].

However, it is notoriously hard to experimentally create a single photon in a well-defined spatial mode. The source of such a radiation state is typically an open system and therefore it suffers from environmental perturbations. There are different approaches to create this elusive state, like the fluorescence of single emitters such as molecules [138, 139], ions [140], atoms [141, 142], color centers [143, 144] or quantum dots [145]. Another approach is based on weakly driven nonlinear systems using, for instance, spontaneous parametric down-conversion [146], heralded and weak excitations of a collective ensemble mode [50, 147–149] or Rydberg excitations [150, 151]. In these works, the emission of higher photon-number Fock states has efficiently been suppressed. However, the purity of the resulting state is still limited by the remaining vacuum contribution that results from both technological and conceptual constraints of the demonstrated sources.

A solution for this obstacle can be distillation, a process in which the desired state is purified from a resource, generally from a larger set of states containing the wanted contribution [59]. In the work presented in this chapter, a similar idea is employed: An incoming coherent state is used as a resource and a projective measurement of its Fock-state parity is implemented. With this technique, the unwanted vacuum and two-photon components of the incident light can be suppressed in a heralded way, thereby enhancing the target one-photon component.
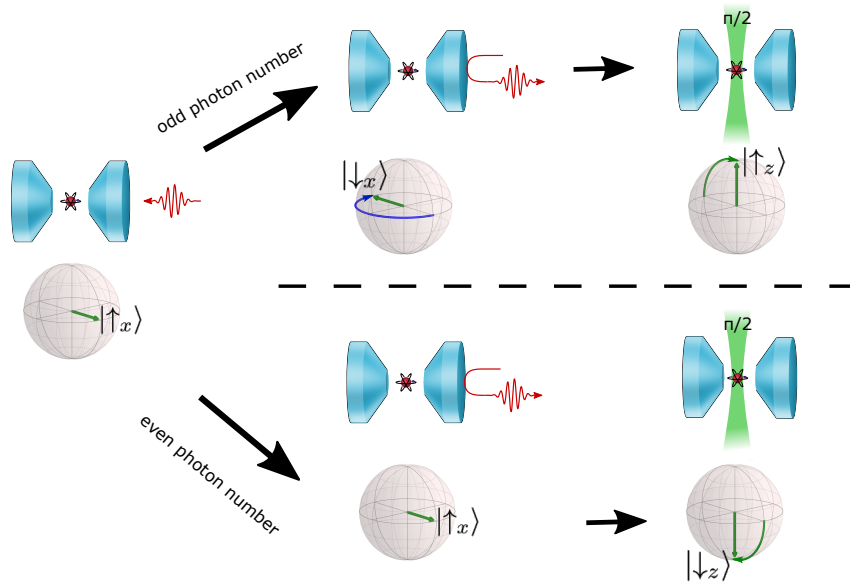
Figure 4.1.: Protocol of the photonic parity detection. The photon interacts with the atom-cavity system with the atom in $|\uparrow_x\rangle$. For an even photon number reflecting from the resonator (lower row in the figure), the state remains unchanged. A $\pi/2$ rotation maps the atomic state to $|\downarrow_z\rangle$ for the final state detection (not shown). For an incident odd photon number (upper row in the figure), there is a relative π phase between the states on the poles of the Bloch sphere. This causes a rotation $|\uparrow_x\rangle \to |\downarrow_x\rangle$. In this case, the final $\pi/2$ pulse results in the atomic state $|\uparrow_z\rangle$.

4.2. Protocol

The essential technique to distill the one-photon component out of an incoming pulse is the photonic parity measurement. It relies on the reflection of a resource light-state – containing a single-photon component – from a high-cooperativity atom-cavity system. The underlying cQED effect of this reflection mechanism is introduced in detail for single photons in Chapter 2.2.3. For the parity measurement here, the incident light is right-circularly polarized in $|R\rangle$, and it is tuned to be resonant with the empty cavity. The discussion in this section uses the approximation $r_\uparrow = -r_\downarrow = 1$ (see Chapter 2.2.3).

A single photon that is reflected from the resonator leads to a π phase shift in the atom-light state if the atom is in $|\downarrow_z\rangle$ and therefore not coupling to the cavity. This phase shift is not imprinted for a coupling atom in $|\uparrow_z\rangle$, as in this case the light is not entering the resonator. The principle can be extended to higher n-photon Fock states $|n\rangle$, where for a noncoupling atom a phase shift of $n\pi$ is caused by the reflection. Thus, for any even photon number n, this phase shift is a multiple of 2π and there is no difference caused by the different atomic states. In contrast, odd photon numbers that reflect from the cavity always result in a π phase difference in the atom-photon state between $|\uparrow_z\rangle$ and $|\downarrow_z\rangle$ [152, 153].

For the distillation, the resource states containing single-photon components are weak

coherent pulses derived from a laser. Denoting a Fock state with n photons as $|n\rangle$, these coherent states are described by [154]

$$|\alpha\rangle = e^{-\frac{|\alpha|^2}{2}} \sum_{n=0}^{\infty} \frac{\alpha^n}{\sqrt{n!}} |n\rangle,\qquad (4.1)$$

where α is assumed to be real. The average photon number in such a coherent pulse is $\bar{n} = \alpha^2$.

Fig. 4.1 sketches the full protocol of the parity measurement used for the distillation: The weak coherent pulses are reflected from the atom-cavity system with the atom initially prepared in the state $(|\uparrow_z\rangle + |\downarrow_z\rangle)\sqrt{2} = |\uparrow_x\rangle$. The reflection of a Fock state with an odd photon number results in

$$\frac{1}{\sqrt{2}} (|\uparrow_z\rangle + |\downarrow_z\rangle) \otimes |R\rangle \xrightarrow{\text{reflection}} \frac{1}{\sqrt{2}} (|\uparrow_z\rangle |R\rangle - |\downarrow_z\rangle |R\rangle) = |\downarrow_x\rangle \otimes |R\rangle. \qquad (4.2)$$

The interaction with the light changes the atomic state $|\uparrow_x\rangle$ to the orthogonal state $|\downarrow_x\rangle$. In contrast to this, the initial atomic state is not changed for the reflection of a Fock state with an even photon number. A subsequent $\pi/2$ pulse around the y-axis turns the atomic state either from $|\downarrow_x\rangle$ to $|\uparrow_z\rangle$ or from $|\uparrow_x\rangle$ to $|\downarrow_z\rangle$, depending on the previously reflected photon number [152].

Already in 2013, this effect has been used to implement a nondestructive detection of an optical photon: A weak coherent pulse was incident on the cavity with the above-mentioned atomic states and the ensuing $\pi/2$ pulse. The different atomic states resulting from the reflection of either a photon or the vacuum were used to herald that a photon interacted with the system [112]. The reflection mechanism was therein used as a detector of the existence of a single photon and the use of a nonperfect resource state - the weak coherent state - was only the convenient approximation of this single photon. In contrast, the focus of the work at hand is to use the protocol described above to change the light state with the atom-cavity system: The detection of the atom state after the interaction with the light implements a projective measurement of the photon-number parity. In order to examine the use of this principle to distill single photons, it is thus a necessary feature that an imperfect approximation of a single photon is reflected from the resonator in the first place. A projection to odd-parity Fock states then purifies the single-photon component by suppressing any even parity contribution, like for example the vacuum or the two-photon component. If the three- and higher photon contributions in the initial pulse can be neglected (for $\alpha^2 \lesssim 1$), this is equivalent to a heralded distillation of a pure single photon. To extract information on the photonic states produced with this protocol, different experimental light-state analysis tools are used that are detailed further below.

For the experiments performed in this work, the distillation protocol is run at a repetition rate of $500\,\text{Hz}$. This rate is lower than in other experiments (see for example in Chapter 5) to accommodate for the transfer speed of the homodyne data to the computer via the FPGA.

4.3. Impact of Imperfections on the Distillation

In an ideal scenario, the photonic parity measurement has a perfect contrast, i.e. a final atomic state $|\uparrow_z\rangle$ corresponds to a photonic state with only odd photon-number contributions. In this case, single photons can be produced with (near) unity fidelity. However, there are various experimental imperfections that limit this contrast in our measurements and therefore lead to an admixture of light of the wrong photon-number parity. In the following, the influence of three major error sources is discussed theoretically. These errors are included in the simulations shown with the data further below. The first two imperfections discussed here affect measurements using the homodyne detector, as these are sensitive to losses in the light state.

4.3.1. Effect of the Cavity Parameters

As described in Sec. 2.1.2, the atom-cavity system has various loss modes that can leak information about the photonic parity state during the interaction. As this information is lost to the environment, it limits the contrast of the parity measurement on a fundamental level for each set of cQED parameters. The effect of these unobserved resonator modes on the maximal achievable single-photon fidelity is discussed here.

The weak coherent input pulse $|\alpha\rangle$ is assumed to be on resonance with both the cavity frequency and the atomic transition $\omega = \omega_c = \omega_a$. Furthermore, α is assumed to be real. For an atomic state $|\uparrow_z\rangle$ ($|\downarrow_z\rangle$) and such an incoming pulse, the reflected light mode is labeled $|r_\uparrow \alpha\rangle$ ($|r_\downarrow \alpha\rangle$) and is considered to be again coherent with an amplitude of $r_\uparrow \alpha$ ($r_\downarrow \alpha$) given by the input-output formalism result in Eq. 2.7. The amplitudes of the light modes related to the transmission through the resonator $|t_{\uparrow/\downarrow} \alpha\rangle$, the light scattered from the mirrors $|m_{\uparrow/\downarrow} \alpha\rangle$ and the light scattered from the atom $|s_{\uparrow/\downarrow} \alpha\rangle$ are obtained accordingly with Eq. (2.8–2.10).

Only the reflected light is detected after the interaction and the undetected light is summarized by the loss modes $|l_\uparrow \alpha\rangle := |t_\uparrow \alpha\rangle |m_\uparrow \alpha\rangle |s_\uparrow \alpha\rangle$ for the atom in the coupling state and $|l_\downarrow \alpha\rangle := |t_\downarrow \alpha\rangle |m_\downarrow \alpha\rangle |s_\downarrow \alpha\rangle$ for a noncoupling atom. The spatial mode of light in the different modes is assumed to be independent of the atomic state. Then the overlap between the modes for the different atomic states can be calculated using the overlap of two coherent states of amplitudes α_1 and α_2 that amounts to $\langle \alpha_1 | \alpha_2 \rangle = e^{-\frac{1}{2}(|\alpha_1|^2 + |\alpha_2|^2) + \alpha_1^\star \alpha_2}$. For real values α_1 and α_2, this simplifies to $\langle \alpha_1 | \alpha_2 \rangle = e^{-\frac{1}{2}(|\alpha_1 - \alpha_2|^2)}$. Therefore, the following equations hold [125]

$$\langle r_\uparrow \alpha | r_\downarrow \alpha \rangle = e^{-2\xi^2 \alpha^2}, \tag{4.3}$$

$$\langle l_\uparrow \alpha | l_\downarrow \alpha \rangle = \langle t_\uparrow \alpha | t_\downarrow \alpha \rangle \langle m_\uparrow \alpha | m_\downarrow \alpha \rangle \langle s_\uparrow \alpha | s_\downarrow \alpha \rangle = e^{-2(1-\xi)\xi \alpha^2}, \tag{4.4}$$

$$\langle l_\uparrow \alpha | \langle r_\uparrow \alpha | r_\downarrow \alpha \rangle | l_\downarrow \alpha \rangle = e^{-2\xi \alpha^2}, \tag{4.5}$$

with

$$\xi := \frac{\kappa_{\text{out}}}{\kappa} \frac{g^2}{g^2 + \kappa\gamma} = \frac{\kappa_{\text{out}}}{\kappa} \frac{2C}{2C + 1} \tag{4.6}$$

and the cooperativity $C = g^2/(2\kappa\gamma)$ of the atom-resonator system. Inserting the QGate cQED parameters of $\{g, \kappa, \kappa_{\text{out}}, \gamma\} = 2\pi \times \{7.8, 2.5, 2.3, 3.0\}$ MHz (giving $C = 4.05$) results in $\xi = 0.819$.

In the distillation protocol, the atom is initially in an equal superposition state $(|\uparrow_z\rangle + |\downarrow_z\rangle)/\sqrt{2}$ and, after the reflection of a weak coherent pulse and the following $\pi/2$ rotation, the atomic state is measured. The probabilities to detect the atom in $|\uparrow_z\rangle$ or $|\downarrow_z\rangle$ are

$$P(\uparrow_z) = \frac{1 - e^{-2\xi\alpha^2}}{2} \quad \text{and} \quad P(\downarrow_z) = \frac{1 + e^{-2\xi\alpha^2}}{2}. \tag{4.7}$$

The corresponding light states are normalized accordingly to

$$|\psi_{\text{out}}^{\mp}\rangle = \frac{|r_\uparrow\alpha\rangle\,|l_\uparrow\alpha\rangle \mp |r_\downarrow\alpha\rangle\,|l_\downarrow\alpha\rangle}{\sqrt{2(1 \mp e^{-2\xi\alpha^2})}}, \tag{4.8}$$

where $-$ $(+)$ corresponds to the state detection yielding $|\uparrow_z\rangle$ $(|\downarrow_z\rangle)$ and thus to a light pulse that is projected on the odd (even) parity photon-number states.

The light in the loss modes is not detected and the corresponding degrees of freedom have to be traced out. This results in the reduced density matrix

$$\begin{aligned} \rho^{\mp} &= \text{tr}_l\,|\psi_{\text{out}}^{\mp}\rangle\,\langle\psi_{\text{out}}^{\mp}| \\ &= \frac{|r_\uparrow\alpha\rangle\,\langle r_\uparrow\alpha| \mp e^{-2(1-\xi)\xi\alpha^2}(|r_\uparrow\alpha\rangle\,\langle r_\downarrow\alpha| + \text{c.t.}) + |r_\downarrow\alpha\rangle\,\langle r_\downarrow\alpha|}{2(1 \mp e^{-2\xi\alpha^2})} \end{aligned} \tag{4.9}$$

that describes the state of the reflected light. The off-diagonal coherence terms in the density matrix are damped as a result of the undetected coupling to the environment. The resulting state approximates a (cat) state with a lower overall amplitude of $\sqrt{\xi}\alpha$ (defined by the normalization) that was subject to a loss of $L_c = 1 - \xi$ [125, 155]. This becomes apparent by considering a system with $r_\uparrow = -r_\downarrow =: r$ by using the condition for g^2 given in Eq. 2.26. In this situation, $\xi = (2\kappa_{\text{out}} - \kappa)/\kappa$, which is exactly the same as $r_\uparrow$. The lowered amplitudes $|\alpha\rangle \to |r\alpha\rangle$ are therefore caused by a combination of the overall smaller cat state $\alpha \to \sqrt{\xi}\alpha$ and an additional damping stemming from a loss of $1 - \xi$. The effect of general losses will be considered in more detail in the next section. The loss discussed here is intrinsic to each cavity system and ultimately limits the distillation capabilities of the protocol. Going back to the exact formula with $r_\uparrow \neq -r_\downarrow$, the fidelity F_n of the reflected light with a certain Fock state $|n\rangle$ for an incoming coherent pulse $|\alpha\rangle$ is given by

$$\begin{aligned} F_n = \langle n|\,\rho^-\,|n\rangle = \frac{1}{2(1 - e^{-2\xi\alpha^2})} &\left(e^{-|r_\uparrow\alpha|^2}\frac{(r_\uparrow\alpha)^{2n}}{n!} \right. \\ &- 2e^{-2(1-\xi)\xi\alpha^2}e^{-\frac{1}{2}\left(|r_\uparrow\alpha|^2 + |r_\downarrow\alpha|^2\right)}\frac{(r_\uparrow r_\downarrow\alpha^2)^n}{n!} \\ &\left. + e^{-|r_\downarrow\alpha|^2}\frac{(r_\downarrow\alpha)^{2n}}{n!} \right). \end{aligned} \tag{4.10}$$

The maximal single-photon fidelity $F_{1,\text{max}}$ the distillation can achieve is reached with coherent states in the limit $\alpha^2 \to 0$ and can be derived from the expression above. Practical values of F_1 will be below this limit of

$$F_1 \leq F_{1,\text{max}} = \xi = \frac{\kappa_{\text{out}}}{\kappa}\frac{2C}{2C + 1}. \tag{4.11}$$

For the QGate cavity parameters, this maximal fidelity is therefore $F_{1,\max} = 0.819$. However, there is no fundamental limit in increasing this number with different cQED parameters and different systems could use the presented protocol to distill single photons with near-unity fidelities.

4.3.2. Additional Loss

In any realistic experiment, there is not just the loss that can be associated to the cavity system, but there are additional effects that occur for example in the propagation and the detection of the light. The impact of further loss L on the light's density matrix ρ^- has two effects. First, the amplitudes reduce from $|r_{\uparrow\downarrow}\alpha\rangle \rightarrow |\nu r_{\uparrow\downarrow}\alpha\rangle)$, with $\nu = \sqrt{T}$ and $T = 1 - L$ being the transmission. Second, the off-diagonal coherence terms experience an additional decay described by a factor $e^{-2L\xi\alpha}$ [155]. The density matrix after the loss is then

$$
\rho^{\mp} = \frac{1}{2(1 \mp e^{-2\xi\alpha^2})} \Big(|\nu r_{\uparrow}\alpha\rangle \langle \nu r_{\uparrow}\alpha| + |\nu r_{\downarrow}\alpha\rangle \langle \nu r_{\downarrow}\alpha| \\
\mp e^{-2L\xi\alpha^2} e^{-2(1-\xi)\xi\alpha^2} (|\nu r_{\uparrow}\alpha\rangle \langle \nu r_{\downarrow}\alpha| + \text{c.t.}) \Big) .
\tag{4.12}
$$

For the remainder of this section, the approximation $r_{\uparrow} = r$ and $r_{\downarrow} = -r$ is again used. It was outlined in the section above that the interaction with the cavity results in an overall smaller state of $\alpha \rightarrow \sqrt{\xi}\alpha$, as apparent in the normalization, and an additional loss of $L_{\mathrm{c}} = 1 - \xi$ resulting in amplitudes of magnitude $\xi\alpha = r\alpha$. Any additional loss can therefore just be added to the impact of the cavity to arrive at the total loss $L_{\mathrm{tot}} = 1 - (1 - L_{\mathrm{c}})(1 - L)$. In this case, T is taken as $T = 1 - L_{\mathrm{tot}}$. The final overlap with a Fock state $|n\rangle$ (similar to Eq. 4.10) is then

$$
\langle n | \rho^- | n \rangle = \frac{e^{-T\xi\alpha^2}}{1 - e^{-2\xi\alpha^2}} \frac{(T\xi)^n \alpha^{2n}}{n!} \left(1 - (-1)^n e^{-2L_{\mathrm{tot}}\xi\alpha^2} \right) .
\tag{4.13}
$$

Especially for small average photon numbers, the additional loss result in a higher contribution of the vacuum in the final photonic state. In Chapter 4.5.2, loss components in our experiment are identified in the propagation and the detection of the light. As they happen only after the distillation, they are not intrinsic to the experimental realization of a specific light state (merely to its detection) and their effect can be corrected to reconstruct the state that was actually distilled. For details on this correction process see [125, 156]. Additionally, there are loss mechanisms that are intrinsic to the produced light state. For example, fluctuations of the cavity lock can result in an effective loss in the accumulated data, as the resonance frequencies differ slightly from shot to shot. The resulting variation in the phase difference between $|r_{\uparrow}\alpha\rangle$ and $|r_{\downarrow}\alpha\rangle$ causes a reduction of the contrast in the parity measurement (an effect that is not described by the approximation of Eq. 4.13). Imperfections that are intrinsic to the produced light states are not be corrected in any way.

4.3.3. Imperfect Atomic State Detection

The last major imperfection to be discussed concerns the atomic state detection. It can result, for example, from a nonperfect $\pi/2$ pulse used to rotate $|\downarrow_x\rangle$ to $|\uparrow_z\rangle$. If an atomic

state $|\uparrow_x\rangle$ after the interaction is wrongly detected as $|\uparrow_z\rangle$ after the rotation, the accumulated data for an odd-parity photon state contains also even parity data points. How much this affects the resulting state depends on the average input-photon number: For $\bar{n} < 1$ the resulting state is dominated by the vacuum, which is an even Fock state (with density matrix labeled as ρ^+). Therefore, $\alpha^2 \to 0$ yields $\langle\alpha|\rho^+|\alpha\rangle \to 1$ and accordingly $\langle\alpha|\rho^-|\alpha\rangle \to 0$. For the distillation, we are interested only in the measurements heralding an odd parity. Since these occur rarely for a small average photon number, a small detection probability of an even state being heralded as an odd parity can dominate the reconstructed density matrix. For a probability of η of the measurement to yield a wrong atomic state-detection result, the density matrix can be obtained with

$$\rho_{\text{eff}} = P_\eta(\rho^-|\uparrow_z)\rho^- + P_\eta(\rho^+|\uparrow_z)\rho^+, \tag{4.14}$$

where $P_\eta(\rho^\pm|\uparrow_z)$ is the conditional probability that an atomic detection in $|\uparrow_z\rangle$ results from an initial density matrix of the odd or even parity states for a certain η. Applying Bayes' theorem, the conditional probabilities can be rewritten as [125]

$$P_\eta(\rho^\pm|\uparrow_z) = \frac{P(\uparrow_z|\rho^\pm)P(\rho^\pm)}{P(\uparrow_z)} = \frac{(0.5 \mp (0.5 - \eta))\langle\alpha|\rho^\pm|\alpha\rangle}{P(\uparrow_z)}, \tag{4.15}$$

where $P(\rho^\pm)$ gives the probability to obtain the density matrix $\rho^\pm$ for a certain coherent input pulse $|\alpha\rangle$ (given in Eq. 4.7) and $\mathrm{P}(\uparrow_z)$ is the total probability to detect the atom in state $|\uparrow_z\rangle$ that depends on η. Therefore, the density matrix of the final state for a given α and η is

$$\rho_{\text{eff}} = \frac{1}{1 - (1 - 2\eta)e^{-2\xi\alpha^2}} \left((1-\eta)(1 - e^{-2\xi\alpha^2})\rho^- + \eta(1 + e^{-2\xi\alpha^2})\rho^+ \right). \tag{4.16}$$

In a simulation keeping track of additional imperfections, $P(\rho^\pm)$ and $\mathrm{P}(\uparrow_z)$ can be calculated by the simulation instead of taking the analytical form given here.

4.4. Photonic State Analysis

Important characteristics of single-photon sources are typically the brightness of the source, e.g. how often an attempted try to create a single photon is successful, and the indistinguishability of the produced photons [157]. In a distillation approach, however, the brightness depends on the abundance of the single-photon component in the resource state and is therefore not intrinsic to the scheme. Similarly, the indistinguishability is a result of the temporal and spectral features of the resource light used. For these reasons, the analysis of the distillation scheme that is presented here focuses only on the pureness of the single-photon component of produced light state.

For the experiments done in this chapter, two different techniques are used to analyze the distilled light after the cavity. The first technique is a homodyne detection that by virtue of different projection axes allows to reconstruct the density matrix or the Wigner function of the light. The second tool is a Hanbury Brown-Twiss detector to access the second-order correlation function of the light pulse. Both methods are introduced in this section.

4.4.1. Homodyne Detection

A useful tool to extract information on a light state is the balanced homodyne detection [158, 159] that was initially developed in the microwave technology of World War II. To implement it in the context of this work, the typically weak light signal is amplified by interfering it with a strong local oscillator (LO) beam of the same wavelength. A 50/50 beam splitter is used to channel the combined light to two independent photodiodes (PDs) of a detector that measures the current difference between them. The local oscillator is derived from the same laser as the signal to be measured and the two beams form together an interferometer. Since its path length is smaller than the coherence length of the source laser, frequency and phase noise appear equally in the signal and the LO and are therefore canceled in the detection.

Each photon individually can either be transmitted or reflected at the beam splitter and the PDs detect (and amplify) via their signal difference the corresponding fluctuations [160]. The signal is projected along a certain axis in phase space defined by the relative phase ϕ of the LO [158]. In each measurement, the current difference is integrated over the temporal shape of the photon [125] and one quadrature value q_ϕ is obtained. The distribution over many measured q_ϕ gives the full projection of the phase space along the axis given by ϕ, the so-called marginal distribution. For a full reconstruction of the signal light-state, it is necessary to get the marginal distributions of many different axes by scanning this relative phase ϕ of the LO. These marginal distributions are always the result of any measurement with the homodyne detection setup and the quantities of interest - the density matrix of the light state, its Wigner function (see below) and the overlap of the light with a certain Fock state - are derived mathematically from this data.

There are different techniques to reconstruct the density matrix or the Wigner function from the marginal distributions for various ϕ [161]. For the purpose of this work, a discrete maximum-likelihood approach was chosen to obtain the density matrix ρ of the light state in a truncated Fock space. The iterative scheme used for this was first applied to optical homodyne detection in 2004 [162] and a detailed description of it can be found in the thesis of Bastian Hacker [125]. The Wigner functions shown in this work are furthermore calculated directly from ρ as explained below. Lastly, the overlap F_n of a given light state with a Fock state $|n\rangle$ is obtained as $F_n = \langle n| \rho |n\rangle$.

4.4.1.1. The Wigner Function

An important visualization of quantum states of light is the Wigner function. It is a quasi-probability distribution in the phase space spanned by the two quadratures of the light [160, 163]. For a given density matrix $\hat{\rho}$, the Wigner function is defined as

$$W_{\hat{\rho}}(x,p) = \frac{1}{\pi} \int e^{2iyp/\hbar} \langle x+y| \hat{\rho} |x-y\rangle \, dy. \tag{4.17}$$

It is normalized to unity by integrating over the full phase space, as expected for a probability distribution. However, the Wigner function can locally be negative and is therefore called a quasi-probabilistic distribution. Regions with negative values appear only for nonclassical states of light [160].
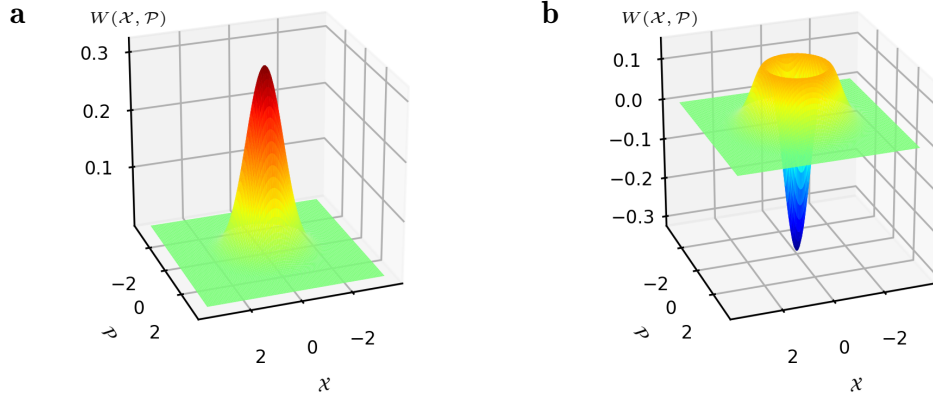
Figure 4.2.: Ideal Wigner functions. The theoretical Wigner functions of a pure vacuum (**a**) and a pure single-photon state (**b**).

There are two Wigner functions especially important for the discussion of the distilled light states, namely the vacuum and the single-photon state. They are given by the Laguerre polynomials of the harmonic oscillator and a derivation of them is outlined in Appendix B in terms of the dimensionless quadratures $\mathcal{X} = \sqrt{m\omega/\hbar}x$ and $\mathcal{P} = p/\sqrt{m\omega\hbar}$. First, the Wigner function for a vacuum state is

$$W_0(\mathcal{X},\mathcal{P}) = \frac{1}{\pi}e^{-\mathcal{X}^2-\mathcal{P}^2}. \tag{4.18}$$

It is shown in Fig. 4.2**a**. It has its maximum at the position $(0,0)$ in phase space and then shows a (radially symmetric) Gaussian decay for higher quadrature values of $\mathcal{P}$ or $\mathcal{X}$. In contrast, the Wigner function for a single-photon Fock state is

$$W_1(\mathcal{X},\mathcal{P}) = \frac{-1}{\pi}e^{-\left(\mathcal{P}^2+\mathcal{X}^2\right)}\left[1 - 2\left(\mathcal{P}^2 + \mathcal{X}^2\right)\right]. \tag{4.19}$$

The resulting radially symmetric distribution is shown in Fig. 4.2**b**. It is nonclassical, as it has a negative minimum at the phase-space origin.

These two Wigner functions show the importance of avoiding losses in a single-photon state that is to be detected: In this situation, losses are equivalent to an admixture of vacuum. Therefore, the maximum of W_0 at $(0,0)$ overlaps with the negative value of W_1 and can lift it to a positive value, thereby destroying the characteristic signature of the nonclassical state. Noise in the homodyne detection can also lead to an effective loss and therefore to a lower negativity [164].

4.4.2. Hanbury Brown-Twiss Setup

A Hanbury Brown-Twiss setup is an intensity interferometer that was introduced by Robert Hanbury Brown and Richard Q. Twiss in 1954 [165]. It probes the correlations in the

intensities of a beam at different times[1] and it is measured by two detectors with a variable time delay τ. Initially, this method was established in the field of radio astronomy. Two years later, they also demonstrated the feasibility of this method for shorter wavelengths and visible light [166, 167].

In this thesis, this technique is applied to the light signal that has interacted with our cavity and is sent via a beam splitter to two different SPDs. The second-order correlation function $g^2(\tau)$ of a light pulse can be determined as a measure of the fluctuations of the light's intensity I (or equivalently the photon number n) in time t as [102]

$$g^2(\tau) = \frac{\langle I(t)I(t + \tau)\rangle}{\langle I(t)\rangle^2}, \tag{4.20}$$

where the brackets $\langle\rangle$ denote the expectation value. Labeling the two SPDs in the output arms of the beam splitter with subscripts 1 and 2, this equation can be rewritten in terms of the probability of clicks in both detectors $P_{12}(\tau)$ that are time τ apart normalized by the probability of a click in each detector individually P_1 and P_2 as $g^2(\tau) = P_{12}(\tau)/(P_1 P_2)$. In contrast to the Wigner function, the vacuum and losses in the transmission of a single photon do not affect the detected correlation function because of this normalization. $g^2(\tau)$ has a different signature for different light states: Coherent light has a Poissonian photon distribution leading to a constant value in the second-order correlation function of $g^2(\tau) = 1$. In contrast to this, it is intuitively clear, that within each single-photon pulse at $\tau = 0$ only one (ideal) detector can click at a time and thus $P_{12} = 0$ and $g^2(0) = 0$. As the photons between different single-photon pulses that are a time τ apart are completely uncorrelated, this results in $g^2(\tau \neq 0) = 1$. The anti-bunching of the second-order correlation function at $\tau = 0$ to zero is therefore another hallmark signature of single photons [168]. Eq. 4.20 can be evaluated more generally at $\tau = 0$ resulting in

$$g^2(0) = \frac{\langle n(n-1)\rangle}{\langle n\rangle^2}. \tag{4.21}$$

Combining this equation with the probability of measuring a certain Fock state out of the distilled light after losses (Eq. 4.13) and with the effect of an imperfect atomic state detection measuring the wrong result with a likelihood of η (Eq. 4.16), the expected $g^2(0)$ for the light state produced with the distillation in the approximation $r_\uparrow = -r_\downarrow$ is:

$$g^2(0) = \left(\frac{1 - (1 - 2\eta)e^{-2\alpha^2}}{1 + (1 - 2\eta)e^{-2\alpha^2}}\right)^2. \tag{4.22}$$

Neither the transmission T nor the loss L_{tot} of Eq. 4.13 remain and $g^2(0)$ is completely independent to the effect of losses. If furthermore $\eta = 0$ is assumed, the above equation simplifies to $g^2(0) = \tanh\alpha^2$. However, if dark counts in the detectors of the Hanbury Brown and Twiss setup are present, the losses can play a role again, as they lower the real signal compared to the noise of the dark counts. To include dark counts in a simulation, the rates of three causes of coinciding clicks in the detectors have to be compared: The

---

[1]In the original experiment by Hanbury Brown and Twiss in 1956, the intensity correlations were probed transversally at different distances between two detectors.

rate of the (signal) clicks stemming from Fock-state components with $n \geq 2$, the rate of a measured click combined with a dark count in the other detector, and the rate of coinciding dark counts in both detectors during the detection window.

4.5. Experimental Setup

The distillation experiments employs the qubit module QGate that was introduced in Chapter 3. The setup used to reflect the weak coherent beams from the atom-cavity system and to subsequently analyze the resulting state is shown in Fig. 4.3. Light comes from an input fiber and uses the low reflectivity of a Semrock laserline filter to be sent to the resonator. The reflected light passes the filter and an AOM is used to send the light either via an optical fiber to a Hanbury Brown-Twiss setup (first-order diffraction) or to a homodyne detector (zeroth-order diffraction, AOM off). In the homodyne setup, a local-oscillator beam, derived from the same master laser as the signal, comes from an optical fiber and is overlapped with the light from the cavity using a 50/50 nonpolarizing beam splitter (NPBS). The power in the LO beam is 1.8 mW. It is resonant with the cavity and the diffusive reflection from the homodyne detector was sufficient to heat the atoms in the resonator. Therefore, a TOPTICA photonics SSR780 Faraday isolator is used in the signal path to block any light coming from the detection setup. It has a transmission of 97 % and a suppression from the other direction of 20 dB, which is sufficient to prevent too strong heating [125].

As outlined above, to use the homodyne detection for a full state reconstruction, it is important to have different relative phases of the LO and the input light-state. In our experiments, this is done with a detuning of 1 Hz between the signal and the LO. As the experimental sequence runs with a repetition rate of 500 Hz, this results in sufficiently many different relative phases. After each experiment, a phase- reference measurement is performed [125].

Unless otherwise specified, the experiments performed in this chapter are done with a weak coherent input pulse having a Gaussian envelope with full width at half maximum $t = 2.3\,\mu\mathrm{s}$.

4.5.1. The Homodyne Detector

Commercial homodyne detectors did not fulfill the specification we were looking for, especially concerning the quantum efficiency of the photodiodes. For this reason, I designed and assembled a custom detector. It has already been used for the work presented in the thesis of Bastian Hacker [125], and its key characteristics are also listed therein. A photo of the detector is shown in Fig. 4.4 and the relevant parts of the circuit diagram are depicted in Appendix C. For the photodiodes, the model S3883 by Hamamatsu was chosen for its high quantum efficiency. Removing the protective glass cap from the diodes, the quantum efficiencies η_{QE} of the detectors at a wavelength of $\lambda = 780\,\mathrm{nm}$ are $\eta_{\mathrm{QE}} = (98.5 \pm 1)$ %, resulting in a sensitivity of 0.63 A/W. The difference in current of the two photodiodes is amplified by a factor of 22000 with a transimpedance amplifier based on the op-amp
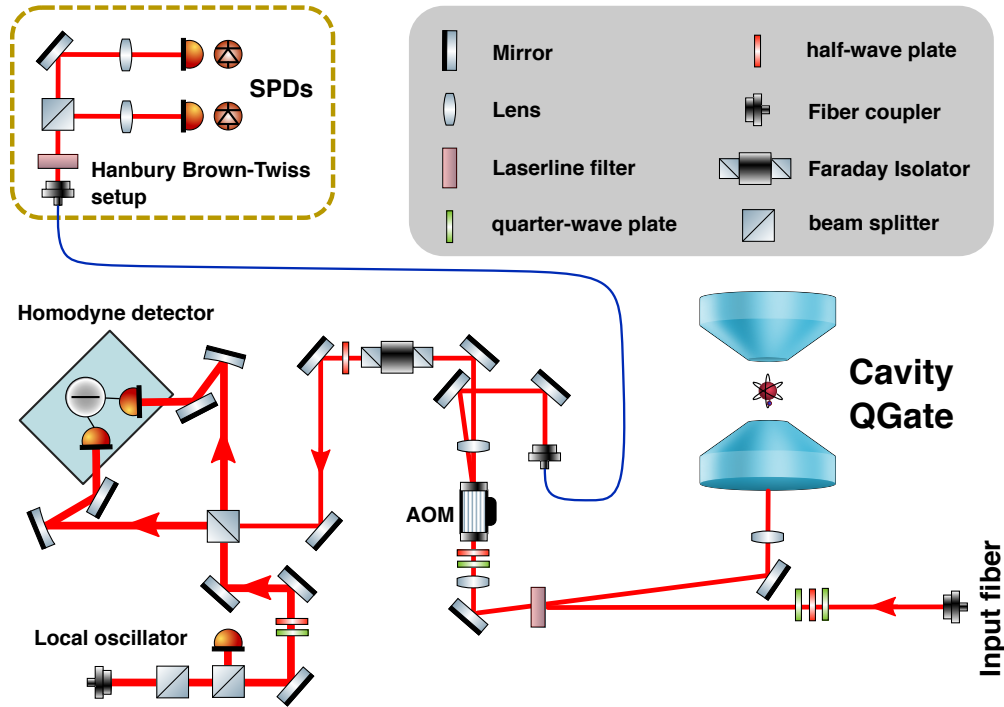
Figure 4.3.: Experimental setup for the distillation. This sketch shows the setup for the light's reflection from the cavity and the subsequent analysis of it in the distillation experiments. The light comes from the input fiber and uses a laserline filter as a circulator. With an AOM, the light can be either sent to a Hanbury Brown-Twiss setup or to the homodyne detector. The lenses, curved mirrors, and waveplates in the setup are used to set the mode and polarization of the light.

LMH6624. Stabilizing capacitances were chosen according to [169]. After a high-pass filter with a cut-off frequency of $0.7\,\mathrm{kHz}$, the signal is again amplified by a factor of 73.5 using an additional custom-built amplifier with an LMH6624 that is mounted directly on the detector (the circuit diagram of it is shown in Appendix C). For impedance matching purposes, this direct mounting is necessary and the two devices should not be connected by a coaxial cable. Furthermore, in the current configuration, the detector unit should not be used without the amplifier without changing the impedance of its output. The full system's signal is sent to an analog-to-digital converter card of an FPGA. The total theoretical gain G of a current difference in the system, including the voltage divider by the output impedance of $51\,\Omega$ and the input of the analog-to-digital converter $(50\,\Omega)$ is $G = 5.14 \times 10^5$. The gain measured with a sinusoidal input at $20\,\mathrm{kHz}$ was slightly higher at $G = (5.5 \pm 0.2) \times 10^5$, possibly due to tolerances in the used electronic parts.

4.5.2. Losses in Light Propagation and Detection

Losses that happen after a specific light state has been produced by the interaction with the cavity are summarized in this section. For a single-photon state, these losses result effectively in the admixture of vacuum and can therefore impair e.g. the negativity in
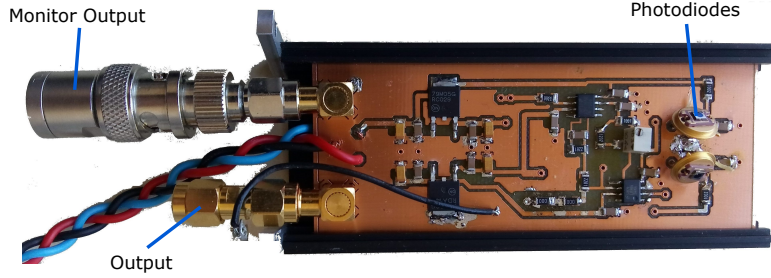
Figure 4.4.: Photo of the homodyne detector. The picture shows the final printed and assembled circuit board. The top cover of the detector unit has been removed for this picture.

the observed Wigner function. However, such losses are added only by the presented measurement setup of the light and are not intrinsic to the created photonic state. For this reason, the reconstructed state can be corrected for the losses that can be attributed solely to the specifics of the measurement setup. These losses are also discussed in the dissertation of Bastian Hacker [125], but due to their importance to the analysis in this section, a quick overview is given here as well.

There are several sources of effective loss related to the homodyne detection. The strongest contribution is caused by the imperfect mode matching of the signal and the LO beam in the two detector paths, as only signal light in the mode of the LO becomes amplified by it. This results in a loss of 6 %. Furthermore, noise in the detector adds a random component q_e to any measured quadrature q_ϕ. This is equivalent to an additional optical loss in the setup L_n [164] of

$$L_n = \frac{\langle q_e^2 \rangle}{\langle q_\phi^2 \rangle}, \tag{4.23}$$

where $\langle \rangle$ denotes the expectation value. The effective electronical noise resulting from e.g. thermal fluctuations or the spot current of the non-ideal op-amps [169, 170] can be estimated with a single measurement comparing the spectrum of the homodyne detector photocurrent with and without the incident local oscillator [164]. For the bandwidth regime of the detection (given by the high pass filter and the spectrum of the used light as roughly 0.7 kHz-500 kHz), it was found that $L_n = 0.025$. In the detection, there is additional classical noise from the laser providing the strong LO signal that leads to an effective loss L_{LO} [125]. For the used LO power of 1.8 mW, this loss amounts to $L_{LO} = 0.018$. The non-unity quantum efficiency of the photodiodes leads to an additional loss of 1.5 %. Lastly there are detection errors resulting from the use of the electronic high-pass that filters out a part of the measured spectrum.

Aside from the detection, there are losses related to the propagation of the light after the resonator. As shown in Fig. 4.3, the light passes the laserline filter, the AOM, the optical isolator, several lenses, mirrors and waveplates, and additionally the viewport of the vacuum chamber (not shown). The losses of all these mentioned imperfections are summarized in Tab. 4.1. The individual losses L_i can be summed according to $1 - L_{sum} = \prod_i (1 - L_i)$. The total identified loss related to the light propagation and detection is $L_{sum} = 25.1\%$.

Table 4.1.: Different losses in light propagation and detection. This table lists all the identified losses affecting the light state after the cavity interaction in the propagation to the measurement setup and in it its subsequent detection. The losses L_i are summed with $1 - L_{\text{sum}} = \prod_i (1 - L_i)$.

Source of effective loss	Loss L_i
Transmission through waveplates, mirrors and NPBS	7.6%
Mode matching with LO	6.0%
Transmission of the isolator	3.0%
AOM transmission	2.5%
Electronic noise of the detector	2.5%
LO laser classical noise	1.8%
Semrock laserline reflectivity	1.5%
Limited quantum efficiency of homodyne PDs	1.5(15)%
High pass filter	1.1%
Vacuum chamber viewport reflection	0.6%
Background noise of high pass filter	0.2%
Total losses L_{sum}	25.1%

4.6. Experimental Results

This section gives the main results of the single-photon distillation experiments. First, the photonic parity measurement is investigated, and then it is used to produce single photons. The generated light is analyzed for different input-photon numbers by the population in the different Fock states and additionally by a Wigner function. Lastly $g^{(2)}$ measurements underline the single-photon character of the produced light for various input-photon numbers, and it is demonstrated that the distillation can be performed for various temporal shapes of the input pulse.

4.6.1. Simulation and Characterization of the Setup

The amount of losses both from the cQED parameters and from the light transmission and detection that have been identified for the QGate setup have already been discussed. However, combined they only form a lower bound of the total losses and in the actual experiment, higher values are observed. Furthermore, the amount of the imperfect atomic state detection was not yet identified. To obtain numbers on the actual observed imperfections, a simulation is fitted to data of the populations in the different Fock states $|0\rangle$, $|1\rangle$, and $|2\rangle$. The resonator is modeled with the input-output formalism (see Chapter 2.1.2) using concatenated beam splitters [125, 153]. At the end, the transmitted and scattered light modes are traced out. To identify and fit some unknown parameters with the simulation, the distillation protocol is performed for 14 different input photon numbers $\bar{n}$ between 0.35 and 4.0 and the resulting state is analyzed with the homodyne setup. For each $\bar{n}$, an
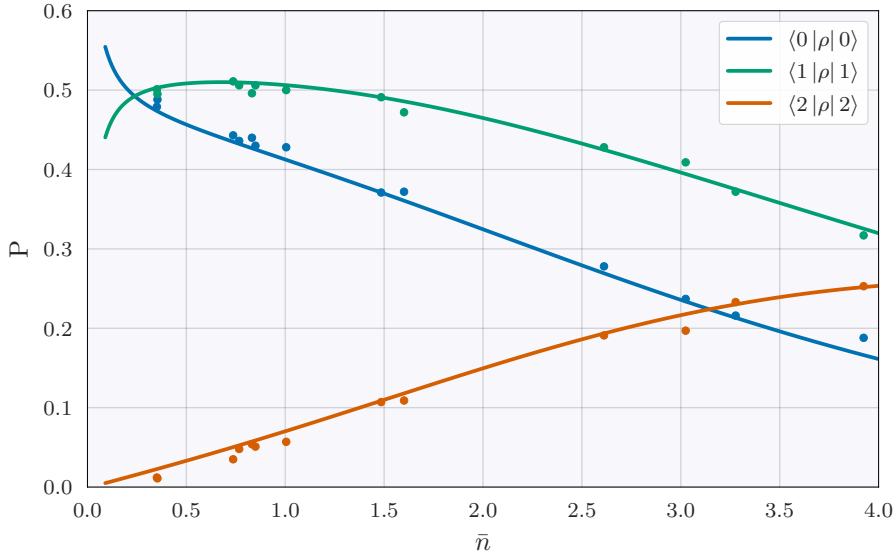
Figure 4.5.: Fitting a theoretical model the data. For an atom detection in $|\uparrow_z\rangle$, the measured and uncorrected populations P in the different Fock states $|0\rangle$ (blue), $|1\rangle$ (orange), and $|2\rangle$ (green) are reconstructed from homodyne measurements and are shown here as colored dots for different average photon numbers of the incoming coherent pulse $\bar{n}$. The curves with the respective colors give the calculated overlap of the density matrix in the simulated model with the different Fock states for the parameters discussed in the main text.

average of $22\,000$ quadrature values have been measured for the detection of the atomic state in $|\uparrow\rangle$. From this data, the different Fock-state contributions are reconstructed with the maximum-likelihood approach. The simulated model of the parity measurement is implemented in QuTip [171]. It includes as free parameters the total losses after the interaction with the cavity L_{fit}, the probability of a wrong state-detection outcome η and the detuning of the light from the cavity frequency Δ_c. The detuning of atomic transition from the incoming light was found to have only a small effect. It was set to a constant value of $\Delta_a = 2\pi \times 6\,\text{MHz}$, resulting from a separate characterization that includes additional AC Stark shifts of residual atomic motion in the standing-wave dipole traps [108].

The fit of this model to the measured data is shown in Fig. 4.5. It results in the parameters $L_{\text{fit}} = 35.2\,\%$, $\eta = 0.013$, and $\Delta_c = 2\pi \times 0.39\,\text{MHz}$. The values for η and Δ_c are used for the simulations given below, unless otherwise specified. Concerning L_{fit}, the experimental data based on the homodyne detection is corrected for the identified losses in propagation and detection of $L_{\text{sum}} = 25.1\%$. This leaves losses of $L_{\text{uncorr}} = 1 - (1 - L_{\text{fit}})/(1 - L_{\text{sum}}) = 13.5\%$ that remain in all presented data and that are used in the simulations. They might stem, for example, from fluctuations of experimental parameters in the production process of the light.
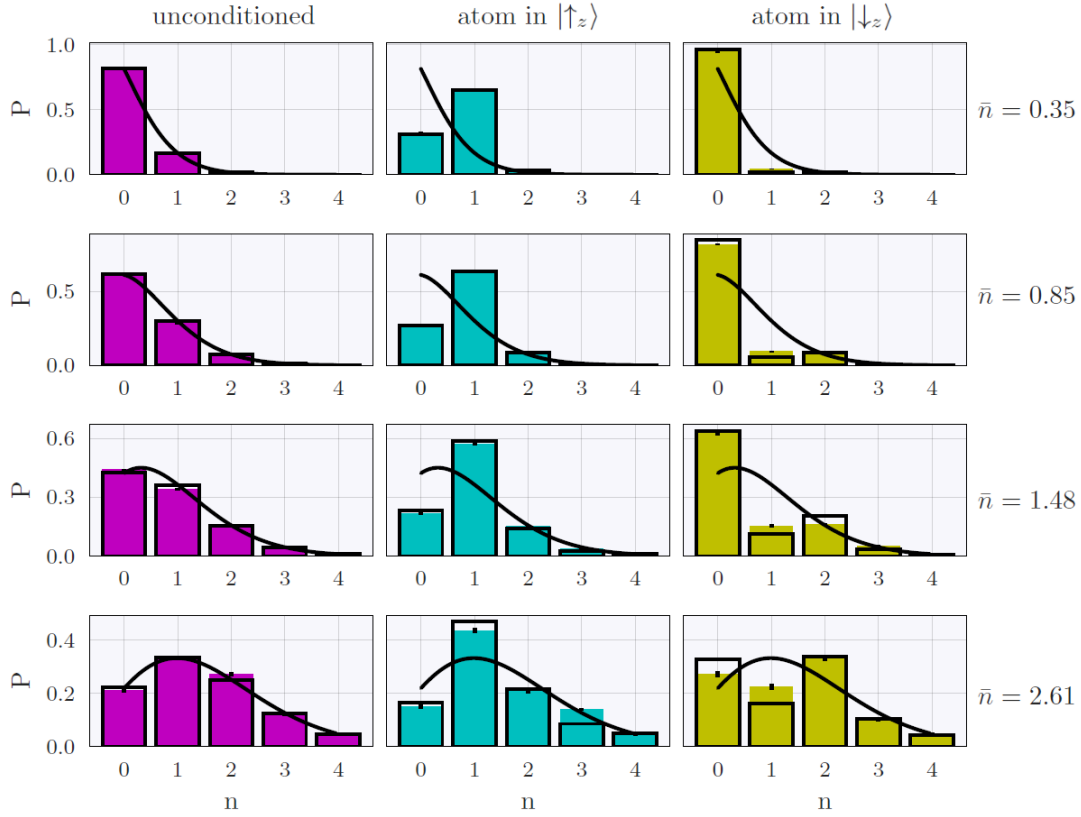
Figure 4.6.: Effect of the parity measurement on the photon distribution. For input pulses with different average photon numbers, the output photon-number distribution after our protocol is shown as reconstructed from the homodyne measurement. In the first column, it is given unconditioned on the atom measurement. The middle column shows the distribution for an atomic state detection in $|\uparrow_z\rangle$ and the last column for a detection in $|\downarrow_z\rangle$. The black line indicates a Poisson distribution with an average photon number given by the unconditional distribution. The input-photon numbers in the different rows are indicated on the right side of the figure. The black contours give the distribution expected from the simulation. The values shown here are corrected for losses occurring in the propagation and detection.

4.6.2. The Photonic Parity Measurement

For an incoming weak coherent pulse $|\alpha\rangle$ with an average photon number of $\bar{n} = \alpha^2$, the parity measurement heralds a projection onto the odd-parity states by measuring the atom in $|\uparrow_z\rangle$. Similarly, even-parity states are heralded by the atom being in $|\downarrow_z\rangle$ at the end of the sequence. In Fig. 4.6, photon distributions reconstructed from the homodyne detection are shown without postselection on an atomic state and for the atom detected both in $|\uparrow_z\rangle$ and $|\downarrow_z\rangle$. As a basis of the reconstruction, an average of $95\,000$ quadrature values have been recorded per input-photon number. The data is corrected for the losses in the propagation and detection of the final light state after the interaction with the cavity. The enhancement
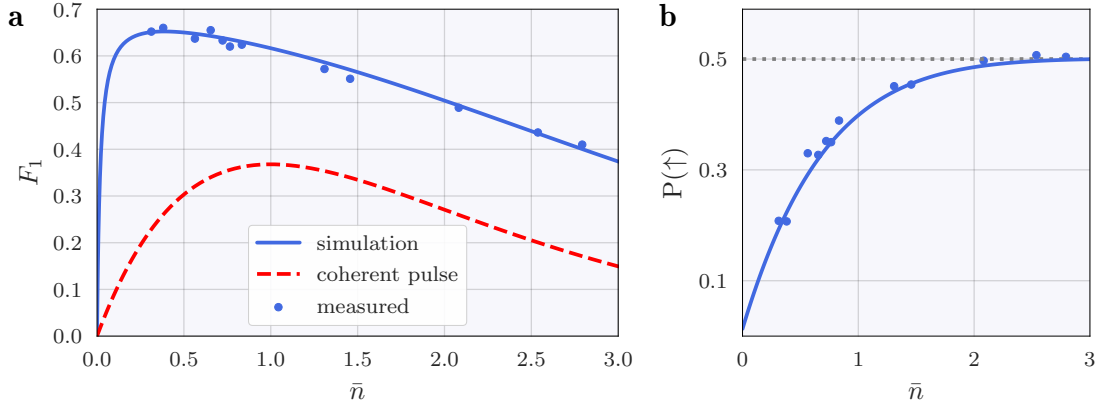
Figure 4.7.: Overlap fidelity with a single photon. a: The measured overlap fidelity F_1 of the distilled light state with a single-photon Fock state reconstructed from a homodyne measurement is shown in blue markers for different input photon numbers $\bar{n}$. The measurements are corrected for losses in propagation and detection. The blue line corresponds to a simulation using the major experimental imperfections. For reference, the overlap of a coherent state of a given photon number with a single-photon state is shown. **b**: The probability of detecting the atom in $|\uparrow_z\rangle$ after the distillation protocol is shown as a function of the input-photon number. The solid line corresponds to a simulation and the blue markers give the measured values per distillation attempt.

of the odd (even) photon contributions for a detection in $|\uparrow_z\rangle$ ($|\downarrow_z\rangle$) compared to the unconditioned distribution is clearly visible. The experimental imperfections discussed above result in a nonperfect separation to the different parity states. A simulation including these imperfections yields the distributions given by the black contours in the figure. They represent well the measurements for smaller average photon numbers. The small deviation for larger photon numbers could be caused by non-linearities in the system and by the fact that the interaction of the light pulse with the cavity happens while part of light is already being detected. However, they do not play a role for the theoretical understanding of the distillation to single photons for that light with small average photon numbers is used.

In all the results for a post-selection in $|\uparrow_z\rangle$, the relative suppression of the vacuum and the two-photon component are apparent. Together with the negligible low population of the three photon state for small $\bar{n}$, this is the key to using the parity measurement to produce single photons.

4.6.3. Distillation of Single Photons

The combination of a coherent input pulse with a small average photon number and a following projection to an odd-parity state constitutes the single-photon distillation. The output fidelity of its measured light state ρ with a single photon (given by the overlap $F_1 = \langle 1| \rho |1\rangle$) is shown in Fig. 4.7**a** (corrected for losses in propagation and detection) for different average input photon numbers $\bar{n}$. It is reconstructed from homodyne measurements using an average of 22 000 quadrature values. The solid line gives F_1 as expected from the theoretical simulation, which matches well with the data. As a reference, the single-photon
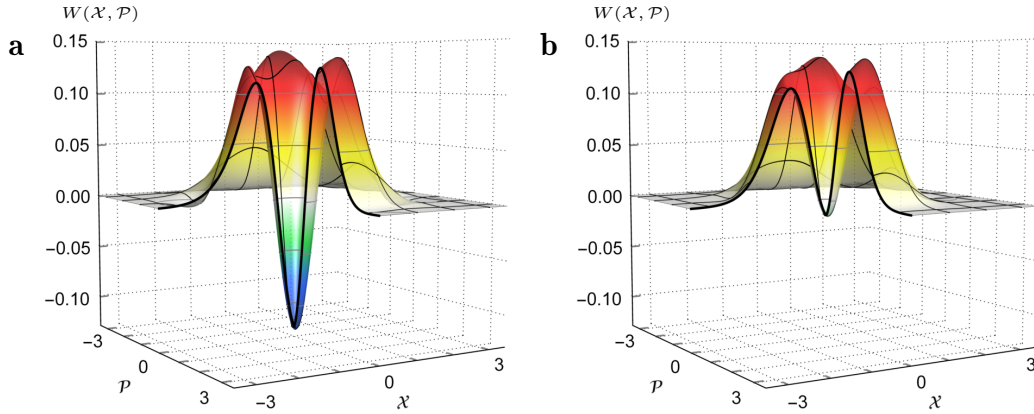
Figure 4.8.: Wigner function having a high overlap with a single-photon state. The figure shows the Wigner functions reconstructed from the homodyne measurements for an input average photon number of $\bar{n} = 0.31$. For a better visibility, part of the function is cut to display the center of the distribution. **a**: Wigner function that is corrected for losses occurring in propagation and detection. **b**: Wigner function as reconstructed from the measured marginal distribution without any further corrections.

fidelity F_1 of a coherent state is also shown in the figure. Such states are used in many quantum-network protocols to approximate single photons. While the coherent state achieves a maximal overlap of $F_1 = 36.8\%$ with a true single photon, the light state produced after the cavity reaches up to $F_1 = (66 \pm 1)\%$. This maximum is achieved for $\bar{n} \approx 0.5$. If the input-photon number increases compared to this value, the contributions from the higher Fock states result in a slow decrease of F_1. For $\bar{n} \to 0$, F_1 also decreases. This is due to the atomic state detection ($\pi/2$ rotation and state detection in $|\uparrow_z\rangle / |\downarrow_z\rangle$) yielding the wrong result in 1.3% of the cases. As the input pulses are dominated by the vacuum, there are fewer detections for an odd parity and the atom in $|\uparrow_z\rangle$. This is shown in Fig. 4.7**b** as the measured probability to detect the atom in this state, $P(\uparrow)$. The lower number of overall detections for small $\bar{n}$ leads to an increased impact of the small percentage of state detections with the wrong result for an atom that should ideally be detected in $|\downarrow_z\rangle$. This yields a lowered F_1 as $P(\uparrow)$ drops.

At the point of the highest fidelity F_1, the Wigner function of the photonic state is reconstructed from the homodyne data out of $7\,500$ quadrature values. In contrast to the results shown before, this analysis also contains information on the off-diagonal elements in the density matrix of the state. Therefore, this representation is a means to show the full state produced by the distillation protocol. The result of this reconstruction for an incoming photon number of $\bar{n} = 0.31$ is shown in Fig. 4.8. The Wigner function in Fig. 4.8**a** is corrected for losses in propagation and measurement. It clearly shows the dip in the middle of the distribution that is characteristic for a single photon, albeit it is with a value of -0.125 ± 0.006 less negative than in the ideal Wigner function ($W_{1,\text{ideal}}(0,0) = -1/\pi$) displayed in Fig. 4.2. This is expected due to the additional losses, the atomic state-detection error, and the contributions of higher photon numbers. The Wigner function of
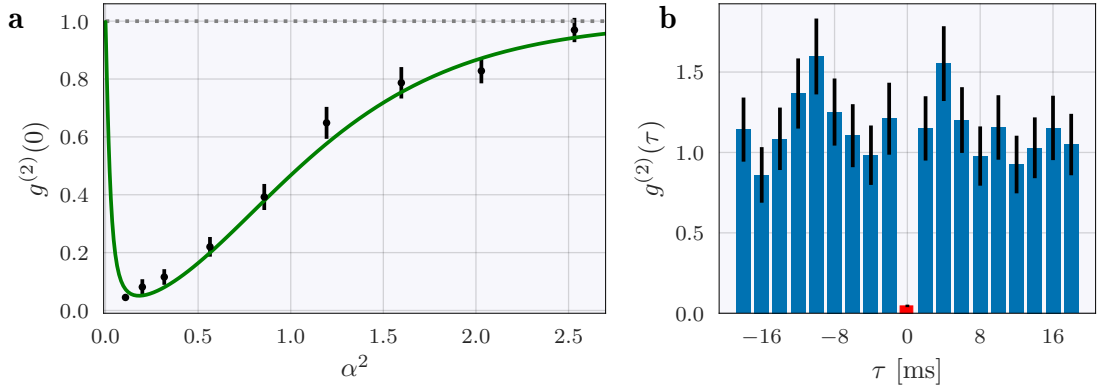
Figure 4.9.: Second-order correlation function measured with the Hanbury Brown and Twiss setup. a: The measured values of $g^{(2)}(0)$ for different average input-photon numbers $\bar{n}$ are shown as black markers. The green curve shows $g^{(2)}(0)$ of the simulated model with the parameters given in the main text. **b:** The measured $g^{(2)}(\tau)$ between the different coherent input pulses that are separated by 2 ms. The errors in both plots are given as black bars and display the standard deviation.

a photonic parity measurement that is subject to these imperfections is discussed in the thesis of Bastian Hacker [125]. At the phase-space origin, its value is

$$W_{\text{theo}}(0,0)(\alpha) = \frac{e^{-2(1-L)\xi\alpha^2} - (1-2\eta)e^{-2L\xi\alpha^2}}{\pi\left(1 - (1-2\eta)e^{-2\xi\alpha^2}\right)}. \tag{4.24}$$

with losses of L and a probability η that the detection of the atomic state yields a wrong result. The losses to be taken into account are caused by the cavity with $L_c = 1 - \xi$ and there are additional, uncorrected losses of $13.5\,\%$, as discussed further above. Using these values at $\alpha = \sqrt{0.31}$, the theoretical negativity of our state expected from Eq. 4.24 is $W_{\text{theo}}(0,0) = -0.109$ and therefore very close to the measured value. Furthermore, the detected Wigner function shows the overall radial symmetry expected for a single photon with a some vaccum contribution. The small deviations from the expected Wigner function can result, for example, from fluctuations of the cavity frequency between different experimental runs. In Fig. 4.8**b**, the Wigner function for the same data is shown without the corrections applied. In this case, there is still a small negativity of -0.016 ± 0.008 at the center of the distribution, but the vacuum component almost suppresses this characteristic of a nonclassical state. With the combination of the fitted losses and the cavity effects, the theory in Eq. 4.24 results in $W_{\text{theo}}(0,0) = -0.004$, confirming that the expected negativity is almost negligible for the given experimental parameters.

If incident weak coherent pulses with even smaller average photon numbers are to be considered, the probability of detecting the wrong atomic state leads to a higher admixture of even-parity contributions and the detected state in the homodyne setup becomes dominated by the vacuum component. To characterize the ability of the distillation protocol to suppress higher-photon numbers in a loss independent way that is less sensitive to the vacuum contribution, the light is analyzed with the Hanbury Brown-Twiss setup. The detection efficiency of light from after the cavity to a final detection with it is $47\,\%$. As

the correlated clicks are normalized with the individual clicks occurring in each detector, the impact of the vacuum on the resulting state is excluded in this approach. The value of the second-order correlation function $g^{(2)}(0)$ at $\tau = 0$ of the distilled light for incoming intensities between $\bar{n} = 0.1$ and $\bar{n} = 2.5$ is shown in Fig. 4.9**a**. For the different datapoints (with the exception of the data at $\bar{n} = 0.1$, see below), an average number of 3 000 clicks was recorded with the single-photon detectors. A clear sub-Poissonian photon statistics as characterized by a reduction in the count fluctuations $g^{(2)}(0) < 1$ is visible. As expected due to the vanishing higher-photon contributions, the figure shows $g^{(2)}(0) \to 0$ for $\bar{n} \to 0$. For very small incoming intensities in the coherent input pulse, the distilled light therefore exhibits the photon statistics expected for a single photon. Fig. 4.9**a** additionally shows a curve resulting from a simulation of the expected $g^{(2)}(0)$ with the experimental parameters in the setup[2]. The increase of $g^{(2)}(0)$ for very small $\bar{n}$ is a result of the dark-count rate of the SPDs of 20 Hz during the detection window of 5 μs. This effect is additionally included in the simulation. For very small detection probabilities, a click in a detector becomes more likely to be an uncorrelated random dark count, increasing $g^{(2)}(0)$. This effect poses a limit on the minimal achievable value measured with our distillation setup.

The lowest recorded value is $g^{(2)}(0) = 0.045 \pm 0.006$ for $\bar{n} = 0.11$. To measure this value accurately, a total of 11 000 clicks were recorded in the detectors for incoming light with this average photon number. Using Eq. 4.22 with $\eta = 0.013$ for the corresponding $\alpha = \sqrt{0.11}$, a theoretical value for the second-order correlation function without the effect of the dark counts $g^{(2)}(0)_{\text{no dc}}$ can be derived including the effect of the incorrect atomic state detection η. This results in $g^{(2)}(0)_{\text{no dc}} = 0.010$ and shows thereby that the main deviation of the measured value from zero results from the dark counts of the detectors and not from the nonzero α or the state detection error rate η.

At the average photon number of $\bar{n} = 0.11$, additionally the correlations between the produced pulses in different experimental runs separated by 2 ms are analyzed in Fig. 4.9**b**. It shows that $g^{(2)}(\tau \neq 0) \approx 1$ and confirms therefore that the low $g^{(2)}(0)$ within one pulse corresponds to an antibunching of photons. In combination, the results shown in Fig. 4.9 confirm that the distillation operation suppresses the two-photon contribution of the initial light state.

The temporal shape of the incident pulse in the experiments so far was a Gaussian with full width at half maximum of 2.3 μs. It is created by controlling the radio frequency (RF) power of the AOM in the beam path of the input light and therefore other shapes can be easily set in our setup. This allows to use the distillation protocol with input light of various temporal profiles. If the changes in a pulse are small on timescales defined by the cavity decay rate κ, the temporal shape of the distilled single photons is defined completely by this input pulse. In contrast to this, for instance, the creation of single photons with adiabatic transfer methods requires the inversion of nontrivial functions and an accurate control of the coupling laser to generate tailored photon shapes [172]. This hinders a flexible approach to adapt photon shapes to, for example, distortions in different quantum channels, as the temporal form is completely predefined by the control. The distillation protocol, however, does not require a precise a-priori knowledge of the pulse shape that is to

---

[2]Here $\Delta_c = 0$ as the stabilization of the cavity frequency introduced in Sec. 3.3 has been implemented prior to this measurement.
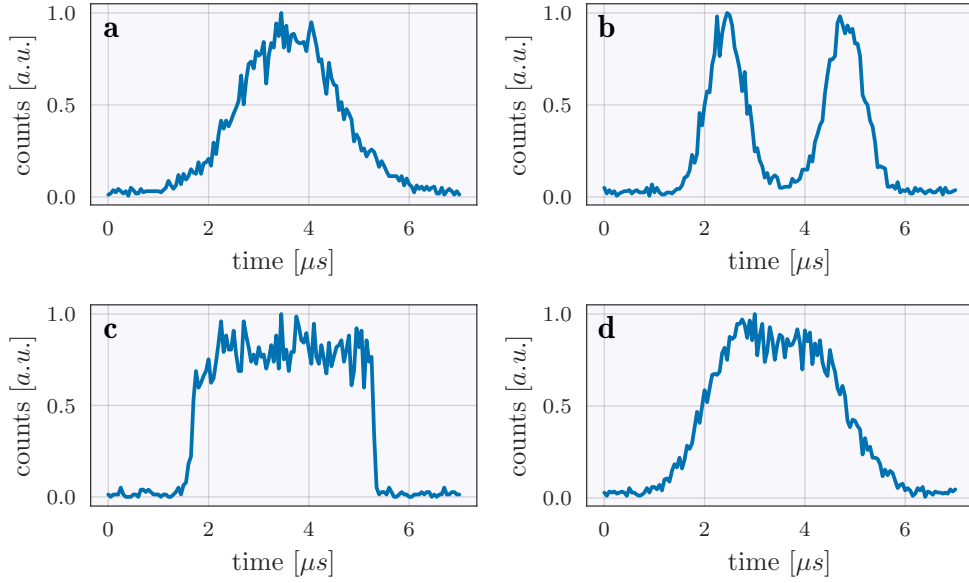
Figure 4.10.: Input pulse shapes. This figure shows the different temporal profiles with that single photons have been created using the distillation protocol. The labeling letters correspond to the quoted values for the second-order correlation function given in Table 4.2.

be distilled, as long as the spectral width of it supports an efficient phase-shift mechanism in the cavity. This is highlighted by distilling single photons with four different pulse shapes shown in Fig. 4.10. The use of these pulses each with an average photon number of $\bar{n} = 0.11$ results in very low values of $g^{(2)}(0)$ (derived from 1 900 detector clicks on average) given in Table 4.2 as expected for a single photon.

4.7. Perspective and Outlook

With the measurements discussed above, it has been shown that our protocol is able to successfully distill the single-photon component out of a weak coherent input state by

Table 4.2.: Second-order correlation function for various input shapes. This tables lists the values obtained for $g^{(2)}(0)$ with the different temporal input shapes given in Fig. 4.10 and with an average photon number in each of $\bar{n} = 0.11$.

Photon shape	$g^{(2)}(0)$
a: Gaussian	0.045 ± 0.006
b: Double peak	0.06 ± 0.03
c: Rectangular	0.06 ± 0.03
d: Capped Gaussian	0.07 ± 0.02

suppressing the even-parity states. The achieved fidelities for this input are limited by the cQED parameters, imperfect atomic state detection, and effective losses to the light state. This restricts the reported single-photon fidelity to $(66 \pm 1)\%$. However, the usage of the distillation protocol is not limited to coherent input states. To illustrate its capabilities on other states, it is interesting to simulate the result a distillation would have on the impure single photon that was produced in a similar system with an adiabatic transfer approach [173]. In this experiment, single-photon fidelities of $F_1 = 56\%$ have been reported. Performing the distillation including all the reported imperfections to this input state could increase this fidelity to $F_1 = 70.1\%$ with a probability of 45.2% for the heralding atomic detection.

The system used for the distillation could be improved with measures such as a better atomic state detection or an enhanced cavity stabilization. This could allow to approach the maximum achievable fidelity of the system $F_{1,\mathrm{max}}$ defined by the cQED parameters (see Eq. 4.11). While in our system these parameters limit the fidelity to 81.9%, different systems with an emitter strongly coupled to a resonator can, for instance, use higher reflectivities of the mirrors and smaller mode volumes to increase this maximal $F_{1\,\mathrm{max}}$. A good candidate system to produce high-fidelity single photons are state-of-the-art fiber resonators in which atom-cavity couplings of $g = 2\pi \times 240\,\mathrm{MHz}$ have been achieved for a single rubidium atom in a cavity of $39\,\mu\mathrm{m}$ length [98]. Assuming an out-coupling efficiency in the reflecting mirror of $1300\,\mathrm{ppm}$ and taking realistic parasitic mirror losses of $13.5\,\mathrm{ppm}$ as reported in [99], single-photon fidelities of up to $F_1 = 0.959$ are possible.

These perspectives together with the adaptability to different temporal pulse shapes make the distillation a valuable tool in e.g. quantum network applications. They require single photons for many protocols from state teleportation [71] to joint computing operations [94] and the ability to be used with different temporal profiles can help to tune a photon spectrally to the receiving network module.

As a last point, the parity measurement itself can be used for the purification of, for instance, the Fock-state distribution of optical cat states [153, 174] or specific photonic states created by photon-blockade mechanisms [175, 176]. It can even allow for error correction in optical codes that employ the photon-number parity as an error syndrome [177].

5. A Nonlocal Quantum Gate between Distant Qubits

The content of this chapter has been published in:

A quantum-logic gate between distant quantum-network modules.
S. Daiss, S. Langenfeld, S. Welte, E. Distante, P. Thomas, L. Hartung, O. Morin and G. Rempe.
Science **371**, 614 (2021).

5.1. Motivation

Since they were first envisioned by Richard Feynman [73], quantum computers have come to the verge of first applications. In 2019, the first advantage of a quantum computer over classical processors has been demonstrated by Google, using 53 superconducting qubits to sample the outputs of random quantum circuits [85]. At the same time, systems based on atoms as qubits have developed the experimental toolboxes for large quantum circuits in monolithic setups [81, 178], and they have even shown the first simulations, e.g. of lattice models based on hybrid classical-quantum algorithms [179]. However, as the number of qubits increases, it becomes increasingly hard to scale the system up further. Each individual qubit must be well isolated from the environment, must have means to control and measure its state precisely, and should be connected to at least some other qubits to allow for joint computations [87]. Furthermore, for an action on a certain qubit there should be no effect on the other information carriers in the system. Experimentally, the limited size of, for example, cryostats or vacuum chambers, the increasing cross-talk between the many qubits, and the complexity of the necessary connection and control infrastructure are severe challenges in the further scaling of quantum processors [88, 89]. To date, the largest monolithic quantum processors have only around 50 qubits. This limited number of implemented qubits becomes even more problematic by the fact that a main goal of today's devices is the incorporation of error correction, requiring several physical qubits for each single logical qubit [90].

A promising way to deal with these challenges is the incorporation of quantum network techniques to combine smaller quantum processors to a larger computing architecture [88, 91, 92]. In such a modular approach, separate devices of moderate sizes can be linked with quantum channels to form a larger quantum processor. A versatile choice to connect the different modules is given by optical photons, as they are fast and have no interaction with other electromagnetic radiation. Optical fiber networks allow to easily guide them, and

thus they can bridge typical inter-building distances with only very small loss, for example on a science campus. First elementary qubit networks between distant modules based on such optical fibers have already shown their capability to teleport quantum states [53] or to distribute entanglement [63, 64, 180–186]. These experiments have demonstrated how to link distant qubit modules to form a joint quantum system. Most notably, in 2012, Ritter et. al published a quantum network paper using the same two qubit modules QGate and Pistol that were introduced in Chapter 3. This paper demonstrated a state transfer between the two modules, local manipulations of a nonlocal state, and the creation of remote atom-atom entanglement between the separated qubits. However, to extend the capabilities of such an architecture to distributed quantum computing, it is necessary to be able to perform quantum-logic gates between the qubits in separated network modules. To this end, gate teleportation has been proposed [93]. It allows performing nonlocal gates between qubits by employing previously shared entanglement, classical communication and local operations [187]. This has first been demonstrated in photonic systems in the context of linear optical quantum computing [188, 189] followed by a realization with continuous-variable states of light [190]. Recently, the technique was also implemented with stationary qubits in monolithic experimental setups. First, it was demonstrated with superconducting qubits in a single cryostat, both in a programmable processor [191] and with a setup using dedicated communication qubits coupled to logical qubits [192], then it was realized with ions in a single Paul trap [193].

In this thesis, I describe the first realization of a nonlocal quantum gate between widely separated qubit modules that we published in [94]. It does not rely on the gate teleportation mechanism but instead employs a simple successive photon-reflection from the modules that was proposed simultaneously by two different groups [194, 195]. In our implementation, we connect our two atom-cavity modules with an optical fiber and reflect a single photon first from QGate and then from Pistol, followed by a heralding photon detection and a conditional feedback. This fast protocol has the additional advantage that no prior distribution of a typically fragile entangled state is necessary and that the distant qubits are thus always ready for a gate execution. We envision that this protocol is used in future implementations of a quantum computer based on spins coupled to optical resonators with modules located in nearby buildings, as depicted in Fig. 5.1.

5.2. Demonstrating a Universal Two-Qubit Gate

As outlined in Chapter 2.2.1, a CNOT gate changes the state of the target qubit if the control qubit is in a certain state. Since the conjunction of this gate together with rotations of each individual qubit allows for universal quantum computing, the demonstration of a CNOT gate between distant qubits in two setups is the most versatile way to merge the computing power of the two modules.

This universal gate is implemented in the work presented here using the basis states $|\uparrow_z\rangle / |\downarrow_z\rangle$ and $|\uparrow_x\rangle = (|\uparrow_z\rangle + |\downarrow_z\rangle)\sqrt{2} / |\downarrow_x\rangle = (|\uparrow_z\rangle - |\downarrow_z\rangle)\sqrt{2}$. With the first value in each
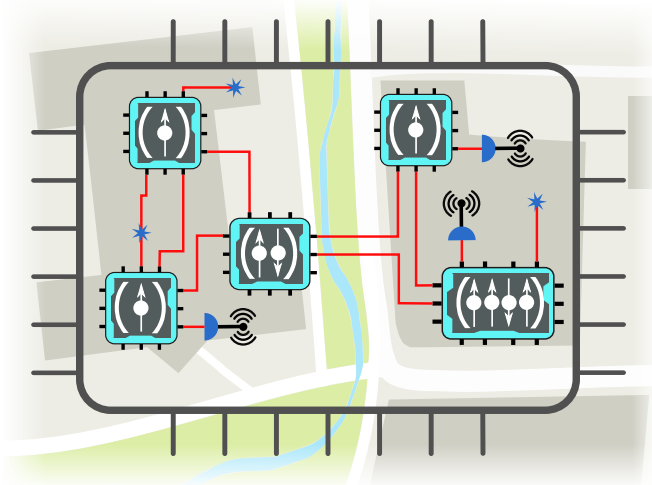
Figure 5.1.: Vision of a distributed computing system. Qubit modules are formed by spins (white arrows) in a resonator (white brackets). Many different such modules form together a larger computing cluster between different buildings. They are connected by optical fibers (red lines) to each other and to both photon sources (blue stars) and photon detectors (blue half-discs). Detection results can be communicated classically (indicated by the black antennas).

ket state belonging to QGate and the second to Pistol, the effect of the gate can be expressed as

$$
\begin{aligned}
|\uparrow_z \uparrow_x\rangle &\longrightarrow |\uparrow_z \uparrow_x\rangle \\
|\uparrow_z \downarrow_x\rangle &\longrightarrow |\uparrow_z \downarrow_x\rangle \\
|\downarrow_z \uparrow_x\rangle &\longrightarrow |\downarrow_z \downarrow_x\rangle \\
|\downarrow_z \downarrow_x\rangle &\longrightarrow |\downarrow_z \uparrow_x\rangle .
\end{aligned}
\tag{5.1}
$$

To characterize the gate realized between the two distant qubits, it is necessary to validate that the presented operation does indeed approximate a CNOT gate (limited by existing experimental imperfections). An important step of this consists in measuring the truth table of the gate operation. It gives the distribution of the output in the basis $|\uparrow_z \uparrow_x\rangle, |\uparrow_z \downarrow_x\rangle, |\downarrow_z \uparrow_x\rangle, |\downarrow_z \downarrow_x\rangle$ for the different initial states in Eq. 5.1. For an ideal CNOT, the gate unitary describing this is defined by the matrix

$$
\hat{U}_{\text{CNOT}} = \begin{pmatrix} 1 & 0 & 0 & 0 \\ 0 & 1 & 0 & 0 \\ 0 & 0 & 0 & 1 \\ 0 & 0 & 1 & 0 \end{pmatrix}
\tag{5.2}
$$

and the truth table measurement detects the corresponding output probabilities for all four input-basis states. However, this does not determine the phases in the entries of Eq.

5.2 that might still be non-zero in the experimental realization. Indeed, the same detection probabilities in the measured states can be achieved with any unitary represented by

$$\hat{U}_{\delta,\theta,\zeta} = \begin{pmatrix} 1 & 0 & 0 & 0 \\ 0 & \exp i\delta & 0 & 0 \\ 0 & 0 & 0 & \exp i\theta \\ 0 & 0 & \exp i\zeta & 0 \end{pmatrix} \tag{5.3}$$

with some phases δ, θ, ζ. Any additional complex phase of the first column can be absorbed in a global phase and is therefore assumed to be zero without loss of generality. Thus, to quantify the unitary operation of a gate as a CNOT, more measurements are needed to determine the values of the possible phases.

An approach that is often taken to claim a CNOT gate consists of measuring the truth table and additionally creating one maximally-entangled Bell state. This method has been used in different gate implementations over a variety of systems [81, 113, 196, 197]. However, it does not simultaneously attribute values to all possible phases in Eq. 5.3. It is more targeted at demonstrating a truth table and showing both the linearity of the gate operation and the ability to create entanglement by producing Bell states.

For a more thorough approach, the values of the other phases should be determined in the analysis of the gate operation. This can be done in different ways. A full process tomography can completely describe the effect of the considered operation for any input state [109]. For this procedure, the resulting state has to be obtained for 16 different input states. However, the full procedure is not necessary if a unitary operation is assumed as in the case of Eq. 5.3. One approach in this simpler scenario is to measure the truth table for different sets of basis states and complement this measurement with one Bell-state generation as done in [135]. A different route is taken here. It combines three different measurements to address the three different possible phases in Eq. 5.3. The outline of this approach is given below, and it also demonstrates why the generation of just one Bell state is not sufficient.

First, the unitary $\hat{U}_{\delta,\theta,\zeta}$ is applied to the state $|\uparrow_x\uparrow_x\rangle$. This results in an entangled state as

$$|\uparrow_x\uparrow_x\rangle = \frac{1}{\sqrt{2}}\left(|\uparrow_z\uparrow_x\rangle + |\downarrow_z\uparrow_x\rangle\right) \xrightarrow{\hat{U}_{\delta,\theta,\zeta}} \frac{1}{\sqrt{2}}\left(|\uparrow_z\uparrow_x\rangle + \exp i\zeta |\downarrow_z\downarrow_x\rangle\right). \tag{5.4}$$

The resulting state yields information about the phase ζ. If it is the Bell state $|\Phi^+\rangle = \left(|\uparrow_z\uparrow_x\rangle + |\downarrow_z\downarrow_x\rangle\right)/\sqrt{2}$, as would be expected for a CNOT gate, it can be concluded that $\zeta = 0$.

The generation of another entangled state is used to determine the second phase. Applying the unitary $\hat{U}_{\delta,\theta,\zeta}$ to the initial state $|\uparrow_x\downarrow_x\rangle$ results in

$$|\uparrow_x\downarrow_x\rangle = \frac{1}{\sqrt{2}}\left(|\uparrow_z\downarrow_x\rangle + |\downarrow_z\downarrow_x\rangle\right) \xrightarrow{\hat{U}_{\delta,\theta,\zeta}} \frac{1}{\sqrt{2}}\left(\exp i\delta |\uparrow_z\downarrow_x\rangle + \exp i\theta |\downarrow_z\uparrow_x\rangle\right). \tag{5.5}$$

If the resulting state after the experiment is the Bell state $|\Psi^+\rangle = \left(|\uparrow_z\downarrow_x\rangle + |\downarrow_z\uparrow_x\rangle\right)/\sqrt{2}$, as would be expected for a CNOT gate, it can be concluded that $\delta = \theta$. Creating the

two maximally-entangled states mentioned here leaves therefore only the phase δ in Eq. 5.3 undefined. It is noteworthy that the unitary $\hat{U}_{\delta,\theta=\delta,\zeta=0}$ already corresponds to a universal gate, as it can be combined with a single-qubit gate on the Pistol side with $|\downarrow_x\rangle \to \exp(-i\delta)|\downarrow_x\rangle$ to form a CNOT.

This last phase can still be determined, for example, by applying $\hat{U}_{\delta,\theta,\zeta}$ to an initial state $|\uparrow_z\uparrow_z\rangle$. This yields

$$|\uparrow_z\uparrow_z\rangle = \frac{1}{\sqrt{2}}\left(|\uparrow_z\uparrow_x\rangle + |\uparrow_z\downarrow_x\rangle\right) \xrightarrow{\hat{U}_{\delta,\theta,\zeta}} \frac{1}{\sqrt{2}}\left(|\uparrow_z\uparrow_x\rangle + \exp i\delta \,|\uparrow_z\downarrow_x\rangle\right). \tag{5.6}$$

If the resulting state after the gate operation is $\left(|\uparrow_z\uparrow_x\rangle + |\uparrow_z\downarrow_x\rangle\right)/\sqrt{2} = |\uparrow_z\uparrow_z\rangle$, i.e. if the input state is an eigenstate of the operation and remains unchanged, it can be concluded that $\delta = 0$. These three measurements together can confirm that an operation producing the correct truth table is, in fact, a CNOT gate.

5.3. Protocol of the Nonlocal Quantum Gate

Here I describe the protocol of the nonlocal gate by formulating the effect of each single step on an initial atomic state

$$|\Psi\rangle = \alpha_1 |\uparrow_z\uparrow_z\rangle + \alpha_2 |\uparrow_z\downarrow_z\rangle + \alpha_3 |\downarrow_z\uparrow_z\rangle + \alpha_4 |\downarrow_z\downarrow_z\rangle. \tag{5.7}$$

As above, the first spin of each ket describes the qubit state in the QGate system, from which the photon is reflected first. The second spin indicates the qubit state in Pistol. The coefficients α_1, α_2, α_3, α_4 follow the normalization constraint

$$\sqrt{|\alpha_1|^2 + |\alpha_2|^2 + |\alpha_3|^2 + |\alpha_4|^2} = 1. \tag{5.8}$$

Hereafter, this discussion uses the approximation $r_\uparrow = -r_\downarrow = 1$ (see Chapter 2.2.3).

First, an initial right-circularly polarized photon in $|R\rangle$ is converted to $|A\rangle$ using a quarter-wave plate. The light is then reflected from the QGate resonator. Using Eq. 2.28 and 2.29 from Chapter 2.2.3, this reflection results in the combined atom-atom-photon state

$$|\Psi\rangle = i\alpha_1 |\uparrow_z\uparrow_z\rangle |D\rangle + i\alpha_2 |\uparrow_z\downarrow_z\rangle |D\rangle - \alpha_3 |\downarrow_z\uparrow_z\rangle |A\rangle - \alpha_4 |\downarrow_z\downarrow_z\rangle |A\rangle. \tag{5.9}$$

On the way to the Pistol setup, the light passes through another quarter-wave plate that transforms the light's polarization according to $|A\rangle \to |R\rangle$ and $|D\rangle \to |L\rangle$. Afterwards, the light is reflected from the Pistol cavity, resulting in a π change of the phase for all terms not having both the Pistol atom in $|\uparrow_z\rangle$ and the photon in $|R\rangle$. The total state is then given by

$$|\Psi\rangle = -i\alpha_1 |\uparrow_z\uparrow_z\rangle |L\rangle - i\alpha_2 |\uparrow_z\downarrow_z\rangle |L\rangle - \alpha_3 |\downarrow_z\uparrow_z\rangle |R\rangle + \alpha_4 |\downarrow_z\downarrow_z\rangle |R\rangle. \tag{5.10}$$

In a next step, the light is detected in the basis of $|A\rangle / |D\rangle$. Rewriting the polarizations as $|R\rangle = (|D\rangle - i\,|A\rangle)/\sqrt{2}$, $\quad |L\rangle = (|A\rangle - i\,|D\rangle)/\sqrt{2}$, we arrive at

$$\begin{aligned}|\Psi\rangle = &-\frac{1}{\sqrt{2}}\left(\alpha_1 |\uparrow_z\uparrow_z\rangle + \alpha_2 |\uparrow_z\downarrow_z\rangle + \alpha_3 |\downarrow_z\uparrow_z\rangle - \alpha_4 |\downarrow_z\downarrow_z\rangle\right)|D\rangle \\ &-\frac{i}{\sqrt{2}}\left(\alpha_1 |\uparrow_z\uparrow_z\rangle + \alpha_2 |\uparrow_z\downarrow_z\rangle - \alpha_3 |\downarrow_z\uparrow_z\rangle + \alpha_4 |\downarrow_z\downarrow_z\rangle\right)|A\rangle.\end{aligned} \tag{5.11}$$
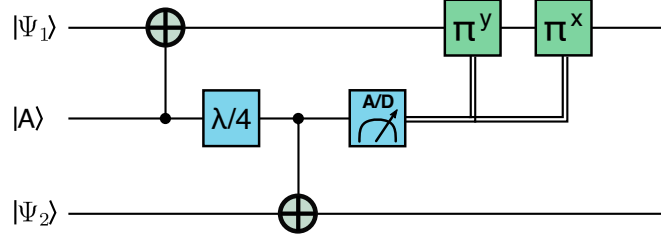
Figure 5.2.: Quantum circuit diagram of the nonlocal gate protocol. $|\Psi_1\rangle$ and $|\Psi_2\rangle$ are the states of the qubits residing in the two distant atom-cavity systems. The middle line gives the state of the ancilla photon that is initially in $|A\rangle$. The reflection of the photon on the qubit modules is depicted as a CNOT gate between the two relevant qubits. The classical communication of the polarization measurement in depicted as double line that is connected to the conditional feedback π pulses.

For limited transmission probabilities, the detection of the photon heralds a successful gate application. The result of this detection is then communicated to the QGate experiment. This allows for a polarization dependent feedback to ensure the resulting atom-atom state is the same for both measured polarizations: If the photon detection occurs in $|A\rangle$, an effective Z-gate feedback is applied to the qubit in QGate.

As described in Chapter 3.4.3, this could be done by introducing a detuning Δ_{R} for a time $1/(2\Delta_{\mathrm{R}})$ between the Raman beams at the QGate setup. This would change the reference system of the qubit given by the Raman beams. However, as there is no control pulse acting on the joint qubit state directly, a different approach was chosen to implement the feedback physically onto the qubit in QGate. In the realization presented in this work, the Z gate is performed by first a π-pulse T_π^y around the y-axis and then a π-pulse T_π^x around the x-axis (see Appendix A). For the photon detected in $|A\rangle$, this implements the following transformation on the QGate atom:

$$T_\pi^x T_\pi^y |\uparrow_z\rangle = -i\,|\uparrow_z\rangle\,, \quad \text{and} \quad T_\pi^x T_\pi^y |\downarrow_z\rangle = i\,|\downarrow_i\rangle\,. \tag{5.12}$$

If the photon is detected in the state $|D\rangle$, no feedback is applied. In total and up to a global phase, this yields the state

$$|\Psi\rangle = (\alpha_1 |\uparrow_z\uparrow_z\rangle + \alpha_2 |\uparrow_z\downarrow_z\rangle + \alpha_3 |\downarrow_z\uparrow_z\rangle - \alpha_4 |\downarrow_z\downarrow_z\rangle) \tag{5.13}$$

independent of the measured polarization of the photon. The total protocol thus realizes a fully controlled quantum-PHASE gate with

$$\begin{aligned}
|\uparrow_z\uparrow_z\rangle &\longrightarrow |\uparrow_z\uparrow_z\rangle \\
|\uparrow_z\downarrow_z\rangle &\longrightarrow |\uparrow_z\downarrow_z\rangle \\
|\downarrow_z\uparrow_z\rangle &\longrightarrow |\downarrow_z\uparrow_z\rangle \\
|\downarrow_z\downarrow_z\rangle &\longrightarrow -\,|\downarrow_z\downarrow_z\rangle
\end{aligned} \tag{5.14}$$

From this, a quantum CNOT gate can be obtained, either in the z-basis by combing the phase gate with two Hadamard gates [114] or by working with one atom in a superposition
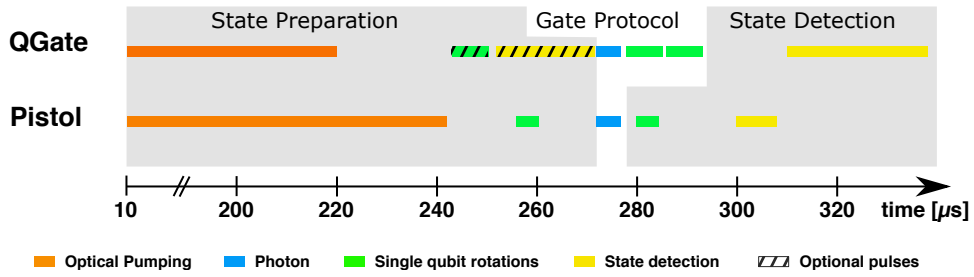
Figure 5.3.: Protocol of the truth table measurement. The experimental sequences that are run in the QGate and Pistol labs to measure the truth table of the nonlocal gate. A hatched color indicates that the corresponding pulse is only performed for some of the prepared states.

basis $|\uparrow_x\rangle = \frac{1}{\sqrt{2}}\left(|\uparrow_z\rangle + |\downarrow_z\rangle\right)$ and $|\downarrow_x\rangle = \frac{1}{\sqrt{2}}\left(|\uparrow_z\rangle - |\downarrow_z\rangle\right)$, which directly results in the gate having the effect

$$
\begin{aligned}
|\uparrow_z\uparrow_x\rangle &\longrightarrow |\uparrow_z\uparrow_x\rangle \\
|\uparrow_z\downarrow_x\rangle &\longrightarrow |\uparrow_z\downarrow_x\rangle \\
|\downarrow_z\uparrow_x\rangle &\longrightarrow |\downarrow_z\downarrow_x\rangle \\
|\downarrow_z\downarrow_x\rangle &\longrightarrow |\downarrow_z\uparrow_x\rangle \, .
\end{aligned}
\tag{5.15}
$$

The quantum circuit diagram of the basic operations necessary for the nonlocal quantum gate is shown in Fig. 5.2. It contains both the separated atomic qubits and the ancilla photon and gives the necessary rotations, feedback, and local atom-photon gates. To demonstrate that this protocol does indeed realize a quantum CNOT gate, it is necessary to show a truth table measurement of Eq. 5.15, as was outlined in the section above. Additional measurements define then the possible phases in the underlying unitary.

5.3.1. Timing of the Protocol

When doing the experiments, we run the gate protocol at a repetition rate of 1 kHz. Most of the time is needed for the cooling of the atoms after each gate attempt and for the initial pumping of the atoms. The sequence of the remaining part of the protocols for the truth table and the entanglement generation are visualized in Fig. 5.3 and Fig. 5.4, respectively. They differ slightly in state preparation and detection, but the gate consisting of the photon reflection and the feedback is the same.

In the following, the differences and similarities of the two measurement protocols are outlined by referring to the colored sequences shown in Fig. 5.3 and Fig. 5.4. For the truth table measurement, the QGate qubit is prepared either in $|\uparrow_z\rangle$ by optical pumping (orange sequence) or in $|\downarrow_z\rangle$ with an additional π-pulse (green) followed by a heralding state detection (yellow). The heralding serves to increase the production fidelity: If for incident state-detection light there are no photons scattered to the cavity, the atom is in $|\downarrow_z\rangle$. These additional pulses for a preparation in $|\downarrow_z\rangle$ are marked as optional in Fig. 5.3. For the entanglement generation experiment, QGate prepares an equal superposition of $|\uparrow_z\rangle$ and $|\downarrow_z\rangle$ by employing a $\pi/2$ rotation pulse after the optical pumping. The same
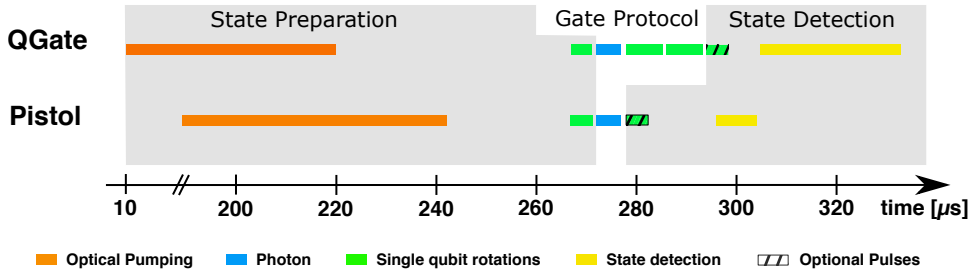
Figure 5.4.: Protocol of the Bell-state generation. The experimental sequences that are run in the QGate and Pistol labs to generate the Bell-states with the nonlocal gate. A hatched color indicates that the corresponding pulse is only performed for some of the prepared states or detection bases.

is done in the Pistol module for both protocols before the gate sequence follows. For this, the photon is first reflected from the two systems and then it is measured with the polarization resolving detector (blue colored sequence). The feedback to the QGate qubit is performed, depending on the measured polarization, with two successive π pulses (green sequences in the gate part). While the atomic states are normally measured in the basis of $|\uparrow_z\rangle / |\downarrow_z\rangle$, the detection basis can also be rotated with additional (optional) Raman pulses around either the x-axis ($\frac{1}{\sqrt{2}} (|\uparrow_z\rangle + |\downarrow_z\rangle)$) or the y-axis ($\frac{1}{\sqrt{2}} (|\uparrow_z\rangle + i |\downarrow_z\rangle)$). This enables measurements along different qubit axes. In the Bell-state generation experiment, these pulses are switched randomly to perform a state detection in all combinations of bases for the two atoms to reconstruct the complete state [198]. In the measurements, the time needed for a $\pi/2$-pulse was roughly $4\,\mu s$. State detections are not done simultaneously in the two setups to prevent state-detection light from the QGate side to leak to the Pistol detectors. First, the state detection is done on the Pistol side during $8\,\mu s$, followed by the measurement on the QGate side. For the latter, we use a measurement time of $30\,\mu s$, but we switch off the detection laser-light automatically if there are more than three photons detected. This threshold allows to discriminate the atomic states by their emission while the resulting spectrum retains enough features to ensure a sufficient discrimination between the two corresponding distributions.

After the final state detection, a stabilization of the cavity frequency is performed in the QGate lab within $110\,\mu s$ [125] before the cooling light is switched on for roughly $500\,\mu s$. In the Pistol lab, the atoms are cooled directly after the sequence given here.

5.4. Experimental Implementation

The setup of the nonlocal gate protocol connects the two individual atom-cavity systems introduced in Chapter 3 to form an elementary quantum network consisting of two modules [61]. The resonators are linked with a 60-meter-long optical fiber as a quantum channel, as described below. Additional coaxial cables are used for classical communication, for example between the detection setup and the first module. The experimental setup is sketched in Fig 5.5.

5.4.1. The Quantum-Network Link

The experimental setups for the two network modules used in this work are located in laboratories that are 21 m apart. A versatile way to connect different network modules is given by the use of optical fibers. Here a 60 m Thorlabs 780HP optical single-mode fiber is employed to send light from QGate to Pistol. The end facets of the fiber have an anti-reflection coating each. For the experiments described below, polarization qubits at 780 nm are sent between the two modules. At this wavelength the fiber has a transmission of 95 % over the distance of 60 m.

At each module, it is important to be able to route the outcoming light of the resonator to a channel different from the input. For this purpose, it is necessary to include circulators before each cavity as shown in Fig 5.5. In case of the QGate side, this is done by employing a Semrock LL780 filter with a transmission of 98.5 % at 780 nm as a non-polarizing beam splitter. As we use weak coherent light as an input, the low reflectivity of the filter is employed to weaken the incident light to the low average photon number utilized. The light reflected from the resonator is transmitted through the filter and is thus only subject to little loss. Afterwards, it passes several optics and an AOM in zeroth order (see Fig 5.5) before being injected into the long fiber.

At the Pistol side, there is a fiber circulator (PMOPTICS Inc. 780nm SM2) directly spliced to the connecting fiber with one port going to the cavity. A transmission of 0.81 has been measured, and it has an isolation to other outputs of at least 36 dB, depending on the port. After a reflection from the Pistol module, the light enters again the circulator and is routed to the last output port, leading to a polarization resolving detection setup based on superconducting nanowire single-photon detectors. In the context of larger quantum networks, such a circulator port could be connected to additional quantum modules [107].

We use piezoelectric fiber squeezers to actively stabilize the polarization between the modules. The details of the applied procedure and the required setup for this are described in Chapter 5.4.3.

5.4.2. Synchronization

In the past years, both the QGate and the Pistol setups have been upgraded independently. For the experiments performed here, it is necessary to synchronize the individual experimental sequences and run them only once both systems have successfully loaded an atom into their cavity. Furthermore, the data taken at the different single-photon detector setups has to be matched to each other.

At the beginning of an experimental run, QGate and Pistol attempt independently to load an atom each. If a system loads an atom successfully, this is heralded using a TTL signal and the atom-cooling sequence [117] is started in the corresponding setup. Once both systems have sent the loading TTL signal, the main experimental protocol is started. The necessary sequences for each system are run individually by an FPGA in each laboratory. In order to synchronize them, the QGate FPGA acts as the main control and sends a
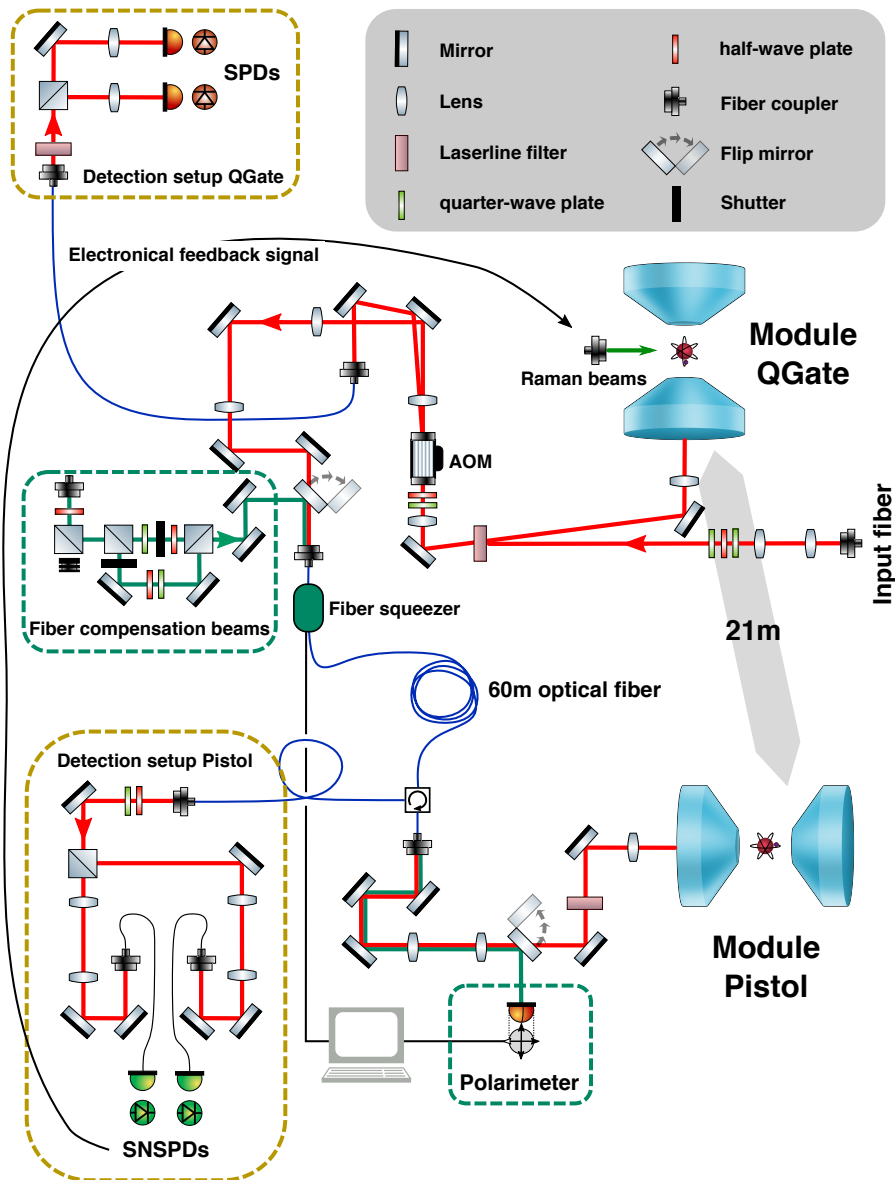
Figure 5.5.: Connection of two qubit modules. This sketch shows the beam path connecting the two qubit modules QGate and Pistol, including all optical components. The connecting light (red line) from an input fiber travels via a laserline filter as a circulator to the QGate cavity. Reflected light can either be sent by an AOM and an optical fiber to the QGate detection setup (top left) or via a 60 m optical fiber to the Pistol module. Using a fiber circulator there, it is first reflected from the cavity before going through the fiber to the Pistol detection setup (bottom left). Depending on the measurement outcome, a feedback is applied to the QGate atom. The waveplates and lenses in the beam paths are used to set the mode and polarization of the light. To control possible polarization drifts in the long fiber, reference light of two different and known polarizations (dark green line) can be coupled into the long fiber using flip mirrors. The polarization of either is measured at the Pistol side and corrected to the target value using piezoelectric fiber squeezers and computer-based optimization.

trigger to start each single experimental run at Pistol exactly at the onset of each QGate sequence.

To attribute the data sets taken at the different locations to each other, the QGate FPGA sends a digitally encoded experimental-run number at the beginning of every sequence to each of the time-tagging quTAU boxes in the laboratories. This allows to match the click data of each time tagger to the other one, even though the absolute time stamp at each device is subject to accumulating relative differences and overflow resets. This digitally encoded experimental-run number is sent three times to allow for a majority-vote error correction in case of non-registered clicks at the time taggers. The click data of each quTAU box is then pre-processed and the relevant information stored in binary file format (hdf5) for a following joint evaluation in Python.

5.4.3. Matching the Polarizations

In the nonlocal gate protocol, the light sent between the two systems contains an ancilla qubit encoded in the polarization. Thus, it is crucial to match the polarization bases at the different locations of the setup; for example, a photon that interacts with QGate in a $|R\rangle$ polarization, should have – neglecting any further quarter-wave plate effect or change due to the QGate resonator – the same polarization when it interacts with Pistol and this polarization should also match $|R\rangle$ in the polarization resolving detection setup. Since the light passes through a long optical fiber, this equates to controlling the birefringence in the fiber. However, it passes through several rooms and is subject to the relative and absolute temperature drifts between them. As the refractive axes depend on the stress on the fiber, these drifts lead to a time dependent birefringence that needs to be controlled (see [199] for measurements of the drift). For this purpose, we employ four piezoelectric fiber squeezers (General Photonics, PCD-M02) to locally apply stress to change the birefringence. The squeezers are mounted at different angles around the fiber to allow for an arbitrary polarization change. This system is used to actively stabilize the birefringence to the desired value, similar to a setup that has been implemented in the Weinfurter group [200, 201].

For the stabilization, we use light in two reference polarizations that can each be blocked using electronic shutters. This light can be injected into the long fiber using a flip mirror at the QGate side (see Fig. 5.5). At Pistol, there is another flip mirror to send the reference light to a polarimeter. To set the reference polarizations, a resonant beam polarized either in $|R\rangle$ or in $|A\rangle$ is sent to the locked QGate cavity without an atom loaded. The light is reflected and passes several optical elements and an AOM, all of which affect the resulting polarization arriving just before the long fiber. Then the reference beams of the fiber calibration are matched to these final polarizations. The detailed procedure for this is described in the next section below. This matching allows to use the automatic fiber calibration with input polarizations that correspond exactly to $|R\rangle$ and $|A\rangle$ at the QGate cavity. As the target polarizations of the automatic calibration at the Pistol module, the respective circular and eigenaxis polarizations of the Pistol resonator are used. With a gradient-descent method, the overlap of measured and target polarization are then maximized using the fiber squeezers [199]. This can be utilized to force $|R\rangle$ at QGate to correspond to $|R\rangle$ at Pistol and to stabilize it against drifts in the birefringence. The

Table 5.1.: Polarization-detection click ratios. Typical ratios of the number of clicks in the different channels of the polarization-detection setup for various input polarizations. The fiber squeezers implement a quarter-wave plate that rotates the polarization prior to the measurement. Polarization-dependent losses, imperfect wave-plate operations and the accuracy of the stabilization and characterization lead to deviations from the ideally expected values.

Detection bases	Preparation bases			
	$|R\rangle$	$|L\rangle$	$|A\rangle$	$|D\rangle$
$|R\rangle\,/\,|L\rangle$	0.50	0.43	0.993	0.031
$|A\rangle\,/\,|D\rangle$	0.994	0.043	0.47	0.53

full protocol of the nonlocal gate includes an additional quarter waveplate, which is also realized using the fiber squeezers on the long fiber. For this, the target polarizations of the compensation algorithm are changed, as an initial $|R\rangle$ should correspond to $|A\rangle$ after the fiber.

The full compensation takes several 10 s and has been performed every 60 min to 90 min during the following experiments to make up for the effect of slow temperature drifts that occur on timescales on the order of hours.

As a last step of the polarization matching, it has to be ensured that also the detection setup measures $|R\rangle$ and $|A\rangle$ as defined at the cavities. To achieve this, light in $|R\rangle$ and $|A\rangle$ is reflected on the Pistol side from a locked and empty resonator. It is used to tweak the polarization detection setup by equalizing the counts in $|A\rangle\,/\,|D\rangle$ or by maximizing the counts in $|A\rangle$, respectively.

To check the final polarization matching, light having the polarizations $|R\rangle$, $|L\rangle$, $|A\rangle$ and $|D\rangle$ is sent via QGate and Pistol and the click ratios in the different channels of the polarization detection setup are checked. A typical result of these ratios after an automated calibration of the fiber is listed in Table 5.1. The deviations from the ideally expected values are attributed to polarization-dependent losses and to imperfect waveplate effects, limited by the accuracy of the polarimeter and the compensation, resulting in a small overall depolarization of the light.

5.4.4. Temperature Effects of the Path-Switch AOM

A crucial element in the beam path is the AOM that is used to send light to the SPDs on the QGate side (see Fig. 5.5 for a sketch of the setup). With the RF power applied, it steers light into the first-order diffraction mode going to the detection setup. This is the standard setting during the protocol, as it also limits light leakage to the Pistol setup. Only for the transmission of the single photon mediating the quantum gate, this RF power is switched off to allow for maximal transmission (97.5 %).

In the procedure to map the reference beams to the polarization of the light reflected from the QGate cavity for a certain AOM duty cycle, light is reflected from the QGate resonator
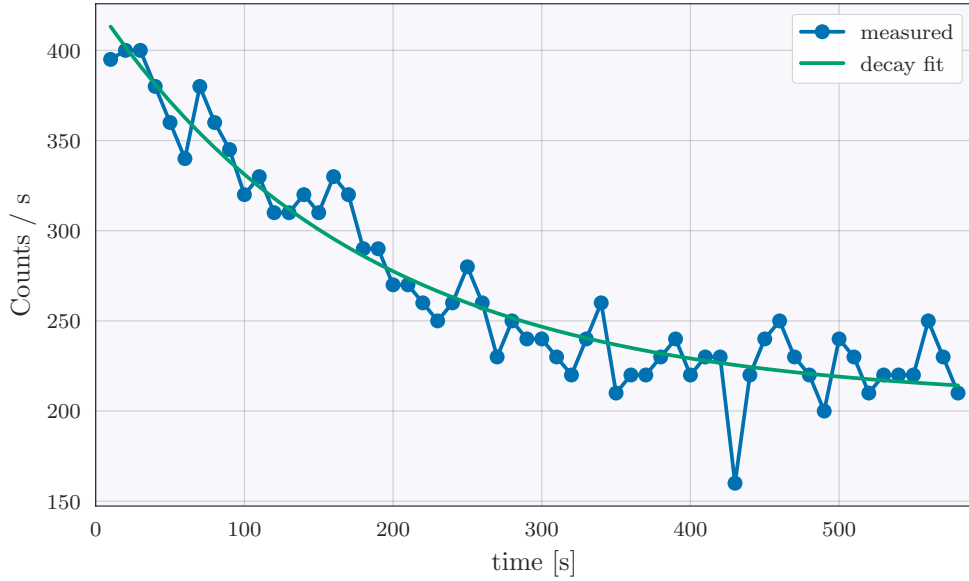
Figure 5.6.: Effect of the path-switch duty cycle. This figure shows the measured photons in the Pistol setup starting when the AOM was switched to a 99 % duty cycle after a short time of being constantly on. The counts/s values given are averages over 10 consecutive seconds. Before the brief period of being constantly on, the transmission had been reduced to ≈ 70 counts using a quarter-wave plate and a polarizer in a 99 % duty-cycle protocol. The slow decay of the counts is attributed to temperature effects that occur already at the small differences in the duty cycles compared here. A fit of an exponential decay to the data is shown in green.

when the AOM is off. Using a combination of a quarter-wave plate and a polarizer in front of the long fiber, the number of clicks detected in the SPDs on the Pistol side is minimized by rotating the elements by hand. Leaving the waveplate and the polarizer in place, the polarizations of the reference beams can be adapted to reduce the counts through the long fiber, and they are thus matched to the polarization of the QGate reflected light. In this procedure, we noticed that the total number of counted photons on the Pistol side for a given polarizer and waveplate setting depends on the duty cycle of the AOM. After for a short time running a protocol that has a 100 % duty cycle (no light sent to the Pistol setup) and a following switching back to the minimization scheme with a 99 % duty cycle (protocol of 1 ms duration), we registered a five-fold increase in the count numbers of the SPDs from the initial ≈ 70 counts (corresponding to a ≈ 7° rotation on the Poincaré sphere for a maximum number of 10^5 detected photons). While this improved during the first 10 min of running with the 99 % duty cycle, it did not recover the original counts, as shown in Fig. 5.6. Instead, the data shows an exponential decay that is fitted with a decay time of 180 s and a limit of 206 counts/s. The fit is displayed in the figure in green. The observed decaying behavior is attributed to the slight change in AOM temperature related to a modification in the duty cycle and to the corresponding impact on the polarization. The AOM contains a crystal as the medium of the sound waves that reflect the incident light via Bragg diffraction. Small changes in temperature can affect the birefringence of this crystal and therefore the polarization of the light transmitted through it. In this effect,

also some hysteresis is observed, and it is thus important to avoid any change in the duty cycle during all the relevant operations and calibration measurements. To this end, all the protocols including e.g. the cooling sequence during loading and the heating sequence when too many atoms are loaded were rewritten. All further measurements between the two setups are performed with the AOM being switched on every $1\,\mathrm{ms}$ for a duration of $8\,\mathrm{\mu s}$.

5.5. Experimental Results

Here I give the main results of our realization of a nonlocal quantum gate protocol, starting with a discussion of the light mediating the interaction. Then the measurement of the truth table is presented. To demonstrate the coherent nature of the gate, the results of the creation of all four maximally-entangled Bell states with this gate protocol are given. Lastly, it is discussed that this operation does indeed realize a quantum controlled-NOT gate.

5.5.1. Weak Coherent Pulses and Success Probability of the Gate

The theoretically discussed ideal protocol from above is subject to several imperfections for our implementation in the laboratories. A primary example is the use of weak coherent pulses that, together with postselection, approximate the single-photon for our purpose. A coherent pulse has a Poissonian photon distribution [154] and therefore it always has contributions of higher Fock states. Due to existing losses in the setup and the detection of the light, such contributions can still be detected as a single photon even though it interacted with either one or both cavities as a higher photon-number state before. The ratio of single to higher photon-number contributions can be improved by decreasing the average photon number $\overline{n}$ of the pulse to $\overline{n} \ll 1$. Such a pulse, however, consists predominantly of vacuum, which greatly lowers the efficiency of our protocol, as there are few heralding clicks. This increases both the impact of dark counts and the overall measurement time and therefore leads to a higher sensitivity to drifts of the experimental parameters.

The impact of the average photon number on QIP protocols in our setup of an elementary quantum network is illustrated by the characterization measurement shown in Fig. 5.7. It is based on the protocol of the single-photon distillation that was introduced in Chapter 4.2: A weak coherent pulse with an average photon number of $\bar{n}$ that is polarized in $|R\rangle$ is sent to the QGate setup with the atom in the superposition state $(|\uparrow_z\rangle + |\downarrow_z\rangle)/\sqrt{2}$. The reflected light travels through the long fiber, is reflected at the Pistol resonator and detected by the SNSPDs. In this scenario, the Pistol cavity is locked without an atom trapped at its center. Ideally, the reflection of a single photon at the QGate cavity changes the atomic state to $(|\uparrow_z\rangle - |\downarrow_z\rangle)/\sqrt{2}$ and a final $\pi/2$ results in the atom in $|\uparrow_z\rangle$. For the distillation, the atom state was measured and the resulting light state analyzed. Here, the atomic state conditioned on a heralding detection of the light (a click in the SPDs) is of interest, as it gives a fidelity to whether a single photon has interacted with the cavity [112]. This technique is used to characterize the influence of the average photon number by measuring
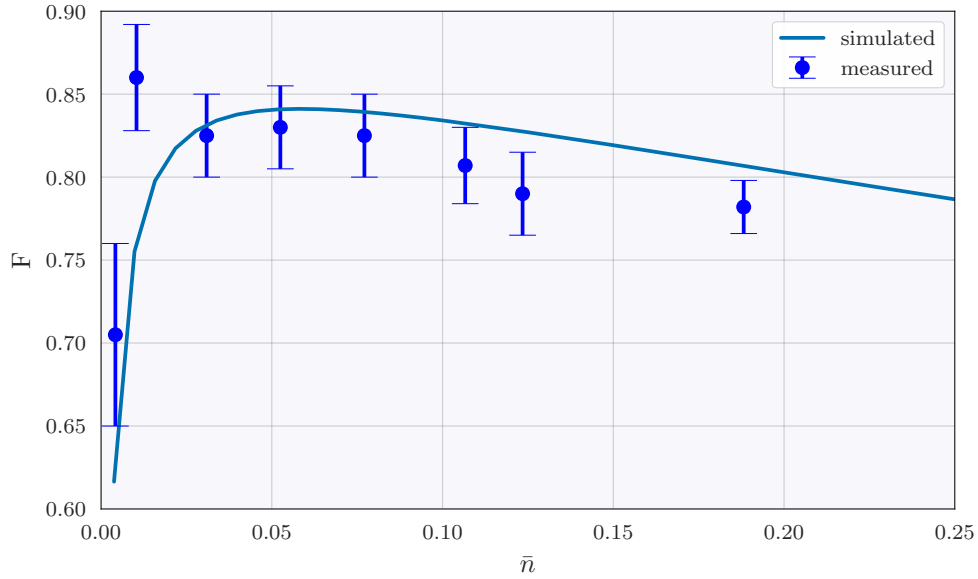
Figure 5.7.: nondestructive (ND) photon-detection protocol over n̄. This figure shows a characterization measurement for the impact of the average photon number $\bar{n}$. The fidelity of the atom being in $|\uparrow\rangle$ for a click detection in the SNSPDs is strongly affected by contributions from higher photon numbers in the initial pulse [112], leading to a drop of the fidelity F for higher $\bar{n}$. For very low average photon numbers, random dark counts in the detectors start to dominate, resulting in a lower fidelity. The solid line gives a curve of the expected fidelity using the experimental specifications listed in Chapter 5.6.1, with a separately measured dark-count rate of $23\,\mathrm{Hz}$ per detector, a Monte-Carlo sampling of the cavity width using 50 samples, and no free parameters.

the overlap fidelity F of the final atomic state with $|\uparrow_z\rangle$: As a result of the higher Fock-state contributions, the fidelity drops with larger $\bar{n}$. For small $\bar{n}$, the scarce rate of detection events leads to a higher impact of the dark-count rate, which again lowers the fidelity. Fig. 5.7 also shows the fidelity expected from a simulation of the experiment including these effects and other known imperfections of the setup (summarized in Chapter 5.6.1, albeit here the cavity width is sampled only with 50 values and a separately measured dark-count rate of $23\,\mathrm{Hz}$ is used for the detectors). For the further experiments presented here, weak coherent light with an average photon number of $\bar{n} = 0.07 \pm 0.01$ is used as a trade-off between good fidelities and acceptable measurement times.

The two cavities have a non-unity reflectivity. For the estimated mode matching, the average reflectivities of the two systems are $60\,\%$ for QGate and $55\,\%$ for Pistol. Between the two setups, there are various optical elements (see Fig. 5.5), a zeroth-order AOM transmission, a Semrock laserline filter and the long fiber with an included circulator. The total transmission of light from just after the QGate cavity to just before the Pistol resonator is $52\,\%$. After Pistol, the light enters again into a fiber, passes the circulator, and is detected using a polarization-detection setup consisting of two SNSPDs. The detection efficiency of a single photon from just after the Pistol cavity with this system is $50\,\%$.

Due to all these effects, the total success probability P to detect a heralding photon for

Table 5.2.: Measurement of the truth table. Registered detection events in the different states for a certain input to the gate operation.

input / output	$\lvert\uparrow_z\uparrow_x\rangle$	$\lvert\uparrow_z\downarrow_x\rangle$	$\lvert\downarrow_z\uparrow_x\rangle$	$\lvert\downarrow_z\downarrow_x\rangle$
$\lvert\uparrow_z\uparrow_x\rangle$	491	103	9	0
$\lvert\uparrow_z\downarrow_x\rangle$	67	424	3	1
$\lvert\downarrow_z\uparrow_x\rangle$	3	3	35	502
$\lvert\downarrow_z\downarrow_x\rangle$	0	0	402	95

a gate attempt is $P = 0.006$. However, the only intrinsic limitation to this probability stems from the light losses of $5\,\%$ in the transmission of the light at $780\,\mathrm{nm}$ through the 60-m-long fiber. The other numbers impacting the success probability can all be improved by technical enhancements and a good single-photon source of appropriate bandwidth and wavelength.

5.5.2. Measurement of the Truth Table

As outlined in Chapter 5.3, our nonlocal gate scheme acts as a CNOT gate in the basis of $\lvert\uparrow_z\rangle / \lvert\downarrow_z\rangle$ for one and $\lvert\uparrow_x\rangle / \lvert\downarrow_x\rangle$ for the other atomic qubit. For this measurement, the qubit in the QGate module is chosen to be prepared in the energy eigenbasis $\lvert\uparrow_z\rangle / \lvert\downarrow_z\rangle$, as there are already the feedback rotations performed on this qubit. The additional pulses to work with $\lvert\uparrow_x\rangle / \lvert\downarrow_x\rangle$ in preparation and detection are added only on the Pistol side of the protocol. This has the additional advantage that decoherence effects on the QGate side are reduced. On the Pistol setup, a lot of work has been already put into eliminating time-dependent decoherence mechanisms for a recent paper [202].

The qubits are prepared in all four possible combinations of the input states, namely $\lvert\uparrow_z\uparrow_x\rangle$, $\lvert\uparrow_z\downarrow_x\rangle$, $\lvert\downarrow_z\uparrow_x\rangle$ and $\lvert\downarrow_z\downarrow_x\rangle$. After each gate protocol, the QGate atom is measured in the z-basis and the Pistol atom in the x-basis. Only outcomes when the mediating photon has been measured to herald the successful transmission are considered. The results of this experiment in terms of the number of detections in the various states for each input state are given in Table 5.2. From these clicks, the truth table shown in Fig. 5.8 is derived. The errors given in the figure are obtained by assuming independent counting statistics in the measurement. Furthermore, the truth table of an ideal CNOT gate is displayed as a lightly shaded reference in this figure. An ideal CNOT gate should only have four bars that equal defined output state per input state and it should display the swap in the target state, if a control qubit is in the correct state. While there are smaller contributions of other output states for each input due to various error sources (discussed in Chapter 5.6.1), there is always one clearly dominant output state visible in the measured data. Labeling the QGate qubit as the control and the Pistol qubit as the target, the basis state in Pistol is flipped
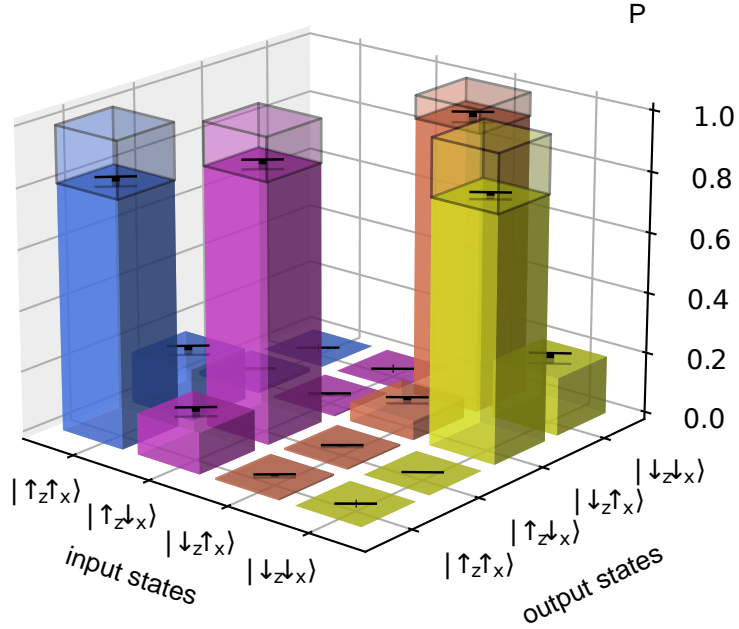
Figure 5.8.: CNOT truth table of the nonlocal gate protocol. The truth table of our quantum gate protocol is shown. The black ranges on top of each bar indicate the statistical errors, assuming independent photon statistics. The light shaded bars give an ideal CNOT truth table as a reference.

whenever the QGate atom in the state $|\downarrow_z\rangle$. For a perfect CNOT gate, this transformation is

$$
\begin{aligned}
|\uparrow_z\uparrow_x\rangle &\longrightarrow |\uparrow_z\uparrow_x\rangle \\
|\uparrow_z\downarrow_x\rangle &\longrightarrow |\uparrow_z\downarrow_x\rangle \\
|\downarrow_z\uparrow_x\rangle &\longrightarrow |\downarrow_z\downarrow_x\rangle \\
|\downarrow_z\downarrow_x\rangle &\longrightarrow |\downarrow_z\uparrow_x\rangle \,.
\end{aligned}
\tag{5.16}
$$

The overlap fidelity of our measured values with those expected for an ideal CNOT gate is $F = (85.1 \pm 0.8)\,\%$ (the error is calculated by error propagation under the assumption of independent errors of the different bars). While additional measurements are necessary to demonstrate the quantum nature of the gate and to analyze possible relative phases in the unitary, the truth table measurement already shows the hallmark signature of a CNOT gate.
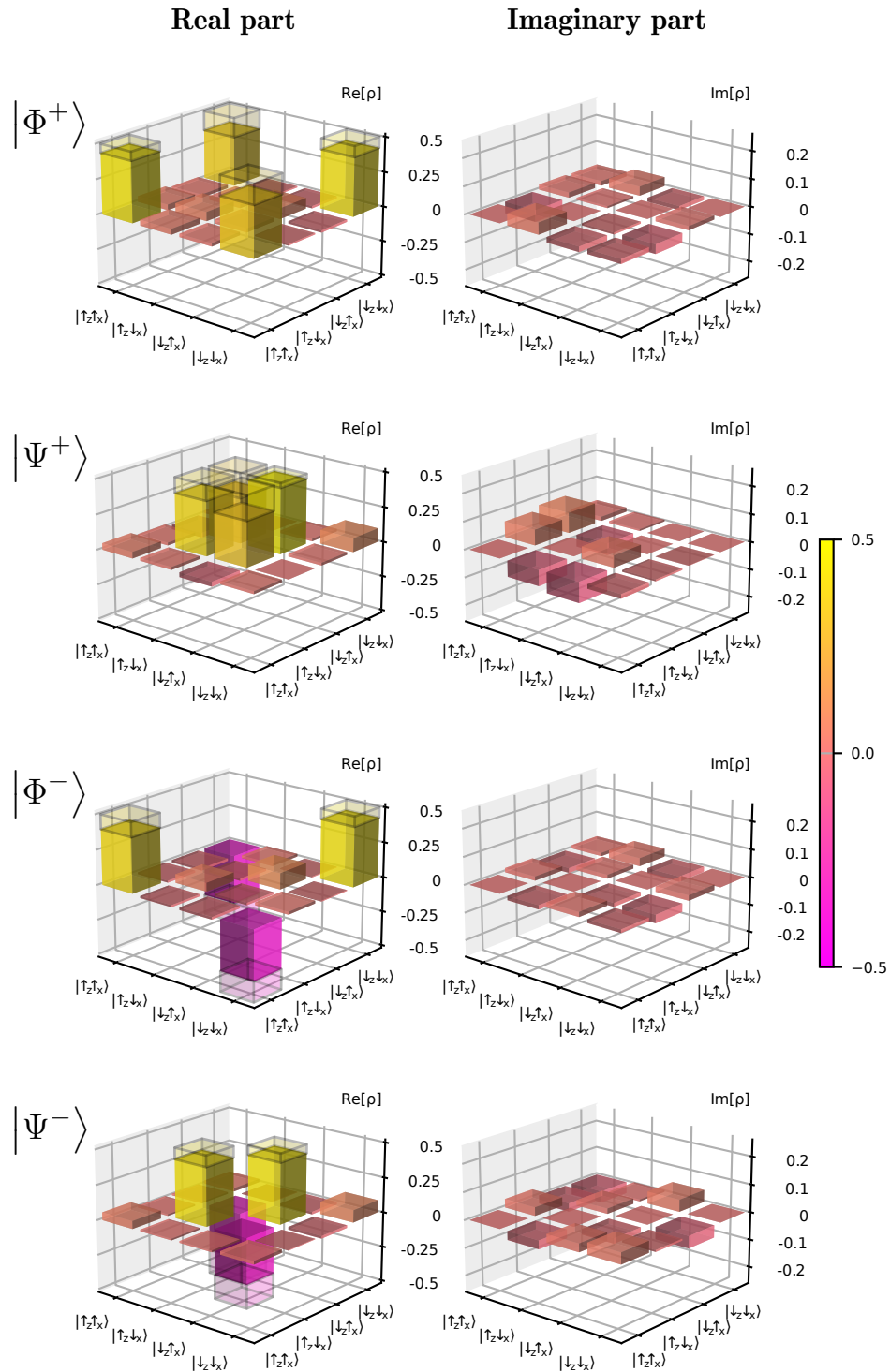
Figure 5.9.: Bell states realized with the nonlocal gate protocol. The real and imaginary parts of the produced density matrices are shown. The ideally expected values are added as light shaded bars.

5.5.3. Creation of the Four Bell States

The coherent quantum character of our protocol is demonstrated by producing all four maximally-entangled Bell states. These measurements also help to identify our gate as a CNOT, as examined in Chapter 5.2 and discussed further below. To produce each of the different Bell states, the nonlocal gate protocol is applied to four different input states

$$
\begin{aligned}
|\uparrow_x\uparrow_x\rangle &\longrightarrow |\Phi^+\rangle \\
|\uparrow_x\downarrow_x\rangle &\longrightarrow |\Psi^+\rangle \\
|\downarrow_x\uparrow_x\rangle &\longrightarrow |\Phi^-\rangle \\
|\downarrow_x\downarrow_x\rangle &\longrightarrow |\Psi^-\rangle ,
\end{aligned}
\tag{5.17}
$$

as outlined in Chapter 5.3. To analyze the resulting state, a full two-qubit tomography is performed by measuring both qubits in the different detection bases $|\uparrow_x\rangle / |\downarrow_x\rangle$, $|\uparrow_y\rangle / |\downarrow_y\rangle$ and $|\uparrow_z\rangle / |\downarrow_z\rangle$ [198]. The switching between the different bases is done randomly (automated at the QGate side and by hand on the Pistol side). From the obtained click distributions, the corresponding density matrices are reconstructed. The results for all four Bell states are displayed in Fig. 5.9, where the real and imaginary parts of the final density matrices are shown separately. The overlap fidelities for the different produced states with the ideally expected Bell states are given in Table 5.3. An average fidelity of $\bar{F} = (76.6 \pm 1.0)\%$ is achieved. This demonstrates that our gate is able to produce entanglement well beyond the classical threshold of $F = 50\%$. The experimental imperfections that limit the fidelity of our implementation are again discussed in Chapter 5.6.1.

Although the application potential of a quantum gate far exceeds the creation of entanglement, it is still interesting to compare this aspect to the entanglement generation that has been done with the same experimental setups in 2012 [61, 122]. In this prior work, a photon has been generated in the first atom-cavity system in a stimulated Raman adiabatic passage process, and it was stored in the atom of the other cavity. With this, entanglement fidelities of $(85.0 \pm 1.3)\%$ were measured at a generation efficiency of 2% and with a read-out efficiency of 0.16%. While the fidelity and the pure generation rate were higher in 2012 (with different aspects limiting either compared to the present protocol), the quantum gate approach has an important advantage, namely the availability of a herald. The heralding can allow, for example, to use the entanglement as a resource that is available

Table 5.3.: Results of the Bell-state generation. The ideally expected output states (up to a global phase) and the achieved overlap fidelity with them after our nonlocal gate protocol for all four prepared input states is displayed.

Input states	Output states	Fidelity
$\lvert\uparrow_x\uparrow_x\rangle$	$\frac{1}{\sqrt{2}}\left(\lvert\uparrow_z\uparrow_x\rangle + \lvert\downarrow_z\downarrow_x\rangle\right) = \lvert\Phi^+\rangle$	$(78.8 \pm 2.0)\%$
$\lvert\uparrow_x\downarrow_x\rangle$	$\frac{1}{\sqrt{2}}\left(\lvert\uparrow_z\downarrow_x\rangle + \lvert\downarrow_z\uparrow_x\rangle\right) = \lvert\Psi^+\rangle$	$(75.1 \pm 2.0)\%$
$\lvert\downarrow_x\uparrow_x\rangle$	$\frac{1}{\sqrt{2}}\left(\lvert\uparrow_z\uparrow_x\rangle - \lvert\downarrow_z\downarrow_x\rangle\right) = \lvert\Phi^-\rangle$	$(76.8 \pm 2.0)\%$
$\lvert\downarrow_x\downarrow_x\rangle$	$\frac{1}{\sqrt{2}}\left(\lvert\uparrow_z\downarrow_x\rangle - \lvert\downarrow_z\uparrow_x\rangle\right) = \lvert\Psi^-\rangle$	$(75.8 \pm 2.0)\%$

for further processing or for other protocols. There are furthermore smaller conceptual differences between the two entanglement creation processes: In 2012, the entangled states were in different hyperfine manifolds in the two atoms, whereas the quantum gate uses the same qubit states, which is an advantage in the construction of larger modular systems. Additionally, in this work, the connecting photon remains available to possibly interact with more systems which could allow for extensions and derivatives of the gate protocol. For these reasons, the generation of entanglement presented in this thesis outlines a very useful technique, even in the context of the work done in 2012, although both the fidelity and the efficiency still require improvement. The imperfections to be addressed for such enhancements are discussed in Chapter 5.6.1.

5.5.4. Discussing the Evidence of a CNOT Gate

As was discussed in Chapter 5.2, the evidence stemming from the truth table measurement is not enough to label a gate as a CNOT. The unitary transformation performed by a gate protocol might still have arbitrary relative phases δ, θ and ζ between the truth table results of the four different input states $|\uparrow_z\uparrow_x\rangle$, $|\uparrow_z\downarrow_x\rangle$, $|\downarrow_z\uparrow_x\rangle$ and $|\downarrow_z\downarrow_x\rangle$. For a CNOT, is it required that $\delta = \theta = \zeta = 0$, which is tested by employing the gate to superposition states of the aforementioned inputs. It was already shown above, that applying the gate to $|\uparrow_x\uparrow_x\rangle$ and $|\uparrow_x\downarrow_x\rangle$ results in the respective Bell states $|\Phi^+\rangle$ and $|\Psi^+\rangle$, as is expected for relative phases of $\zeta = 0$ and $\theta = \delta$ in the gate unitary. The remaining phase δ can be determined by a gate operation on $|\uparrow_z\uparrow_z\rangle$. A non-zero relative phase δ would result in a rotation of the atom in the second module out of its energy eigenstate (see Chapter 5.2). However, in the gate operation, this module experiences only the reflection of the photon and no further pulses. This can not result in a rotation away from the energy eigenstate $|\uparrow_z\rangle$. As expected, in a measurement reflecting a photon successively from the two modules with the qubits in $|\uparrow_z\uparrow_z\rangle$, the initial state is preserved with a measured probability of $(98.6 \pm 0.6)\,\%$. This is expected for $\delta = 0$ and, as a conclusion and within the experimental imperfections, the gate presented here is indeed a quantum CNOT gate.

5.6. Error Analysis and Simulation

In order to evaluate how different experimental imperfections affect the fidelities for both the truth table measurement and the Bell-state production, a simulation of our experiment is performed using the Python library QuTip [171]. For this, the cavities are modeled using the input-output formalism (see Chapter 2.1.2) and for each cavity interaction the light modes that are reflected, transmitted, or scattered from the mirrors or the atom are considered. In the simulation, this is implemented using concatenated beam splitters [125, 153]. At the end of the calculation, the unwanted light modes are traced out. In the present section, I first describe the identified physical imperfections of our setup before I show the result of how big their impact on the measured fidelity is according to the simulation.

5.6.1. Experimental Imperfections

Transversal mode matching: The photons are propagating through the system starting from a fiber output via a low reflectivity beam splitter (a Semrock filter) to the QGate cavity and then from there via the long transmission fiber to the Pistol resonator and back again to the fiber, as shown in Fig. 5.5. As explained in Chapter 2.1.3, imperfect transversal mode matchings between the fibers and the cavities lead to an interference in the collecting fiber between light that is interacting with the atom-resonator system and directly reflected light. Thus imperfect mode matching lowers the overall performance of the gate protocol. The simulation is used to gauge the magnitude of this effect. There are three fiber matchings to be taken into account: On the QGate side, there is the outcoupling fiber for light going to the cavity and there is the long fiber picking up the light after the reflection from the resonator. On the Pistol side, the output of the long fiber and circulator combination is again the input after the interaction with the cavity. Therefore, the relevant parameters (see Chapter 2.1.3) on the QGate side are the intensity mode matchings η_{out} and η_{long} and the relative phase between light in the picked-up matched and unmatched modes ϕ^*_{QGate}. On the Pistol side, there is the mode matching η_{Pistol} and the respective relative phase ϕ^*_{Pistol}. The effects of the two relative phases on the overall fidelities were found to be minor compared to the other parameters. Therefore, both ϕ^*_{QGate} and ϕ^*_{Pistol} are estimated by the value found in [108] with a large fidelity interval of $\phi^*_j = 0.17 \pm 0.17$ for $j \in \{\text{QGate}, \text{Pistol}\}$. The mode matching at the long fiber is bound from below by using the power transmission of 0.55 ± 0.05 though the fiber and taking into account the losses caused by the optical circulator. As a result, this matching is assumed to be $\eta_{\text{long}} = 0.69 \pm 0.05$ to get an upper bound on the related error. The matching η_{out} can be estimated by either a reverse transmission measurement through the fiber using light from the cavity mode or by the cavity spectrum for a coupling and a noncoupling atom that is defined by the cQED parameters and the mode matching. This results in $\eta_{\text{out,QGate}} = 0.94 \pm 0.02$. Lastly, it was found that $\eta_{\text{out,Pistol}} = 0.98 \pm 0.01$.

Weak coherent pulses: As discussed further above, weak coherent pulses are used in this series of experiment to approximate the single photon traveling between the modules. We have a probability of 0.0060(6) to measure a heralding click in each run of the experiment with the atoms in an equal superposition of energy eigenstates. From the mode matching and the cavity parameters, the average reflectivities on resonance $R = (r(\uparrow)^2 + r(\downarrow)^2)/2$ can be calculated to be $R_{\text{QGate}} = 0.60 \pm 0.03$ and $R_{\text{Pistol}} = 0.55 \pm 0.01$. The transmission probability between the two resonators is impacted by other elements in the beam path shown in Fig. 5.5. Apart from the long fiber, there are the AOM pathswitch, the Semrock filter, 6 mirrors and four lenses and the total transmission including the fiber is $T = 0.52 \pm 0.05$. Lastly, there is the detection efficiency of $\eta_{\text{eff}} = 0.5 \pm 0.03$. Using these numbers, the average input-photon number is $\overline{n} = 0.07 \pm 0.01$ per pulse.

Decoherence: In the quoted experiments to test the performance of the nonlocal gate, there is always at least one atom in either QGate or Pistol in a superposition state. Therefore, the fidelities are always affected by dephasing effects that drive superpositions of the energy eigenstates to a statistical mixture. Relaxation effects can be neglected on
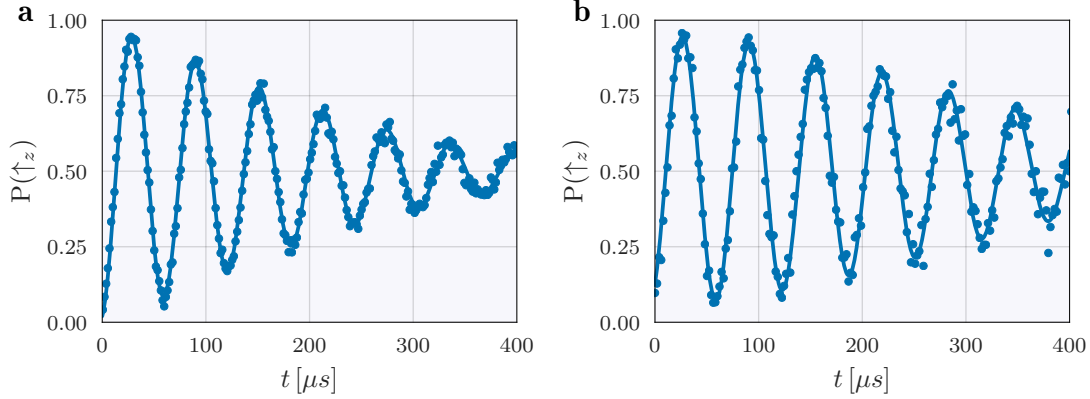
Figure 5.10.: Decoherence in the two setups. The figure shows the measured populations in the state $|\uparrow_z\rangle$ for a Ramsey experiment with waiting time t between the pulses in blue. The decoherence becomes apparent as a decay of the oscillation amplitude. Shown as a solid line is a fit used to obtain the time constants given in the main text. Part **a** shows the Ramsey experiment results for QGate and part **b** shows them for the Pistol setup.

the time scales relevant for the experiment and therefore dephasing and decoherence are used equivalently in the following. In order to estimate the effect of it on the measured fidelities, the respective decoherence times are the crucial parameter. To obtain them, a Ramsey type experiment is performed preparing the atoms in $|\uparrow_z\rangle$ and using two $\pi/2$ pulses separated by a variable time t before the population in $|\uparrow_z\rangle$ is measured after the last pulse. The resulting curve for a scan of t can be fitted with a cosine with decaying amplitude. For the Pistol setup, this decay is well described by a Gaussian decay $\approx \exp(-t^2/\tau_{pist}^2)$ and a decay constant of $\tau_{pist} = (390 \pm 17)\,\mu s$ was measured. The result of this measurement including the fit is shown in Fig. 5.10**b**. The statistical error given is extracted from the fit to the data. However, a larger systematic error is expected due to the $1064\,nm$ trap and fluctuating magnetic fields that were not controlled during this measurement and in the following $\tau_{pist} = (390 \pm 100)\,\mu s$ is assumed.

On the QGate setup, the decoherence is best fitted with both a Gaussian and an exponential decay $\approx \exp(-t/\tau_{q1})\exp(-t^2/\tau_{q2}^2)$ with $\tau_{q1} = (401 \pm 21)\,\mu s$ and $\tau_{q2} = (372 \pm 15)\,\mu s$. The measured data and the fit are shown in Fig. 5.10**a**. The errors are derived as the statistical errors from the fit. Furthermore, from the fit of the QGate data, an offset of the cosine can be extracted. It results from the decoherence happening for two $\pi/2$ pulses with a non-zero duration that are applied without any waiting period. Here, the effective additional time during which the state can decay is $t_{\text{eff}} = (2.15 \pm 0.10)\,\mu s$, and it has to be added to the protocol time on the QGate side.

State preparation and measurement errors: The infidelity in the state preparation and measurement (SPAM) is considered as an average over the various bases used, as these numbers do depend on the different preparation and detection axes of the experimental run. In general, the highest fidelity is achieved when pumping the atoms to $|\uparrow_z\rangle$ and when measuring them along the z-axis, where no additional single qubit rotations are needed.

For other combinations, the required Raman pulses introduce an additional source of error, especially as drifts and fluctuations in the ambient magnetic fields can affect the atomic transition frequency $|\uparrow_z\rangle \leftrightarrow |e\rangle$ and thus – via the changed rotation angle – the fidelity during longer measurements. While this has been compensated every 60 min to 90 min, it still has residual effects. From detections in the different bases and from the observed visibility of Rabi oscillations between the measurements, a fidelity of the SPAM of 0.96 ± 0.015 is assumed in both the QGate and the Pistol experiment.

Polarization effects and cavity birefringences: As pointed out in Chapter 5.4.3, there are effects from polarization-dependent losses and an imperfect waveplate rotation in the matching of the polarization bases at different places of the combined experimental setup. In a first step, these imperfections were included in the simulation using variable parameters in the light transmission of the long fiber. Then the free parameters were fitted with the target to reproduce the measured click distribution shown in Table 5.1. The fit was repeated with different starting values to check if there are various parameter sets that might lead to the same click pattern that was observed. Two such sets were found, with one being more unlikely as a retardation far-off from a quarter-wave plate is compensated with bigger polarization-dependent losses. This second set of parameters is therefore only used to estimate the fidelity range of the error caused by polarization effects, whereas the other set is used generally in the simulation.

Furthermore, a small depolarization of 0.005 ± 0.005 in the long fiber is included in the simulation. This addresses the limited accuracy of the used polarimeter and the residual error in the automatic compensation. Lastly, an additional error related to the polarization of the light stems from the birefringences of the resonators introduced in Chapter 3.3. In the procedure employed to match the polarizations at the different parts of the setup, the cavities are locked and no atom is loaded. With a strongly-coupled atom, however, light polarized in $|R\rangle$ can not enter the cavity anymore and gets directly reflected. As a consequence of this, it is not rotated by the birefringence that affects only light that enters the resonators. As this happens only for the atom in the coupling state $|\uparrow_z\rangle$, it leads to a small polarization difference in the reflected light depending on the atomic state. This effect is also included in the simulation.

Cavity width and detuning: The amplitudes and phases of the reflectivites of both resonators depend on the detuning between the incoming light and the cavity frequencies (see Chapter 2.1.1). To get these numbers, the reflection spectra of the resonators are compared using frequency-scanned light from the same source, in this case the weak coherent states from the QGate experiment. As the QGate resonator has an in-sequence stabilization of drifts of the resonator [125], the detuning of it can be assumed to be zero. Measuring the resonance frequency of the Pistol cavity relative to the other setup, it was found that $\Delta_{\mathrm{Pistol}} = 2\pi \, (0.3 \pm 0.1)$ MHz.

Another important feature affecting the detuning comes from the fluctuation of the cavity lock around its central frequency. It can lead to slightly different detunings from shot to shot and thus lowers the fidelity in the aggregated data over many experiments. To measure the fluctuations, power-stabilized light that is detuned from the cavity by $\approx \kappa$ can be sent

though the resonator to be detected afterwards. As it is not at the central frequency but at the side of the transmission spectrum, fluctuations in the central frequency will translate to fluctuations of the measured power after the resonator. If the frequency drifts closer to resonance, more light passes, for drifts in the other direction the measured power is lower. The width of the lock can then be extracted from the width of the measured power spectrum around its central value. For QGate, a standard deviation of $\sigma_{\text{QGate}} = 2\pi \, (205 \pm 50)$ kHz around the mean was found and for Pistol a value of $\sigma_{\text{Pistol}} = 2\pi \, (200 \pm 50)$ kHz is estimated. In the simulation, this distribution of the resonator frequency has been implemented using a Monte Carlo simulation using 750 detuning samples chosen randomly from a Gaussian distribution with the width given above.

Other imperfections: Additional to the experimental parameters mentioned in this section, the cQED parameters play a role as they lead to losses and can leak information about the atomic state (see Chapter 2.1.2). Lastly, the SNSPDs have a (9.5 ± 0.5) Hz dark-count rate per channel of clicks, independent of any incoming light that stems mostly from light leakage. This leads to false positives and therefore to a reduction in the measured fidelities. For achieving this low dark-count rate, the light in the room of the detectors has to be switched off, as otherwise more light couples into the fibers just before the detectors. In the simulation, the dark-count rate is included taking into account the $2\,\mu s$ detection window of the photon.

5.6.2. Impact on the Achieved Fidelities

The effect of the individual experimental imperfections on the fidelity is estimated using the simulation. First a baseline fidelity is established by including all imperfections except for the frequency width of the cavity lock, as it requires a Monte-Carlo approach. To attribute numbers to the impact of the different parameters on the fidelity, each of them is switched off individually and the resulting fidelity is compared to the established base value. In this way, it is taken into account that the effects of the different deficiencies are not independent of each other and can have cross effects with the other imperfections. Thus, the fidelity reduction of each individual element is to be understood as a value valid for the realized settings. Improvements in some of the parameters in the future could also affect the error contributions of different experimental imperfections.

The calculation of the effect of the frequency width of the cavity lock with the Monte Carlo method is done on top of the baseline error established for the other parameters. The impact of the cavity QED parameters is at the heart of the simulation and can not be easily switched off by a using a different set of parameters. The error caused by them is therefore estimated by comparing an otherwise perfect scenario to a unity fidelity. The fidelity reduction of the mode matching was calculated similarly, with only the imperfections of the cavity QED parameters included otherwise.

The fidelity reductions of all different parameters are summarized in Table 5.4, both for the truth table and the Bell-state measurement.

Table 5.4.: Impact of different experimental imperfections on the measured fidelities. The table summarizes the effect of different experimental imperfections in both the truth table and the Bell-state generation measurement. The values are derived from the simulation discussed in the main text.

Imperfection	Effect on truth table	Effect on Bell states
Weak coherent states and losses	$(2.3^{+0.3}_{-0.3})\%$	$(3.8^{+0.5}_{-0.4})\%$
SPAM	$(2.9^{+1.0}_{-1.0})\%$	$(2.7^{+1.0}_{-1.0})\%$
Polarization effects	$(2.2^{+0.3}_{-0.5})\%$	$(2.7^{+0.4}_{-0.6})\%$
Mode matchings	$(2.0^{+1.6}_{-1.2})\%$	$(2.4^{+2.5}_{-1.5})\%$
Lock widths and atom-cavity detunings	$(1.4^{+1.3}_{-0.7})\%$	$(1.9^{+2.8}_{-1.0})\%$
Detector dark counts	$(0.61^{+0.03}_{-0.03})\%$	$(0.74^{+0.04}_{-0.03})\%$
Atomic decoherence	$(0.11^{+0.09}_{-0.03})\%$	$(3.2^{+0.3}_{-0.2})\%$
cQED parameters	0.17%	0.33%

5.7. Perspective and Outlook

With the measurements discussed above, a nonlocal quantum CNOT gate between two qubits in spatially separated network modules has been shown. The gate is heralded, an important feature as fibers operating as optical links between the setups have inherent loss and heralding is a way to deal with the non-deterministic photon transmission. It was shown that the gate operation considered in this chapter has an $(85.1 \pm 0.8)\%$ overlap with an ideal CNOT truth table. Possible additional non-zero phases in a unitary describing our operation have been excluded with the backdrop of the experimental creation of all four maximally-entangled Bell states with an average fidelity of $(76.6 \pm 1.0)\%$ by the gate. In this first implementation, the observed gate fidelity is still limited by various experimental imperfections. For a use in larger modular quantum architectures, the performance still has to be improved. As discussed above, a major step in this direction would be the use of single photons, for example derived from a distillation scheme (see Chapter 4). Also, for various other identified error sources, prescriptions for improvements are available, for example with faster qubit rotations or a better stability of the magnetic fields and cavity center frequencies. All this will help to boost the fidelity in future realizations of this gate, making it feasible in larger multi-module and multi-gate applications.

The gate implementation discussed in this chapter is performed within $22\,\mu s$, which is still slow compared to monolithic state-of-the-art quantum computation architectures (for example, Google's Sycamore processor performs two-qubit gates within $12\,ns$ (see Supplementary Material of [85]), and two-qubit gates mediated by Rydberg excitations in arrays of neutral atoms are done within $400\,ns$ [81]). On one hand, the gate presented here could be sped up with faster rotations and a differently implemented Z feedback. On the other hand, this gate could also be treated by algorithms as a special connecting gate that might not need to be performed at the same speed as the local operations. In this

sense, algorithmic compilations heeding the differing nature of local and nonlocal gates are required to make the most of a larger modular system.

Future steps to establish this nonlocal gate in a larger context could involve connecting modules with several qubits each and also to connect more than two modules, to explore the scaling behavior of distributed systems based on this gate. This could also enable single-step multi-module gates [107].

6. Summary and Outlook

In the work described in this thesis, two quantum-network protocols have been experimentally realized using modules consisting of an atom strongly coupled to an optical cavity.

In Chapter 4, I present a technique that we have used to distill single photons out of a resource coherent state [72]. By applying a parity-projection measurement, the zero- and two-photon components of the incoming weak coherent state have been successfully suppressed. With this, a light state having a $(66 \pm 1)\,\%$ overlap with a single photon has been produced. The remaining infidelity is almost exclusively coming from the vacuum and is largely affected by the imperfect cavity QED parameters. The Wigner function of the state created by this distillation has been reconstructed and the suppression of the higher Fock-state contributions has been confirmed by measuring the second-order correlation function with $g^{(2)}(0) = 0.045 \pm 0.006$.

In Chapter 5, I present the first realization of a quantum gate between stationary qubits in modules that are located in two separate laboratories [94]. The two qubit modules have been connected with a 60-m-long optical fiber as a photonic quantum channel. By reflecting a single photon successively from both setups and by implementing a conditional feedback after the photon measurement, we have been able to demonstrate a universal, nonlocal quantum-logic gate. In the experiments, we have measured an overlap of $(85.1 \pm 0.8)\,\%$ with the truth table of an ideal CNOT gate. Furthermore, the gate has been used to create all four maximally-entangled Bell states with an average fidelity of $(76.6 \pm 1.0)\,\%$ out of separable input states. An important part of the remaining infidelity stems from the use of weak coherent pulses instead of single photons.

For both protocols, possible steps to increase the fidelity in future implementations have been outlined. The fact that the largest limitation for the nonlocal quantum gate could be removed by the use of single photons instead of weak coherent pulses shows that the two protocols could be naturally combined in a quantum network: One module could be used to distill the single photon that is the resource for a gate between distant qubits located in the other modules. It is important to note that such a distillation module would not be required for each two modules that should be connected with a quantum gate: Photons could be routed to specific modules, and it is also possible to tune only the target modules into resonance with the light. Furthermore, it has been proposed that a single photon can be used to connect many modules to perform a single-step Toffoli gate between qubits in them [107]. These perspectives highlight the possibilities that quantum gates based on the reflection of a photon might have in networks with many modules.

I have pointed out that a main challenge in current quantum computing architectures is to scale up the system size to more qubits. The nonlocal gate presented in this work can

enable a different approach where the qubits are distributed over many modules that form together a larger quantum computer. In such a scenario, it might still be desirable to have more than one qubit per module, as the use of fibers lowers the overall efficiency. Together with the scaling constraints in a single system, this could result in a trade-off between the number of qubits per module and the number of modules for a given size of a distributed quantum computer.

To use more qubits in our network modules, several atoms can be trapped at the center of the cavities and each could encode a qubit [111]. Optical tweezers could then be used for an individual preparation, manipulation and detection of each atom. Furthermore, the tweezers would enable an active positioning of the qubits in the resonator, allowing to reload atoms from a reservoir to regions of strong coupling. Techniques of the optical tweezers have been pioneered in the groups of Antoine Browaeys [203] and Mikhail Lukin [204]. They could be implemented in our modules through the high NA objectives with the use of acousto-optical deflectors that are powered by a signal of various frequency components. In the Pistol setup, a single-atom addressing has already been implemented to shoot unwanted atoms out of the cavity [205]. Optical tweezers could furthermore allow to use the AC Stark shift on the atoms to bring specific qubits in- and out of resonance with the cavity. Since the nonlocal quantum gate relies on the reflection of a photon resonant with the atom-cavity system, the AC Stark shift could be used to select individual qubits for a gate operation with another module. In such a setup, nonlocal quantum gates between different modules could be combined with local two-qubit gates based on a photon reflection, that have been demonstrated in [111]. Together, this could allow performing gates between any two qubits of a larger combined, distributed system.

The complete experimental setup of each individual module was still rather large in this work (see e.g. [125] for an overview picture of the optical part of QGate in 2019). However, the majority of this space is required for the laser systems, whereas the resonator at the heart of each module is way smaller [117]. In the recent years, quantum optics experiments are slowly moving toward more compact, integrated systems and this trend toward miniaturization will continue. Today, there are already quantum experiments that can create a Bose-Einstein condensate and use less than $0.1\,\mathrm{m}^3$ for all optics, electronics and shielding [206]. This trend will also result in the modules for quantum networks becoming integrated and smaller, facilitating the construction of larger, modular networks.

An important feature of the protocols presented in this thesis is that they are not limited to the specific experimental platform of single atoms in a cavity. They rely on the phase-shift reflection mechanism that can be realized with any emitter that couples sufficiently strong to a one-sided resonator. First experiments using this mechanism have, for example, already been performed with a charged quantum dot in a photonic crystal cavity [207] or with a superconducting artificial atom and a microwave cavity [208]. Each experimental platform has its own advantages and challenges [60], and it is not clear if future developments will favor one system over the others. Therefore, it is valuable to devise protocols that are applicable to different platforms and that might thus be useful tools in quantum networks beyond a specific implementation.

Today more than ever, the field of quantum networks and quantum computation is blooming: First quantum key distribution systems are commercially sold and investments in quantum

computing are huge, resulting in many start-ups and big tech corporations entering the field. The interest in quantum technology is also taken up by the funding agencies worldwide, reflecting the potential and value that is expected from harnessing the power of individual quantum constituents. All of this will result in many novel applications in the years to come, using and expanding the protocols that exist so far. The field of quantum information processing is therefore a fertile ground for the tools presented in this work, and it will be interesting to see how they will be incorporated in future systems.

A. Atomic and Photonic Qubit Transformations

The effect of a quarter-wave plate (depending on the orientation of the birefringence axes) in this basis of $|R\rangle / |L\rangle$ is given by the matrices

$$T_{\lambda/4} = \frac{1}{\sqrt{2}} \begin{pmatrix} -i & 1 \\ 1 & -i \end{pmatrix}, \quad T_{-\lambda/4} = \frac{1}{\sqrt{2}} \begin{pmatrix} i & 1 \\ 1 & i \end{pmatrix}. \tag{A.1}$$

Similarly, for an atom in the basis of $|\uparrow_z\rangle / |\downarrow_z\rangle$, the effect of π and $\pi/2$ rotations around the x- and y-axes are given by the transformations

$$T_{\pi/2}^y = \frac{1}{\sqrt{2}} \begin{pmatrix} 1 & -1 \\ 1 & 1 \end{pmatrix}, \quad T_{\pi/2}^x = \frac{1}{\sqrt{2}} \begin{pmatrix} 1 & -i \\ -i & 1 \end{pmatrix} \tag{A.2}$$

and

$$T_{\pi}^y = \begin{pmatrix} 0 & -1 \\ 1 & 0 \end{pmatrix}, \quad T_{\pi}^x = \begin{pmatrix} 0 & -i \\ -i & 0 \end{pmatrix}, \tag{A.3}$$

with the rotation angle given as the subscript and the rotation axis indicated as the superscript.

B. Wave Functions and Wigner Distributions

The Wigner functions for a given density matrix ρ or for for a given wave function ψ are

$$W_{\hat{\rho}}(x,p) = \frac{1}{\pi} \int e^{2iyp/\hbar} \langle x+y| \, \hat{\rho} \, |x-y\rangle \, dy, \tag{B.1}$$

or

$$W_{\psi}(x,p) = \frac{1}{\pi} \int e^{2iyp/\hbar} \psi^{\star}(x+y)\psi(x-y)dy. \tag{B.2}$$

To obtain the Wigner functions of the vacuum and the single-photon states, the annihilation operator for the harmonic oscillator can be used:

$$a = \sqrt{\frac{m\omega}{2\hbar}} \left(\hat{x} + \frac{i}{m\omega}\hat{p} \right), \qquad \left[a, a^{\dagger} \right] = 1. \tag{B.3}$$

The wave function of the vacuum is straightforwardly obtained with $a\,|0\rangle = 0$ multiplied by $\langle x|$ and the transition to position space $(\hat{p} \to -i\hbar\partial_x, |0\rangle \to \langle x|\, 0\, |=\rangle \psi_0(x))$, leading to

$$\psi_0(x) = \frac{1}{\sqrt{\sqrt{\pi}x_0}} e^{-\frac{x^2}{2x_0^2}} \tag{B.4}$$

with $x_0 = \sqrt{\hbar/(m\omega)}$. Similarly the wave functions for higher Fock states can be calculated. Using the Hermite polynomials

$$H_n(x) = (-1)^n e^{x^2} \left(\frac{d}{dx} \right)^n e^{-x^2}, \tag{B.5}$$

the Fock wave-functions are

$$\psi_n(x) = \frac{1}{\sqrt{2^n(n!)}} \left(\frac{1}{\pi x_0^2} \right)^{\frac{1}{4}} H_n\left(\frac{x}{x_0} \right) e^{-\frac{x^2}{2x_0^2}}. \tag{B.6}$$

The equations become more elegant by switching to the dimensionless quadratures

$$\mathcal{X} = \frac{x}{x_0}, \qquad \mathcal{P} = \frac{x_0 p}{\hbar}, \tag{B.7}$$

To calculate the Wigner function for the vacuum, a straight-forward Gaussian integral yields

$$W_0(\mathcal{X}, \mathcal{P}) = \frac{1}{\pi} e^{-\mathcal{X}^2 - \mathcal{P}^2}. \tag{B.8}$$

For a general Fock state, the solution can be expressed with the Laguerre polynomials, which are defined as

$$L_n(x) := \frac{e^x}{n!} \frac{d^n}{dx^n} \left(x^n e^{-x} \right). \tag{B.9}$$

This yields the Wigner functions

$$W_n(\mathcal{X}, \mathcal{P}) = \frac{(-1)^n}{\pi} \exp\left[-\left(\mathcal{P}^2 + \mathcal{X}^2\right)\right] L_n\left[2\left(\mathcal{P}^2 + \mathcal{X}^2\right)\right] \tag{B.10}$$

and therefore for a single photon

$$W_1(\mathcal{X}, \mathcal{P}) = \frac{-1}{\pi} e^{-\left(\mathcal{P}^2 + \mathcal{X}^2\right)} \left[1 - 2\left(\mathcal{P}^2 + \mathcal{X}^2\right)\right]. \tag{B.11}$$

C. Circuit Diagram of the Homodyne Detector

Homodyne Detector
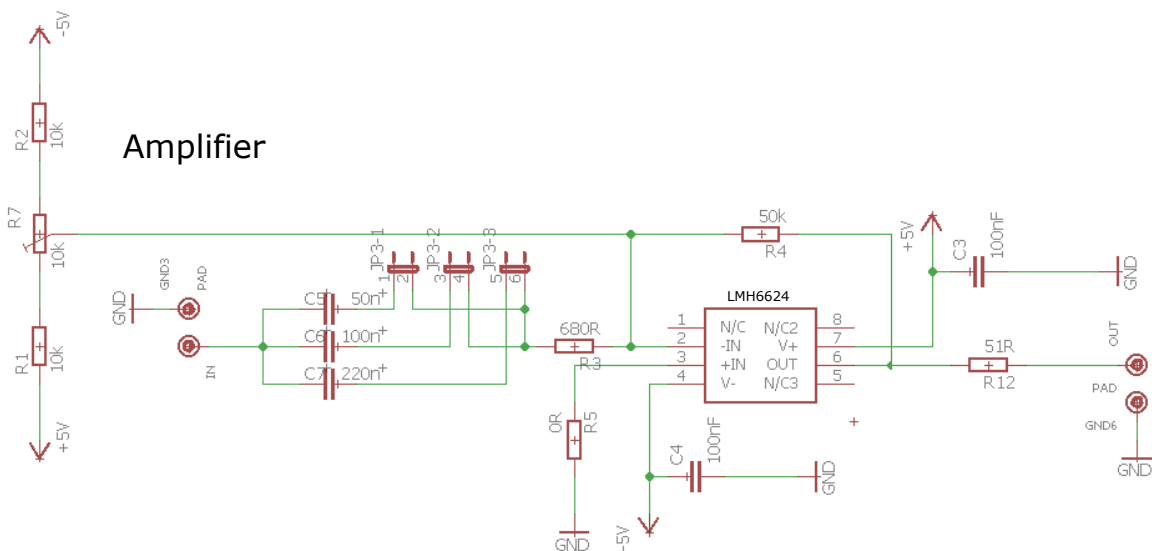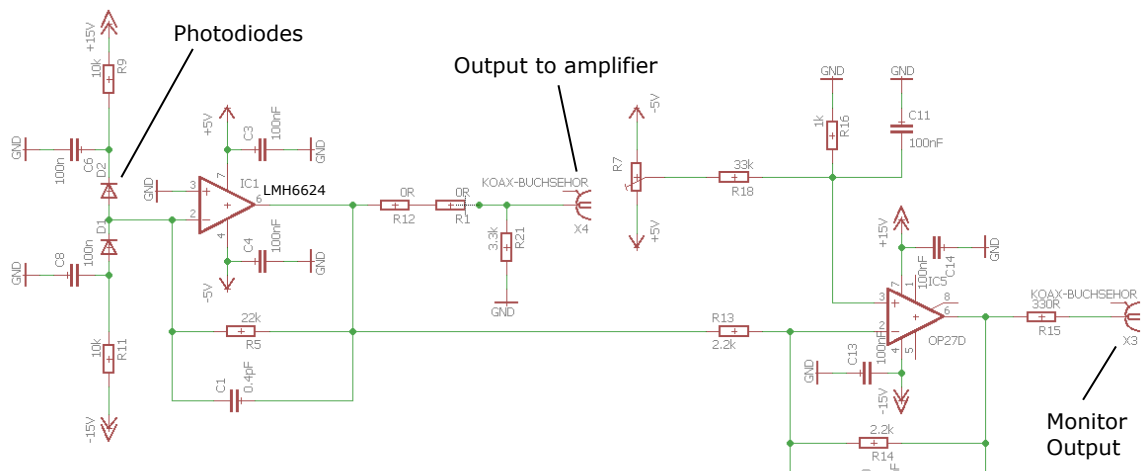
Amplifier

Figure C.1.: Circuit diagrams of the homodyne detector and the amplifier used in the distillation experiment. In both diagrams, the voltage regulators have been omitted.

D. List of Abbreviations

AOM	accousto-optical modulator
CNOT	controlled-NOT
cQED	cavity quantum electrodynamics
EPR	Einstein, Podolski and Rosen
FPGA	field-programmable gate array
LO	local oscillator
MOT	magneto-optical trap
NA	numerial aperture
ND	nondestructive
NPBS	nonpolarizing beam splitter
PD	photodiode
QEC	quantum error correction
QIP	quantum information processing
RF	radio frequency
SNSPD	superconducting nanowire single-photon detector
SPAM	state preparation and measurement
SPD	single-photon detector

Bibliography

[1] M. Planck. *Zur Theorie des Gesetzes der Energieverteilung im Normalspectrum. Verhandlungen der deutschen physikalischen Gesellschaft* **2**, 237–245 (1900).

[2] A. Einstein. *Über einen die Erzeugung und Verwandlung des Lichtes betreffenden heuristischen Gesichtspunkt. Ann. Phys.* **322**, 132–148 (1905).

[3] G. N. Lewis. *The Conservation of Photons. Nature* **118**, 874–875 (1926).

[4] N. Bohr. On the Constitution of Atoms and Molecules. In O. Darrigol, B. Duplantier, J.-M. Raimond & V. Rivasseau (eds.) *Niels Bohr, 1913-2013: Poincaré Seminar 2013*, 13–33 (Springer, 2016).

[5] M. Born & P. Jordan. *Zur Quantenmechanik. Z. Physik* **34**, 858–888 (1925).

[6] De Broglie, Louis. *Recherches sur la théorie des Quanta. Ann. Phys.* **10**, 22–128 (1925).

[7] W. Pauli. *Über den Zusammenhang des Abschlusses der Elektronengruppen im Atom mit der Komplexstruktur der Spektren. Z. Physik* **31**, 765–783 (1925).

[8] W. Heisenberg. *Über quantentheoretische Umdeutung kinematischer und mechanischer Beziehungen. Z. Physik* **33**, 879–893 (1925).

[9] P. A. M. Dirac & R. H. Fowler. *The fundamental equations of quantum mechanics. Proc. R. Soc. Lond. A* **109**, 642–653 (1925).

[10] E. Schrödinger. *Quantisierung als Eigenwertproblem. Ann. Phys.* **384**, 361–376 (1926).

[11] N. Bohr. In J. A. Wheeler & W. H. Zurek (eds.) *Quantum Theory and Measurement*, 9–49 (Princeton Univ. Press, 1983).

[12] E. Schrödinger. *Die gegenwärtige Situation in der Quantenmechanik. Naturwissenschaften* **23**, 807–812 (1935).

[13] E. Schrödinger. *ARE THERE QUANTUM JUMPS?: PART II*. The British Journal for the Philosophy of Science* **3**, 233–242 (1952).

[14] T. H. Maiman. *Stimulated Optical Radiation in Ruby. Nature* **187**, 493–494 (1960).

[15] S. V. Andreev, V. I. Balykin, V. S. Letokhov & V. G. Minogin. *Radiative slowing and reduction of the energy spread of a beam of sodium atoms to 1.5 K in an oppositely directed laser beam. JETP Letters* **34**, 442–445 (1981).

[16] W. D. Phillips, J. V. Prodan & H. J. Metcalf. *Neutral atomic beam cooling experiments at NBS. Progress in Quantum Electronics* **8**, 119–127 (1984).

[17] J. Prodan, A. Migdall, W. D. Phillips, I. So, H. Metcalf & J. Dalibard. *Stopping Atoms with Laser Light. Phys. Rev. Lett.* **54**, 992–995 (1985).

[18] W. Ertmer, R. Blatt, J. L. Hall & M. Zhu. *Laser Manipulation of Atomic Beam Velocities: Demonstration of Stopped Atoms and Velocity Reversal. Phys. Rev. Lett.* **54**, 996–999 (1985).

[19] W. D. Phillips. *Nobel Lecture: Laser cooling and trapping of neutral atoms. Rev. Mod. Phys.* **70**, 721–741 (1998).

[20] C. N. Cohen-Tannoudji. *Nobel Lecture: Manipulating atoms with photons. Rev. Mod. Phys.* **70**, 707–719 (1998).

[21] S. Chu. *Nobel Lecture: The manipulation of neutral particles. Rev. Mod. Phys.* **70**, 685–706 (1998).

[22] A. Einstein. *Quantentheorie des einatomigen idealen Gases. Königliche Preußische Akademie der Wissenschaften. Sitzungsberichte* 261–267 (1924).

[23] W. Ketterle. *Nobel lecture: When atoms behave as waves: Bose-Einstein condensation and the atom laser. Rev. Mod. Phys.* **74**, 1131–1151 (2002).

[24] E. A. Cornell & C. E. Wieman. *Nobel Lecture: Bose-Einstein condensation in a dilute gas, the first 70 years and some recent experiments. Rev. Mod. Phys.* **74**, 875–893 (2002).

[25] A. Ashkin, J. M. Dziedzic, J. E. Bjorkholm & S. Chu. *Observation of a single-beam gradient force optical trap for dielectric particles. Opt. Lett.* **11**, 288–290 (1986).

[26] C. I. Westbrook, R. N. Watts, C. E. Tanner, S. L. Rolston, W. D. Phillips, P. D. Lett & P. L. Gould. *Localization of atoms in a three-dimensional standing wave. Phys. Rev. Lett.* **65**, 33–36 (1990).

[27] J. Ye, D. W. Vernooy & H. J. Kimble. *Trapping of Single Atoms in Cavity QED. Phys. Rev. Lett.* **83**, 4987–4990 (1999).

[28] *Hans G. Dehmelt - Biographical. NobelPrize.org. Nobel Prize Outreach AB 2021.* (Accessed: 2021-07-29).

[29] W. Neuhauser, M. Hohenstatt, P. E. Toschek & H. Dehmelt. *Localized visible* Ba^+ *mono-ion oscillator. Phys. Rev. A* **22**, 1137–1140 (1980).

[30] S. Dürr, T. Nonn & G. Rempe. *Origin of quantum-mechanical complementarity probed by a 'which-way' experiment in an atom interferometer. Nature* **395**, 33–37 (1998).

[31] S. Haroche. *Nobel Lecture: Controlling photons in a box and exploring the quantum to classical boundary. Rev. Mod. Phys.* **85**, 1083–1102 (2013).

[32] D. J. Wineland. *Nobel Lecture: Superposition, entanglement, and raising Schrödinger's cat. Rev. Mod. Phys.* **85**, 1103–1114 (2013).

[33] S. Haroche & J.-M. Raimond. *Exploring the Quantum* (Oxford University Press, 2006).

[34] J. P. Dowling & G. J. Milburn. *Quantum technology: the second quantum revolution.* *Phil. Trans. R. Soc. A* **361**, 1655–1674 (2003).

[35] L. Jaeger. *The Second Quantum Revolution* (Copernicus, 2018).

[36] H. J. Kimble. *The quantum internet. Nature* **453**, 1023–1030 (2008).

[37] C. H. Bennett & G. Brassard. *Quantum cryptography: Public key distribution and coin tossing. International Conference on Computers, Systems & Signal Processing, Bangalore, India, Dec 9-12, 1984* 175–179 (1984).

[38] W. K. Wootters & W. H. Zurek. *A single quantum cannot be cloned. Nature* **299**, 802–803 (1982).

[39] S. Pirandola *et al. Advances in quantum cryptography. Adv. Opt. Photon.* **12**, 1012–1236 (2020).

[40] P. Kómár, E. M. Kessler, M. Bishof, L. Jiang, A. S. Sørensen, J. Ye & M. D. Lukin. *A quantum network of clocks. Nat. Phys.* **10**, 582–587 (2014).

[41] X. Guo, C. R. Breum, J. Borregaard, S. Izumi, M. V. Larsen, T. Gehring, M. Christandl, J. S. Neergaard-Nielsen & U. L. Andersen. *Distributed quantum sensing in a continuous-variable entangled network. Nat. Phys.* **16**, 281–284 (2020).

[42] A. Einstein, B. Podolsky & N. Rosen. *Can Quantum-Mechanical Description of Physical Reality Be Considered Complete? Phys. Rev.* **47**, 777–780 (1935).

[43] J. S. Bell. *On the Einstein Podolsky Rosen paradox. Physics* **1**, 195–200 (1964).

[44] S. J. Freedman & J. F. Clauser. *Experimental Test of Local Hidden-Variable Theories. Phys. Rev. Lett.* **28**, 938–941 (1972).

[45] A. Aspect, J. Dalibard & G. Roger. *Experimental Test of Bell's Inequalities Using Time-Varying Analyzers. Phys. Rev. Lett.* **49**, 1804–1807 (1982).

[46] G. Weihs, T. Jennewein, C. Simon, H. Weinfurter & A. Zeilinger. *Violation of Bell's Inequality under Strict Einstein Locality Conditions. Phys. Rev. Lett.* **81**, 5039–5043 (1998).

[47] B. Hensen *et al. Loophole-free Bell test using electron spins in diamond: second experiment and additional analysis. Sci. Rep.* **6**, 30289 (2016).

[48] W. Rosenfeld, D. Burchardt, R. Garthoff, K. Redeker, N. Ortegel, M. Rau & H. Weinfurter. *Event-Ready Bell Test Using Entangled Atoms Simultaneously Closing Detection and Locality Loopholes. Phys. Rev. Lett.* **119**, 010402 (2017).

[49] J. I. Cirac, P. Zoller, H. J. Kimble & H. Mabuchi. *Quantum State Transfer and Entanglement Distribution among Distant Nodes in a Quantum Network. Phys. Rev. Lett.* **78**, 3221–3224 (1997).

[50] L.-M. Duan, M. D. Lukin, J. I. Cirac & P. Zoller. *Long-distance quantum communication with atomic ensembles and linear optics. Nature* **414**, 413–418 (2001).

[51] C. H. Bennett, G. Brassard, C. Crépeau, R. Jozsa, A. Peres & W. K. Wootters.

Teleporting an unknown quantum state via dual classical and Einstein-Podolsky-Rosen channels. Phys. Rev. Lett. **70**, 1895–1899 (1993).

[52] D. Bouwmeester, J.-W. Pan, K. Mattle, M. Eibl, H. Weinfurter & A. Zeilinger. *Experimental quantum teleportation. Nature* **390**, 575–579 (1997).

[53] S. Pirandola, J. Eisert, C. Weedbrook, A. Furusawa & S. L. Braunstein. *Advances in quantum teleportation. Nat. Photon.* **9**, 641–652 (2015).

[54] S.-K. Liao *et al. Satellite-Relayed Intercontinental Quantum Network. Phys. Rev. Lett.* **120**, 030501 (2018).

[55] S.-K. Liao *et al. Satellite-to-ground quantum key distribution. Nature* **549**, 43–47 (2017).

[56] H.-J. Briegel, W. Dür, J. I. Cirac & P. Zoller. *Quantum Repeaters: The Role of Imperfect Local Operations in Quantum Communication. Phys. Rev. Lett.* **81**, 5932–5935 (1998).

[57] M. Uphoff, M. Brekenfeld, G. Rempe & S. Ritter. *An integrated quantum repeater at telecom wavelength with single atoms in optical fiber cavities. Appl. Phys. B* **122**, 46 (2016).

[58] M. Żukowski, A. Zeilinger, M. A. Horne & A. K. Ekert. *"Event-ready-detectors" Bell experiment via entanglement swapping. Phys. Rev. Lett.* **71**, 4287–4290 (1993).

[59] C. H. Bennett, G. Brassard, S. Popescu, B. Schumacher, J. A. Smolin & W. K. Wootters. *Purification of Noisy Entanglement and Faithful Teleportation via Noisy Channels. Phys. Rev. Lett.* **76**, 722–725 (1996).

[60] D. Awschalom *et al. Development of Quantum Interconnects (QuICs) for Next-Generation Information Technologies. PRX Quantum* **2**, 017002 (2021).

[61] S. Ritter, C. Nölleke, C. Hahn, A. Reiserer, A. Neuzner, M. Uphoff, M. Mücke, E. Figueroa, J. Bochmann & G. Rempe. *An elementary quantum network of single atoms in optical cavities. Nature* **484**, 195–200 (2012).

[62] M. Pompili *et al. Realization of a multinode quantum network of remote solid-state qubits. Science* **372**, 259–264 (2021).

[63] D. Hucul, I. V. Inlek, G. Vittorini, C. Crocker, S. Debnath, S. M. Clark & C. Monroe. *Modular entanglement of atomic qubits using photons and phonons. Nat. Phys.* **11**, 37–42 (2015).

[64] A. Delteil, Z. Sun, W.-b. Gao, E. Togan, S. Faelt & A. Imamoglu. *Generation of heralded entanglement between distant hole spins. Nat. Phys.* **12**, 218–223 (2016).

[65] C. W. Chou, H. de Riedmatten, D. Felinto, S. V. Polyakov, S. J. van Enk & H. J. Kimble. *Measurement-induced entanglement for excitation stored in remote atomic ensembles. Nature* **438**, 828–832 (2005).

[66] N. Maring, P. Farrera, K. Kutluer, M. Mazzera, G. Heinze & H. de Riedmatten. *Photonic quantum state transfer between a cold atomic gas and a crystal. Nature* **551**,

485–488 (2017).

[67] S. Wehner, D. Elkouss & R. Hanson. *Quantum internet: A vision for the road ahead. Science* **362** (2018).

[68] D. Meschede, H. Walther & G. Müller. *One-Atom Maser. Phys. Rev. Lett.* **54**, 551–554 (1985).

[69] G. Rempe, H. Walther & N. Klein. *Observation of quantum collapse and revival in a one-atom maser. Phys. Rev. Lett.* **58**, 353–356 (1987).

[70] G. Rempe, R. J. Thompson, H. J. Kimble & R. Lalezari. *Measurement of ultralow losses in an optical interferometer. Opt. Lett.* **17**, 363–365 (1992).

[71] A. Reiserer & G. Rempe. *Cavity-based quantum networks with single atoms and optical photons. Rev. Mod. Phys.* **87**, 1379–1418 (2015).

[72] S. Daiss, S. Welte, B. Hacker, L. Li & G. Rempe. *Single-Photon Distillation via a Photonic Parity Measurement Using Cavity QED. Phys. Rev. Lett.* **122**, 133603 (2019).

[73] R. P. Feynman. *Simulating physics with computers. Int J Theor Phys* **21**, 467–488 (1982).

[74] D. Jaksch, C. Bruder, J. I. Cirac, C. W. Gardiner & P. Zoller. *Cold Bosonic Atoms in Optical Lattices. Phys. Rev. Lett.* **81**, 3108–3111 (1998).

[75] B. Schumacher. *Quantum coding. Phys. Rev. A* **51**, 2738–2747 (1995).

[76] D. Deutsch. *Quantum theory, the Church-Turing principle and the universal quantum computer. Proc. R. Soc. Lond. A* **400**, 97–117 (1985).

[77] A. Chi-Chih Yao. Quantum Circuit Complexity. In *Proceedings of the 1993 IEEE 34th Annual Foundations of Computer Science*, SFCS '93, 352–361 (1993).

[78] P. W. Shor. Algorithms for quantum computation: discrete logarithms and factoring. In *Proceedings 35th Annual Symposium on Foundations of Computer Science*, 124–134 (1994).

[79] L. K. Grover. A Fast Quantum Mechanical Algorithm for Database Search. In *Proceedings of the Twenty-Eighth Annual ACM Symposium on Theory of Computing*, STOC '96, 212–219 (1996).

[80] C. Hempel *et al. Quantum Chemistry Calculations on a Trapped-Ion Quantum Simulator. Phys. Rev. X* **8**, 031022 (2018).

[81] H. Levine *et al. Parallel Implementation of High-Fidelity Multiqubit Gates with Neutral Atoms. Phys. Rev. Lett.* **123**, 170503 (2019).

[82] L. M. K. Vandersypen, M. Steffen, G. Breyta, C. S. Yannoni, M. H. Sherwood & I. L. Chuang. *Experimental realization of Shor's quantum factoring algorithm using nuclear magnetic resonance. Nature* **414**, 883–887 (2001).

[83] S. Rosenblum, P. Reinhold, M. Mirrahimi, L. Jiang, L. Frunzio & R. J. Schoelkopf.

Fault-tolerant detection of a quantum error. Science **361**, 266–270 (2018).

[84] P. Kok, W. J. Munro, K. Nemoto, T. C. Ralph, J. P. Dowling & G. J. Milburn. *Linear optical quantum computing with photonic qubits. Rev. Mod. Phys.* **79**, 135–174 (2007).

[85] F. Arute *et al. Quantum supremacy using a programmable superconducting processor. Nature* **574**, 505–510 (2019).

[86] L. M. Sager, S. E. Smart & D. A. Mazziotti. *Preparation of an exciton condensate of photons on a 53-qubit quantum computer. Phys. Rev. Research* **2**, 043205 (2020).

[87] D. P. DiVincenzo. *The Physical Implementation of Quantum Computation. Fortschr. Phys.* **48**, 771–783 (2000).

[88] T. D. Ladd, F. Jelezko, R. Laflamme, Y. Nakamura, C. Monroe & J. L. O'Brien. *Quantum computers. Nature* **464**, 45–53 (2010).

[89] R. Van Meter & S. J. Devitt. *The Path to Scalable Distributed Quantum Computing. Computer* **49**, 31–42 (2016).

[90] S. J. Devitt, W. J. Munro & K. Nemoto. *Quantum error correction for beginners. Rep. Prog. Phys.* **76**, 076001 (2013).

[91] C. R. Monroe, R. Raussendorf, A. Ruthven, K. R. Brown, P. Maunz, L.-M. Duan & J. Kim. *Large-scale modular quantum-computer architecture with atomic memory and photonic interconnects. Phys. Rev. A* **89**, 022317 (2014).

[92] C. R. Monroe, R. J. Schoelkopf & M. D. Lukin. *Quantum Connections. Scientific American* **314**, 50–57 (2016).

[93] D. Gottesman & I. L. Chuang. *Demonstrating the viability of universal quantum computation using teleportation and single-qubit operations. Nature* **402**, 390–393 (1999).

[94] S. Daiss, S. Langenfeld, S. Welte, E. Distante, P. Thomas, L. Hartung, O. Morin & G. Rempe. *A quantum-logic gate between distant quantum-network modules. Science* **371**, 614–617 (2021).

[95] H. J. Metcalf & P. van der Straten. *Laser Cooling and Trapping* (Springer-Verlag, 1999).

[96] E. T. Jaynes & F. W. Cummings. *Comparison of quantum and semiclassical radiation theories with application to the beam maser. Proceedings of the IEEE* **51**, 89–109 (1963).

[97] A. Kuhn. Cavity Induced Interfacing of Atoms and Light. In A. Predojević & M. W. Mitchell (eds.) *Engineering the Atom-Photon Interaction*, 3–38 (Springer, 2015).

[98] R. Gehr, J. Volz, G. Dubois, T. Steinmetz, Y. Colombe, B. L. Lev, R. Long, J. Estève & J. Reichel. *Cavity-Based Single Atom Preparation and High-Fidelity Hyperfine State Readout. Phys. Rev. Lett.* **104**, 203602 (2010).

[99] M. Uphoff, M. Brekenfeld, G. Rempe & S. Ritter. *Frequency splitting of polarization*

eigenmodes in microscopic Fabry–Perot cavities. New J. Phys. **17**, 013053 (2015).

[100] H. Takahashi, E. Kassa, C. Christoforou & M. Keller. *Strong Coupling of a Single Ion to an Optical Cavity. Phys. Rev. Lett.* **124**, 013602 (2020).

[101] R. J. Thompson, G. Rempe & H. J. Kimble. *Observation of normal-mode splitting for an atom in an optical cavity. Phys. Rev. Lett.* **68**, 1132–1135 (1992).

[102] D. F. Walls & G. J. Milburn. *Quantum Optics* (Springer-Verlag, 2008).

[103] M. J. Collett & C. W. Gardiner. *Squeezing of intracavity and traveling-wave light fields produced in parametric amplification. Phys. Rev. A* **30**, 1386–1391 (1984).

[104] C. W. Gardiner & M. J. Collett. *Input and output in damped quantum systems: Quantum stochastic differential equations and the master equation. Phys. Rev. A* **31**, 3761–3774 (1985).

[105] M. Malekakhlagh. *Heisenberg-Langevin Formalism For Open Circuit-QED Systems. Dissertation. Princeton University* (2017).

[106] C. Y. Hu, A. Young, J. L. O'Brien, W. J. Munro & J. G. Rarity. *Giant optical Faraday rotation induced by a single-electron spin in a quantum dot: Applications to entangling remote spins via a single photon. Phys. Rev. B* **78**, 085307 (2008).

[107] I. Cohen & K. Mølmer. *Deterministic quantum network for distributed entanglement and quantum computation. Phys. Rev. A* **98**, 030302 (2018).

[108] A. Neuzner. *Resonance Fluorescence of an Atom Pair in an Optical Resonator. Dissertation. Technische Universität München* (2015).

[109] M. A. Nielsen & I. L. Chuang. *Quantum Computation and Quantum Information* (Cambridge University Press, 2016).

[110] R. Raussendorf, D. E. Browne & H. J. Briegel. *Measurement-based quantum computation on cluster states. Phys. Rev. A* **68**, 022312 (2003).

[111] S. Welte, B. Hacker, S. Daiss, S. Ritter & G. Rempe. *Photon-Mediated Quantum Gate between Two Neutral Atoms in an Optical Cavity. Phys. Rev. X* **8**, 011018 (2018).

[112] A. Reiserer, S. Ritter & G. Rempe. *Nondestructive Detection of an Optical Photon. Science* **342**, 1349–1351 (2013).

[113] A. Reiserer, N. Kalb, G. Rempe & S. Ritter. *A quantum gate between a flying optical photon and a single trapped atom. Nature* **508**, 237–240 (2014).

[114] M. Uphoff. *Optical microcavities for quantum communication with single atoms. Dissertation. Technische Universität München* (2017).

[115] M. Körber. *Long-lived and Efficient Qubit Memory for Photonic Quantum Networks. Dissertation. Technische Universität München* (2020).

[116] S. Langenfeld. *Quantum Communication with a Two-Atoms Network Node. Dissertation. Technische Universität München* (2021).

[117] S. Nußmann. *Kühlen und Positionieren eines Atoms in einem optischen Resonator. Dissertation. Technische Universität München* (2006).

[118] H. Specht. *Einzelatom-Quantenspeicher für Polarisations-Qubits. Dissertation. Technische Universität München* (2010).

[119] B. Weber. *Distribution of quantum information between an atom and two photons. Dissertation. Technische Universität München* (2008).

[120] M. Uphoff. *State manipulation of single atoms in an optical cavity. Diploma thesis, Technische Universität München* (2010).

[121] C. Nölleke. *Quantum state transfer between remote single atoms. Dissertation. Technische Universität München* (2013).

[122] C. Hahn. *Remote Entanglement of Two Single Atoms. Dissertation. Technische Universität München* (2014).

[123] A. A. Reiserer. *A controlled phase gate between a single atom and an optical photon. Dissertation. Technische Universität München* (2014).

[124] N. Kalb. *Heralded storage of photonic polarization in a single atom. Master thesis, Technische Universität München* (2014).

[125] B. Hacker. *Two-Photon Gate and Creation of Optical Cat States using One Atom in a Cavity. Dissertation. Technische Universität München* (2019).

[126] S. T. Welte. *Photon-Mediated Quantum Information Processing with Neutral Atoms in an Optical Cavity. Dissertation. Technische Universität München* (2019).

[127] D. A. Steck. *Rubidium 87 D Line Data. available online at `http://steck.us/alkalidata`* (Version 2.2.1, last revised 21 November 2019).

[128] R. Grimm, M. Weidemüller & Y. B. Ovchinnikov. *Optical Dipole Traps for Neutral Atoms. Advances In Atomic, Molecular, and Optical Physics* **42**, 95 – 170 (2000).

[129] E. D. Black. *An introduction to Pound-Drever-Hall laser frequency stabilization. Am. J. Phys* **69**, 79 (2001).

[130] J. Bochmann, M. Mücke, C. Guhl, S. Ritter, G. Rempe & D. L. Moehring. *Lossless State Detection of Single Neutral Atoms. Phys. Rev. Lett.* **104**, 203601 (2010).

[131] V. Scarani, H. Bechmann-Pasquinucci, N. J. Cerf, M. Dušek, N. Lütkenhaus & M. Peev. *The security of practical quantum key distribution. Rev. Mod. Phys.* **81**, 1301–1350 (2009).

[132] E. Knill, R. Laflamme & G. J. Milburn. *A scheme for efficient quantum computation with linear optics. Nature* **409**, 46–52 (2001).

[133] J. L. O'Brien. *Optical Quantum Computing. Science* **318**, 1567–1570 (2007).

[134] B. Hacker, S. Welte, G. Rempe & S. Ritter. *A photon-photon quantum gate based on a single atom in an optical resonator. Nature* **536**, 193–196 (2016).

[135] D. Tiarks, S. Schmidt-Eberle, T. Stolz, G. Rempe & S. Dürr. *A photon-photon*

quantum gate based on Rydberg interactions. Nat. Phys. **15**, 124–126 (2019).

[136] S. Aaronson & A. Arkhipov. *The Computational Complexity of Linear Optics. Theory of Computing* **9**, 143–252 (2013).

[137] J. B. Spring *et al. Boson Sampling on a Photonic Chip. Science* **339**, 798–801 (2013).

[138] C. Brunel, B. Lounis, P. Tamarat & M. Orrit. *Triggered Source of Single Photons based on Controlled Single Molecule Fluorescence. Phys. Rev. Lett.* **83**, 2722–2725 (1999).

[139] B. Lounis & W. E. Moerner. *Single photons on demand from a single molecule at room temperature. Nature* **407**, 491–493 (2000).

[140] M. Keller, B. Lange, K. Hayasaka, W. Lange & H. Walther. *Continuous generation of single photons with controlled waveform in an ion-trap cavity system. Nature* **431**, 1075–1078 (2004).

[141] A. Kuhn, M. Hennrich & G. Rempe. *Deterministic Single-Photon Source for Distributed Quantum Networking. Phys. Rev. Lett.* **89**, 067901 (2002).

[142] J. McKeever, A. Boca, A. D. Boozer, R. Miller, J. R. Buck, A. Kuzmich & H. J. Kimble. *Deterministic Generation of Single Photons from One Atom Trapped in a Cavity. Science* **303**, 1992–1994 (2004).

[143] C. Kurtsiefer, S. Mayer, P. Zarda & H. Weinfurter. *Stable Solid-State Source of Single Photons. Phys. Rev. Lett.* **85**, 290–293 (2000).

[144] R. Brouri, A. Beveratos, J.-P. Poizat & P. Grangier. *Photon antibunching in the fluorescence of individual color centers in diamond. Opt. Lett.* **25**, 1294–1296 (2000).

[145] P. Lodahl, S. Mahmoodian & S. Stobbe. *Interfacing single photons and single quantum dots with photonic nanostructures. Rev. Mod. Phys.* **87**, 347–400 (2015).

[146] C. K. Hong & L. Mandel. *Experimental realization of a localized one-photon state. Phys. Rev. Lett.* **56**, 58–60 (1986).

[147] C. W. Chou, S. V. Polyakov, A. Kuzmich & H. J. Kimble. *Single-Photon Generation from Stored Excitation in an Atomic Ensemble. Phys. Rev. Lett.* **92**, 213601 (2004).

[148] X.-H. Bao, A. Reingruber, P. Dietrich, J. Rui, A. Dück, T. Strassel, L. Li, N.-L. Liu, B. Zhao & J.-W. Pan. *Efficient and long-lived quantum memory with cold atoms inside a ring cavity. Nat. Phys.* **8**, 517–521 (2012).

[149] E. Bimbard, R. Boddeda, N. Vitrant, A. Grankin, V. Parigi, J. Stanojevic, A. Ourjoumtsev & P. Grangier. *Homodyne Tomography of a Single Photon Retrieved on Demand from a Cavity-Enhanced Cold Atom Memory. Phys. Rev. Lett.* **112**, 033601 (2014).

[150] Y. O. Dudin & A. Kuzmich. *Strongly Interacting Rydberg Excitations of a Cold Atomic Gas. Science* **336**, 887–889 (2012).

[151] T. Peyronel, O. Firstenberg, Q.-Y. Liang, S. Hofferberth, A. V. Gorshkov, T. Pohl, M. D. Lukin & V. Vuletić. *Quantum nonlinear optics with single photons enabled by*

strongly interacting atoms. Nature **488**, 57–60 (2012).

[152] B. Wang & L.-M. Duan. *Engineering superpositions of coherent states in coherent optical pulses through cavity-assisted interaction. Phys. Rev. A* **72**, 022320 (2005).

[153] B. Hacker, S. Welte, S. Daiss, A. Shaukat, S. Ritter, L. Li & G. Rempe. *Deterministic creation of entangled atom-light Schrödinger-cat states. Nat. Photon.* **13**, 110–115 (2019).

[154] R. J. Glauber. *The Quantum Theory of Optical Coherence. Phys. Rev.* **130**, 2529–2539 (1963).

[155] N. Spagnolo, C. Vitelli, T. De Angelis, F. Sciarrino & F. De Martini. *Wigner-function theory and decoherence of the quantum-injected optical parametric amplifier. Phys. Rev. A* **80**, 032318 (2009).

[156] G. M. D'Ariano, U. Leonhardt & H. Paul. *Homodyne detection of the density matrix of the radiation field. Phys. Rev. A* **52**, R1801–R1804 (1995).

[157] N. Somaschi *et al. Near-optimal single-photon sources in the solid state. Nat. Photon.* **10**, 340–345 (2016).

[158] U. Leonhardt. *Measuring the Quantum State of Light* (Cambridge University Press, 1997).

[159] D. T. Smithey, M. Beck, M. G. Raymer & A. Faridani. *Measurement of the Wigner distribution and the density matrix of a light mode using optical homodyne tomography: Application to squeezed states and the vacuum. Phys. Rev. Lett.* **70**, 1244–1247 (1993).

[160] A. Furusawa. *Quantum States of Light* (Springer, 2015).

[161] A. I. Lvovsky & M. G. Raymer. *Continuous-variable optical quantum-state tomography. Rev. Mod. Phys.* **81**, 299–332 (2009).

[162] A. I. Lvovsky. *Iterative maximum-likelihood reconstruction in quantum homodyne tomography. J. Opt. B: Quantum Semiclass. Opt.* **6**, S556–S559 (2004).

[163] E. Wigner. *On the Quantum Correction For Thermodynamic Equilibrium. Phys. Rev.* **40**, 749–759 (1932).

[164] R. Kumar, E. Barrios, A. MacRae, E. Cairns, E. Huntington & A. Lvovsky. *Versatile wideband balanced detector for quantum optical homodyne tomography. Optics Communications* **285**, 5259–5267 (2012).

[165] R. Hanbury Brown & R. Q. Twiss. *LXXIV. A new type of interferometer for use in radio astronomy. The London, Edinburgh, and Dublin Philosophical Magazine and Journal of Science* **45**, 663–682 (1954).

[166] R. Hanbury Brown & R. Q. Twiss. *Correlation between Photons in two Coherent Beams of Light. Nature* **177**, 27–29 (1956).

[167] R. Hanbury Brown & R. Q. Twiss. *A Test of a New Type of Stellar Interferometer on Sirius. Nature* **178**, 1046–1048 (1956).

[168] H. J. Kimble, M. Dagenais & L. Mandel. *Photon Antibunching in Resonance Fluorescence. Phys. Rev. Lett.* **39**, 691–695 (1977).

[169] X. Rasmus. Transimpedance Considerations for High-Speed Amplifiers. `https://www.ti.com/lit/pdf/sboa122` (2009). Accessed: 2021-07-29.

[170] A. V. Masalov, A. Kuzhamuratov & A. I. Lvovsky. *Noise spectra in balanced optical detectors based on transimpedance amplifiers. Rev. Sci. Instrum.* **88**, 113109 (2017).

[171] J. R. Johansson, P. D. Nation & F. Nori. *QuTiP: An open-source Python framework for the dynamics of open quantum systems. Comput. Phys. Commun.* **183**, 1760–1772 (2012).

[172] A. V. Gorshkov, A. André, M. D. Lukin & A. S. Sørensen. *Photon storage in Λ-type optically dense atomic media. II. Free-space model. Phys. Rev. A* **76**, 033805 (2007).

[173] M. Mücke, J. Bochmann, C. Hahn, A. Neuzner, C. Nölleke, A. Reiserer, G. Rempe & S. Ritter. *Generation of single photons from an atom-cavity system. Phys. Rev. A* **87**, 063805 (2013).

[174] A. Ourjoumtsev, H. Jeong, R. Tualle-Brouri & P. Grangier. *Generation of optical 'Schrödinger cats' from photon number states. Nature* **448**, 784–786 (2007).

[175] C. Hamsen, K. N. Tolazzi, T. Wilk & G. Rempe. *Strong coupling between photons of two light fields mediated by one atom. Nat. Phys.* **14**, 885–889 (2018).

[176] J. C. Loredo *et al. Generation of non-classical light in a photon-number superposition. Nat. Photon.* **13**, 803–808 (2019).

[177] N. Ofek *et al. Extending the lifetime of a quantum bit with error correction in superconducting circuits. Nature* **536**, 441–445 (2016).

[178] K. Wright *et al. Benchmarking an 11-qubit quantum computer. Nat. Commun.* **10**, 5464 (2019).

[179] C. Kokail *et al. Self-verifying variational quantum simulation of lattice models. Nature* **569**, 355–360 (2019).

[180] D. L. Moehring, P. Maunz, S. Olmschenk, K. C. Younge, D. N. Matsukevich, L.-M. Duan & C. Monroe. *Entanglement of single-atom quantum bits at a distance. Nature* **449**, 68–71 (2007).

[181] J. Hofmann, M. Krug, N. Ortegel, L. Gérard, M. Weber, W. Rosenfeld & H. Weinfurter. *Heralded Entanglement Between Widely Separated Atoms. Science* **337**, 72–75 (2012).

[182] H. Bernien *et al. Heralded entanglement between solid-state qubits separated by three metres. Nature* **497**, 86–90 (2013).

[183] N. Kalb, A. A. Reiserer, P. C. Humphreys, J. J. W. Bakermans, S. J. Kamerling, N. H. Nickerson, S. C. Benjamin, D. J. Twitchen, M. Markham & R. Hanson. *Entanglement distillation between solid-state quantum network nodes. Science* **356**, 928–932 (2017).

[184] Y. Yu *et al. Entanglement of two quantum memories via fibres over dozens of*

kilometres. Nature **578**, 240–245 (2020).

[185] L. J. Stephenson, D. P. Nadlinger, B. C. Nichol, S. An, P. Drmota, T. G. Ballance, K. Thirumalai, J. F. Goodwin, D. M. Lucas & C. J. Ballance. *High-Rate, High-Fidelity Entanglement of Qubits Across an Elementary Quantum Network. Phys. Rev. Lett.* **124**, 110501 (2020).

[186] D. Lago-Rivera, S. Grandi, J. V. Rakonjac, A. Seri & H. de Riedmatten. *Telecom-heralded entanglement between multimode solid-state quantum memories. Nature* **594**, 37–40 (2021).

[187] J. Eisert, K. Jacobs, P. Papadopoulos & M. B. Plenio. *Optimal local implementation of nonlocal quantum gates. Phys. Rev. A* **62**, 052317 (2000).

[188] Y.-F. Huang, X.-F. Ren, Y.-S. Zhang, L.-M. Duan & G.-C. Guo. *Experimental Teleportation of a Quantum Controlled-NOT Gate. Phys. Rev. Lett.* **93**, 240501 (2004).

[189] W.-B. Gao *et al. Teleportation-based realization of an optical quantum two-qubit entangling gate. Proc. Natl. Acad. Sci.* **107**, 20869–20874 (2010).

[190] S. Yokoyama, R. Ukai, J.-i. Yoshikawa, P. Marek, R. Filip & A. Furusawa. *Nonlocal quantum gate on quantum continuous variables with minimal resources. Phys. Rev. A* **90**, 012311 (2014).

[191] P. K. Vishnu, D. Joy, B. K. Behera & P. K. Panigrahi. *Experimental demonstration of non-local controlled-unitary quantum gates using a five-qubit quantum computer. Quantum Inf Process* **17**, 274 (2018).

[192] K. S. Chou, J. Z. Blumoff, C. S. Wang, P. C. Reinhold, C. J. Axline, Y. Y. Gao, L. Frunzio, M. H. Devoret, L. Jiang & R. J. Schoelkopf. *Deterministic teleportation of a quantum gate between two logical qubits. Nature* **561**, 368–373 (2018).

[193] Y. Wan *et al. Quantum gate teleportation between separated qubits in a trapped-ion processor. Science* **364**, 875–878 (2019).

[194] L.-M. Duan, B. Wang & H. J. Kimble. *Robust quantum gates on neutral atoms with cavity-assisted photon scattering. Phys. Rev. A* **72**, 032333 (2005).

[195] X.-M. Lin, Z.-W. Zhou, M.-Y. Ye, Y.-F. Xiao & G.-C. Guo. *One-step implementation of a multiqubit controlled-phase-flip gate. Phys. Rev. A* **73**, 012323 (2006).

[196] T. Yamamoto, Y. A. Pashkin, O. Astafiev, Y. Nakamura & J. S. Tsai. *Demonstration of conditional gate operation using superconducting charge qubits. Nature* **425**, 941–944 (2003).

[197] F. Schmidt-Kaler, H. Häffner, M. Riebe, S. Gulde, G. P. T. Lancaster, T. Deuschle, C. Becher, C. F. Roos, J. Eschner & R. Blatt. *Realization of the Cirac–Zoller controlled-NOT quantum gate. Nature* **422**, 408–411 (2003).

[198] J. B. Altepeter, D. F. V. James & P. G. Kwiat. 4 Qubit Quantum State Tomography. In M. Paris & J. Řeháček (eds.) *Quantum State Estimation. Lecture Notes in Physics, vol 649* (Springer, 2004).

[199] T. Nadolny. *Automatic Compensation of Polarization Drifts in an Optical Fiber.* Bachelor thesis, Ludwig-Maximilians-Universität München (2018).

[200] F. Hocke. *Long Distance Atom Photon Entanglement.* Diploma thesis, Ludwig-Maximilians-Universität München (2007).

[201] W. Rosenfeld, F. Hocke, F. Henkel, M. Krug, J. Volz, M. Weber & H. Weinfurter. *Towards Long-Distance Atom-Photon Entanglement. Phys. Rev. Lett.* **101**, 260403 (2008).

[202] M. Körber, O. Morin, S. Langenfeld, A. Neuzner, S. Ritter & G. Rempe. *Decoherence-protected memory for a single-photon qubit. Nat. Photon.* **12**, 18–21 (2018).

[203] H. Labuhn, D. Barredo, S. Ravets, S. de Léséleuc, T. Macrì, T. Lahaye & A. Browaeys. *Tunable two-dimensional arrays of single Rydberg atoms for realizing quantum Ising models. Nature* **534**, 667–670 (2016).

[204] M. Endres, H. Bernien, A. Keesling, H. Levine, E. R. Anschuetz, A. Krajenbrink, C. Senko, V. Vuletic, M. Greiner & M. D. Lukin. *Atom-by-atom assembly of defect-free one-dimensional cold atom arrays. Science* **354**, 1024–1027 (2016).

[205] A. Neuzner, M. Körber, O. Morin, S. Ritter & G. Rempe. *Interference and dynamics of light from a distance-controlled atom pair in an optical cavity. Nat. Photon.* **10**, 303–306 (2016).

[206] E. R. Elliott, M. C. Krutzik, J. R. Williams, R. J. Thompson & D. C. Aveline. *NASA's Cold Atom Lab (CAL): system development and ground test status. npj Microgravity* **4**, 16 (2018).

[207] S. Sun, H. Kim, G. S. Solomon & E. Waks. *A quantum phase switch between a single solid-state spin and a photon. Nat. Nanotechnol.* **11**, 539–544 (2016).

[208] J.-C. Besse, S. Gasparinetti, M. C. Collodo, T. Walter, P. Kurpiers, M. Pechal, C. Eichler & A. Wallraff. *Single-Shot Quantum Nondemolition Detection of Individual Itinerant Microwave Photons. Phys. Rev. X* **8**, 021003 (2018).

Acknowledgements